# *Tracking past sea-level changes via isotope geochemistry: Insights from a Holocene post-Last Glacial Maximum record, NW Scotland*

JENNIFER LOUISE TAYLOR

# Tracking past sea-level changes via isotope geochemistry: Insights from a Holocene post-Last Glacial Maximum record, NW Scotland

Jennifer Taylor

Thesis submitted for the degree of

Master of Science (by Research)

Department of Earth Sciences

Durham University

2021

# Abstract

Previous paleoenvironmental and sea-level reconstructions from nearshore environments have typically required the preservation of biological proxies, however, in regions of poor preservation such reconstructions are severely hampered. Thus, this research utilises an isotopic tracer (osmium-isotope system - $^{187}Os/^{188}Os$) that is not reliant on microfossil preservation but is captured by sedimentary organic matter during deposition. Here we apply a multi-element geochemical approach coupling osmium with carbon, sulphur and nitrogen elemental and isotopic analysis together with X-ray fluorescence, radiocarbon dating and foraminiferal analysis to Loch Duart Marsh, NW Scotland, an isolation basin containing Late Glacial to Holocene sediments. This study assesses the suitability of these geochemical proxies for palaeoenvironmental reconstructions and combines them with the established biostratigraphic method of foraminifera analysis to reconstruct a detailed palaeoenvironmental and sea-level reconstruction of Loch Duart Marsh.

The Loch Duart Marsh sediment core contains a sedimentary interval deposited under freshwater conditions, the $^{187}Os/^{188}Os$ signature of which is distinctly more radiogenic (up to 4.3) than during marine deposition (~1). This revealed that periods of inundation and basin isolation can be distinguished in the osmium isotope record. The freshwater interval is further supported by a distinct increase in C/N (~6 units). Radiocarbon dating indicates a duration of freshwater sedimentation of 4.1 ka, with marine ingression following the freshwater phase occurring at 10.2 ka. The complex relative sea-level record of NW Scotland due to glacial isostatic adjustment provides a unique history that is reflected in the $^{187}Os/^{188}Os$ signature of the sedimentary organic matter, where $^{187}Os/^{188}Os$ values of ~1 reflect marine settings and more radiogenic values indicate freshwater deposition. The application of $^{187}Os/^{188}Os$ geochemistry to this site further displays its suitability as a technique to reconstruct relative sea-level, a technique that could be applied to basins globally.

**Contents**

# List of Tables

## Chapter 7: Results

## List of Figures

**Figure 17:** RSL curves from Kuchar et al. (2012) (dashed black line) and Bradley et al. (2011) (solid black line) model predictions for Assynt, sea-level index points from Coigach (Shennan et al., 2000) are denoted in black, and those from Duart in red. An index point based on radiocarbon material is represented by the red diamond and the black solid square denotes a limiting index point. The arrows indicate the positive or negative tendency associated with each sea-level index point. Underneath the graph, the stratigraphic units of Loch Duart Marsh are presented with the dates of the transitions between units annotated the dates are estimated from the age-depth model for this study (Fig. 16). RSL figure from Hamilton et al. (2015)..72

## Declaration of Copyright



## Acknowledgements

I would like to give a special thank you to my supervisors at Durham University David Selby and Jeremy Lloyd for creating this project title and for their excellent guidance, patience and support throughout this project. Many thanks also to Durham University for providing financial assistance for accommodation during the fieldwork required for this project. I would also like to thank my family for their continued support and of relevance to this study their help during the fieldwork aspect of this project.

# 1. Introduction

The impacts of future sea-level rise on coastal regions in response to ongoing climate change are of increasing concern. It is projected that by 2100 global sea level could rise by ~2 m under continued emissions scenarios, the effects of early-onset Antarctic ice sheet instability could lead this value to be surpassed (Bamber et al., 2019; Kopp et al., 2017; Wong et al., 2017). The effects of this sea-level rise are multifaceted and hugely prevalent to human civilisation not least because some of the most densely populated regions on Earth are coastal zones due to access to trade routes and resources (Neumann et al., 2015). Recent work has increased estimates of the effect of sea level on human life threefold suggesting that by 2100 with a +2°C warming scenario 310-420 million people will be threatened by annual flood events (Kulp & Strauss, 2019). If Antarctic instability is accounted for this estimate increases to 380-630 million (Kulp & Strauss, 2019). One method to more accurately predict future changes in sea level is to improve our comprehension of past sea-level changes. Past sea-level reconstructions provide critical input data that can be used to test and refine models of future change. Understanding past environmental changes in marginal marine environments is also vital in understanding the potential implications of future climate change on coastal environments as these are particularly sensitive to climate perturbations influencing sea level and ocean circulation.

The British and Irish Ice Sheet (BIIS) was present over much of the British Isles during the Last Glacial Maximum (LGM). It has long been recognised that the onset and demise of this ice sheet resulted in complex relative sea-level (RSL) histories across the British Isles due to the glacial and periglacial isostatic readjustment following the ice sheets deglaciation (e.g., Flemming, 1982). Additionally, the ocean geoid is believed to have changed shape sufficiently during the Quaternary to produce apparent changes in sea level on a regional basis (Mörner, 1976, 1980). As a result of the deglaciation of the BIIS, geological in addition to tide gauge

data show differential movement between Scotland which experienced relative uplift and the south of England which saw relative subsidence (e.g., Sissons, 1983; Shennan et al., 1983; Shennan et al., 2018). The RSL record in Scotland is well documented through a range of geological evidence including sedimentological and biological archives and these records have been used to refine models of RSL change (Shennan et al., 2006). However, sites of poor preservation of typical climate and RSL proxies such as microfossils in some areas has limited the ability to reconstruct paleoclimatic conditions therefore the development of an alternate method of reconstruction would expand the paleoclimatic understanding of the region spatially allowing for a more complete understanding of the impacts of RSL and climatic conditions on the British Isles.

Herein the aims of this study are twofold. Firstly, the suitability of a range of geochemical proxies (XRF, TOC, $\delta^{13}C$, C/S and $^{187}Os/^{188}Os$) for palaeoenvironmental and sea-level reconstruction from an isolation basin setting will be assessed. The ability of these geochemical proxies to track connection to and isolation from the open sea dependent on relative sea level could allow their application to regions lacking biostratigraphy. Secondly, the study will apply these multi-geochemical proxies in combination with the established biostratigraphic proxy of foraminifera analysis to reconstruct a detailed palaeoenvironmental and sea-level reconstruction of Loch Duart Marsh an isolation basin in NW Scotland.

# 4. Context of Research

This chapter outlines the existing literature regarding the glacial and deglacial history of NW Scotland and the effects of this on RSL. The RSL history of NW Scotland is discussed with a focus on its behaviour following the deglaciation of the BIIS. Finally, isolation basins and their affinity for RSL reconstructive research are discussed.

## 4.1 British and Irish Ice Sheet

The British and Irish Ice Sheet (BIIS) is believed to have covered most of Britain, Ireland and the North Sea during the last glacial, reaching its furthest extent 27 ka BP (Clark et al., 2012). For over 150 years the BIIS and its extent has been studied extensively with some of the earliest research employing sedimentological evidence to identify that land ice rather than icebergs had in fact been present and were the cause of glacial drift deposits (e.g. Geikie, 1894). Over the last century research into the BIIS has been an interdisciplinary effort combining the fields of sedimentology and geomorphology with modern seismic and Geographic Information System (GIS) software (e.g. Nygård et al., 2004; Clark et al., 2012). Whilst the presence of an ice sheet over much of the British Isles is widely accepted, its extent is still debated. The furthest extent of the BIIS has recently been increased from a primarily terrestrial ice sheet (ca. 357,000 $km^2$) to a much larger (ca. 840,000 $km^2$) predominantly marine-based ice sheet covering extensive areas of the North Sea and continental shelves of Britain and Ireland (Fig. 1) (Clark et al., 2012).

Earlier research investigating the extent of the BIIS primarily based on onshore biostratigraphy and lithological evidence estimated the BIIS to be independent with a limited extent (Davies et al., 1984; Bowen, 1986). The ice sheet was estimated to extend only a brief distance onto the Atlantic shelf and the North Sea basin, (extent shown by the red line on figure 1, Bowen,

1986). This interpretation strongly influenced ice sheet models later proposed (e.g., Boulton et al., 1991; Lambeck, 1995).

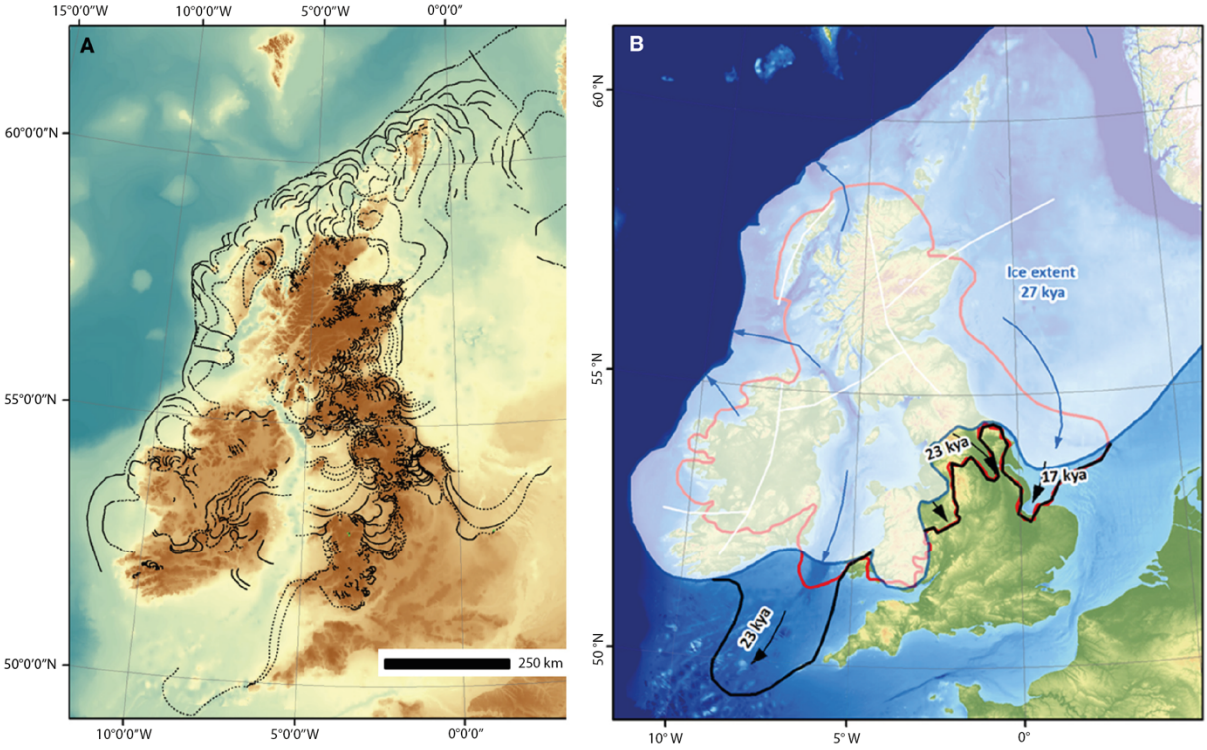


**Figure 1:** A – A reconstruction of the pattern of retreat of the BIIS inferred from mapped geomorphic features. B – Overview of the maximum extent of the BIIS, the solid red line depicts the earlier idea of a largely terrestrial ice sheet (Bowen et al., 1986). The white shaded area depicts the extent of the ice at 27 ka based on more recent study the black solid lines show succeeding advances of the BIIS (Clark et al., 2012; Clark et al., 2018). Figure from Clark et al., (2018).

More contemporary reconstructions of the ice sheet have been facilitated by the advancement of modern reconstructive techniques including digital elevation models, offshore geophysical data and cosmogenic nuclide surface exposure dating (Sejrup et al., 2005; Greenwood & Clark, 2009; Ballantyne et al., 2010). The northern extent of the BIIS has been revised in more recent reconstructions due to such methods. For example, submarine evidence off the Irish west coast was found to be similar to that seen on the Norwegian shelf allowing the margin to be reconstructed to join SW Ireland with the Fennoscandian Ice Sheet (FIS) (Haflidason et al., 1997; Sejrup et al., 2005). Studies on the ice sheet's southern extent have also led to its revision.

Key glacial and marine deposits in southern Ireland were examined and Optically Stimulated Luminescence (OSL) dates were used to demonstrate that southern Ireland was covered by ice during the last glaciation (Ó Cofaigh et al., 2012). Subsequently, recent reconstructions have revised the extent of the BIIS showing it to be largely marine-based (Figure 1B) with an estimated 300,000 $km^3$ of ice on the continental shelves of Britain and Ireland and over the North Sea (Clark et al., 2012). The exact cause of the retreat of the BIIS is a continued topic of study. Increasing levels of northern hemisphere solar insolation has been postulated as the trigger for the deglaciation of the BIIS as rising temperatures in addition to a rising sea level driven by melting of other ice masses could cause ice sheet instability (e.g., Clark et al., 2009). More recent studies suggest an alternate trigger for deglaciation. Evidence from radiocarbon dating suggests initial ice sheet retreat occurred between 26.3 and 24.8 ka cal BP which is earlier in the global last glacial maximum than previously thought thereby suggesting that the key influence in ice sheet retreat was not atmospheric warming, foraminiferal and glacimarine sediment analysis also support high RSL during deglaciation and the absence of ocean warming (Ó Cofaigh et al., 2019). As a result, glacial isostatic depression of the crust has been interpreted to be the cause of the high relative sea level that caused the onset of deglaciation from the shelf margin as the timing of first retreat (26.3 – 24.8 cal ka BP) is contemporaneous with the LGM eustatic sea-level lowstand (Lambeck et al., 2014).

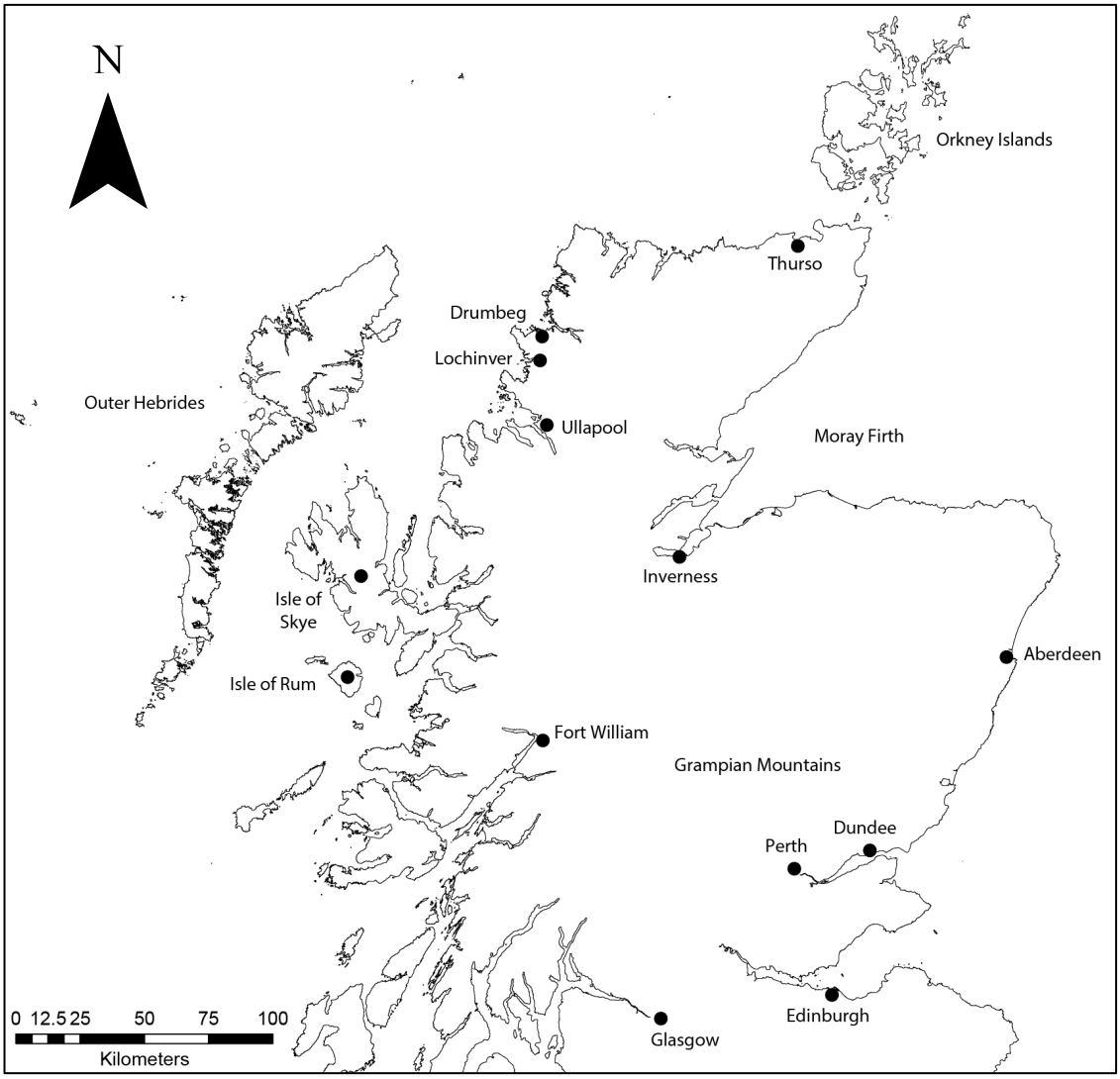


**Figure 2:** Map showing key locations in Scotland discussed throughout the text

Further work on dating glacial features is required to determine whether an external or internal forcing caused the demise of the BIIS. However, whilst the temporal demise of the ice sheet remains uncertain, the spatial pattern of retreat is largely constrained due to the compilation of mapped glacial landforms (e.g., Clark et al., 2012). Following its maximum extent, the BIIS began its retreat along its northern borders whilst it grew in the south in part due to the Irish Sea Ice Stream with glaciers advancing in the Cheshire Basin, Vale of York and England's east coast. The Orkney–Shetland Platform ice cap which at times experienced connection with the FIS to the east, underwent an overall reduction in size at ~23 ka BP and subsequently, the BIIS and FIS separated (Bradwell et al., 2021). Subsequent thinning of the ice sheet occurred with

the ice mostly restricted to the landmasses of Ireland-Scotland with a remaining marine-based portion over the Orkney-Shetland isles. By 17 ka BP the margin of the BIIS is reconstructed to have been mostly onshore, the North Channel and Irish Sea ice streams subsequently severed the ice sheet into almost separate Irish and Scottish ice sheets, which is reconstructed to have taken place by 16 ka BP. (Clark et al., 2012)

The climatic conditions and therefore the extent of glaciation in Scotland during the Late-glacial period (~15 -11 ka BP) is a continued matter of debate (Bradwell et al., 2008). The late-glacial interstadial (14.7-12.9 ka BP) is a particularly contentious period of uncertainty with regard to the presence and extent of glaciation in Scotland with several hypotheses being proposed. Pollen studies and radiocarbon dates suggest extensive to complete deglaciation of Britain at this time (e.g., Sissons, 1967; Bowen et al., 1986). However other authors have argued that restricted glaciers survived and persisted during the Lateglacial Interstadial (e.g., Ballantyne & Sutherland, 1987; Finlayson et al., 2011). Recent analysis using cosmogenic-exposure ages suggests that substantial ice caps were present in north-western Scotland during the Lateglacial Interstadial (Bradwell et al., 2008).

Following this between 12.9 and 11.7 ka BP an abrupt cooling during a period known as the Younger Dryas impacted the northern hemisphere (Bickerdicke et al., 2018a). Cooling was experienced across the British Isles with Scotland experiencing a maximum drop of 10 °C in mean annual temperatures (Golledge et al., 2008). This shift to a phase of cooling led to the regrowth of glaciers in Scotland and parts of northern England (Sissons, 1977; Hubbard, 1999; Golledge, 2010). This period of cooling and glacier regrowth is termed the Loch Lomond Stadial (LLS) in Britain and is analogous to the global Younger Dryas. As discussed, the chronology of retreat of the BIIS has proven complex to reconstruct and this is also true of the retreat of ice during the LLS. One hypothesis for retreat suggests that the glaciers over Scotland

saw continued growth until the termination of the stadial before retreating due to the warming conditions that characterise the transition into the Holocene (11.7-11.6 ka) (Sissons, 1974). A second conflicting hypothesis also suggests that the glaciers retreated rapidly at the transition into the Holocene but argues that they reached their maximum extent by the mid LLS (c. 12.6–12.4 ka) and that retreat soon commenced due to warmer summer temperatures and increased aridity (Benn et al., 1992). The conflict in the ages ascertained from glacial deposits that led to these conflicting hypotheses has been suggested to be due to variations in the size and catchment elevation of glaciers with larger glaciers such as the Lomond responding more slowly to a change in climate whilst those at lower elevations may have become isolated from the catchment areas (Bickerdike et al., 2018b). These findings, in addition to numerical modelling, suggest a maximum extent of LLS glaciation occurring between 12.6 and 12.4 ka BP which supports that glacial retreat commenced during the mid-stadial (Golledge et al., 2008).

Assynt has been a site of study for evidence of the LLS glaciation, cosmogenic $^{10}$Be isotope analysis yielding exposure ages of 12.9-14.1 ka BP supports the existence of glaciers in this region during the LLS (Bradwell, 2006). More recent geomorphological findings show large terminal moraines at Cùl Mòr, Assynt indicating that the glacier in this region maintained its maximum extent for a prolonged period and that its deglaciation was uninterrupted, possibly due to the small size of the glacier or due to a restricted basin size (Bickerdike et al., 2018b).

## 4.2 Relative sea-level change in Scotland

The relative sea-level history across the British Isles has been extensively studied both through direct field observations and more recently numerically through glacial isostatic adjustment (GIA) modelling. Northwest Scotland has been a keen area of interest for over a century with much of the work on Late Glacial and Holocene RSL change in Scotland focused here (Smith et al., 2019). This is illustrated through the longest dated record of RSL spanning the Late Glacial and Holocene being constructed from Arisaig (see Figure 3) (Shennan et al., 1993, 1994, 2006).

Sea level reconstruction has typically relied upon geomorphological indicators of sea-level such as marine terraces and tidal notches. In addition, sedimentary environments such as saltmarshes and isolation basins (see section 4.3) have been used as they provide detailed lithological and biological evidence of transitions between marine and terrestrial conditions (Edwards, 2013). The former of these environments use mean high water spring tides (MHWST) and OD as datums where the carseland is a former saltmarsh (Smith et al., 2003). Isolation basins (discussed further later) use dated lithological and biostratigraphic horizons to constrain RSL (e.g., Shennan et al., 1993). In NW Scotland, isolation basins are the common environment for RSL reconstructions due to the topography of the area with estuarine carselands more abundant in southeast Scotland (Smith et al., 2019).

Complimenting the continuous direct field study of proxies to understand and reconstruct RSL as discussed is the recent advance in GIA modelling. These are modelled on geophysical, rheological, water and ice loading parameters to understand the pattern of uplift experienced within and around Scotland (e.g., Lambeck, 1993; 1995; Bradley et al., 2011). The two most recent BIIS reconstructions from GIA modelling are the Bradley and Kuchar models (Bradley et al., 2011; Kuchar et al., 2012). The former used geomorphological constraints and are based on the maximum vertical height of the ice sheet on trimline data (Ballantyne, 2007). More

recent findings suggest that trimlines in fact mark the upper limit of warm-based ice and therefore represent the minimum vertical height the BIIS reached during the LGM (Ballantyne, 2010). As a result, the second model employs the revised trimline interpretation in conjunction with ice flow directions (Kuchar et al., 2012).

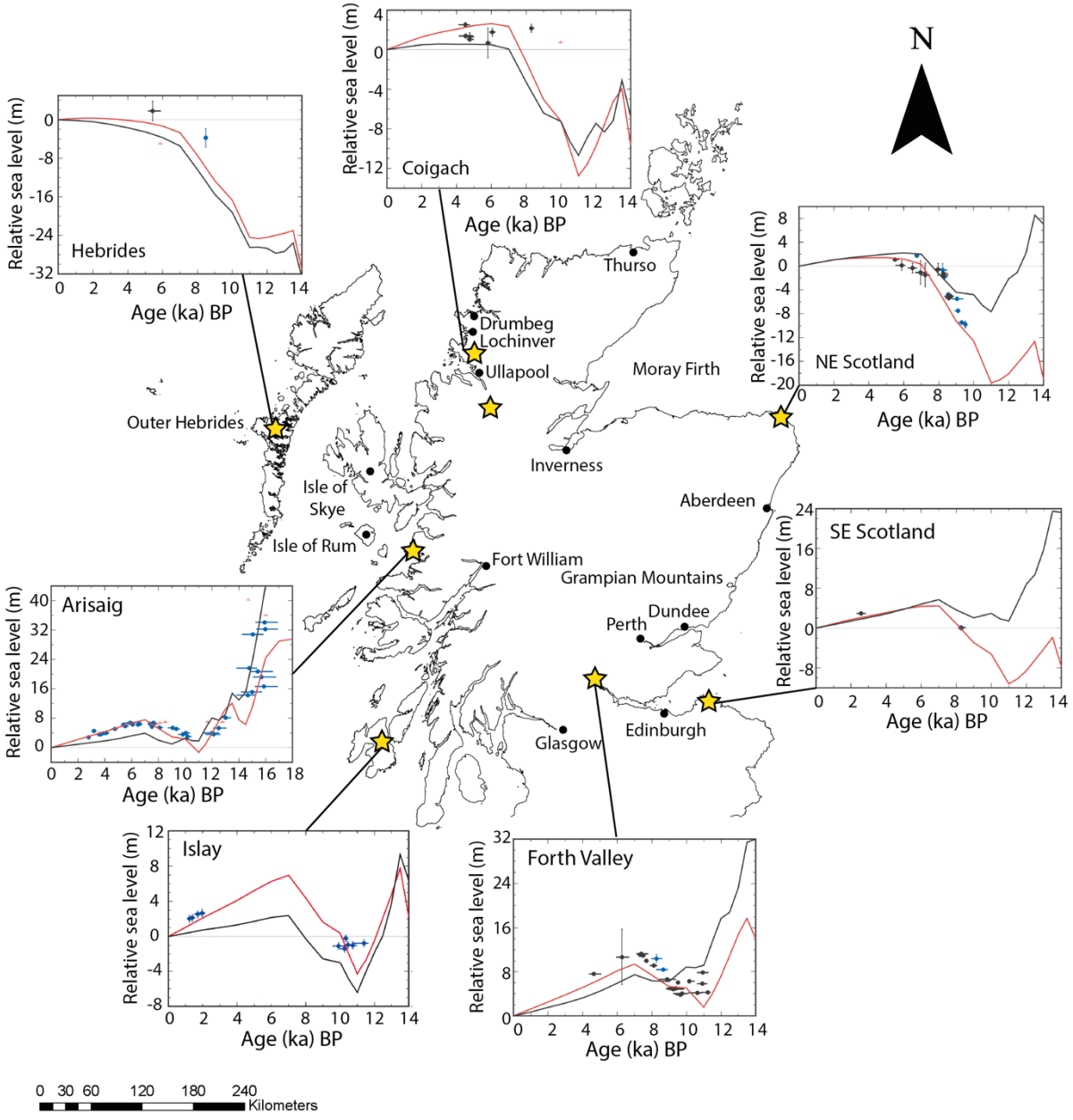


**Figure 3:** Map of Scotland with the location of 7 sites modelled marked by yellow stars the corresponding graphs show the predicted RSL at the sites from the Bradley et al., (2011) (red line) and Kuchar (black line) models, compared to the observed primary sea-level index points (figure adapted from Hamilton et al. (2015), graphs from Smith et al., 2019).

These models are valuable as they allow local and global effects on RSL to be modelled. This is especially useful in Scotland as the RSL signal is governed by both the local isostatic response of the land as a result of the BIIS's deglaciation and to changes in the global sea level due to the deglaciation of larger ice sheets, such as the Laurentide Ice sheet (LIS) or Scandinavian Ice sheet (SIS).

Recent work applied both the Bradley et al., (2011) and Kuchar et al., (2012) models to 7 sites across Scotland to show the effects of local and global influences on RSL (Smith et al., 2019). These sites are all in close proximity to the centre of ice loading and therefore subsequent uplift. As a result, the initial signal is the local effect of the uplift experienced by Scotland due to the deglaciation of the BIIS and is characterised by a fall in RSL. Following this, the more large-scale effect of the deglaciation of larger ice sheets results in the subsequent rise in RSL this is seen in Figure 3 as the inflection point in each site. The Forth valley site is closest to the centre of ice loading and subsequently experienced the maximum uplift and fall in RSL, at more distal sites such as Arisaig the effects of uplift are reduced and therefore the initial fall in RSL is less.

Such modelling conducted at Loch Duart Marsh, the site of study of this thesis, suggests that the Bradley et al., (2011) model underestimates the elevation of RSL over the Late Glacial and Early Holocene and that GIA models need to incorporate thicker ice in the NW sector of the BIIS (Hamilton et al., 2015). Field data including sea-level index points recorded from sites such as isolation basins allow the reconstruction of changes in RSL and provide vital constraints on these models and whilst further work is needed to refine these models, they provide a context to RSL histories and a means of testing the influence of local and global factors.

## 4.3 Isolation basins and the reconstruction of relative sea-level

Isolation basins are natural rock lipped depressions that experience connection or isolation from the sea depending on changes in relative sea level (Lloyd & Evans, 2000). The isolated nature of this basin type is owed to the presence of a typically impervious rock sill separating the basin from open water. Due to the enclosed nature of isolation basins, they are typically low energy environments that preserve fine-grained sediments. This type of basin is particularly useful in sea level reconstruction as during periods where sea level is higher than the elevation of the basin's sill the basin will experience connection to the sea leading to marine sedimentation (Figure 4, T1). When sea level falls to an elevation just below that of the sill the basin will experience periodic connection to the sea at high tide whilst being isolated at low tide. This results in a more complex assemblage of microfossils and other paleoenvironmental proxies as the basin is experiencing marine, brackish and freshwater episodes over a relatively short time (Figure 4, T2). When sea level falls further to an elevation at which even at high tide the basin is not connected to the sea, the basin becomes completely isolated resulting in freshwater sedimentation (Figure 4, T3). Due to the changing conditions within isolation basins in response to RSL differences in the sediments and microfossils preserved contain a record of climate and environmental change as well as changes in RSL (Shennan, 1999). As a result, a variety of sedimentological and biological methods are used to identify periods of isolation and connection. Studies of the microfossil genera preserved within isolation basins have aided paleoenvironmental reconstructions, these commonly employ foraminifera as different species can tolerate varying salinities (Lloyd, 2000; Lloyd & Evans, 2002). Notable work using foraminifera from Loch nan Corr in NW Scotland allowed the reconstruction of Holocene RSL in this area. Further foraminiferal work combining dinoflagellate cysts and thecamoebians allowed the reconstruction of RSL across west and northwest Scotland (e.g., Shennan et al., 2006). Isolation basins have been widely utilised geographically to reconstruct RSL with some

of the earliest work conducted on postglacial lake deposits in Sweden (e.g., Sundelin, 1917). NW Scotland has been the setting of some of the more recent work utilising isolation basins due to their prevalence in the area coupled with the complex RSL history of the region (e.g., Shennan et al., 1994; 1999).

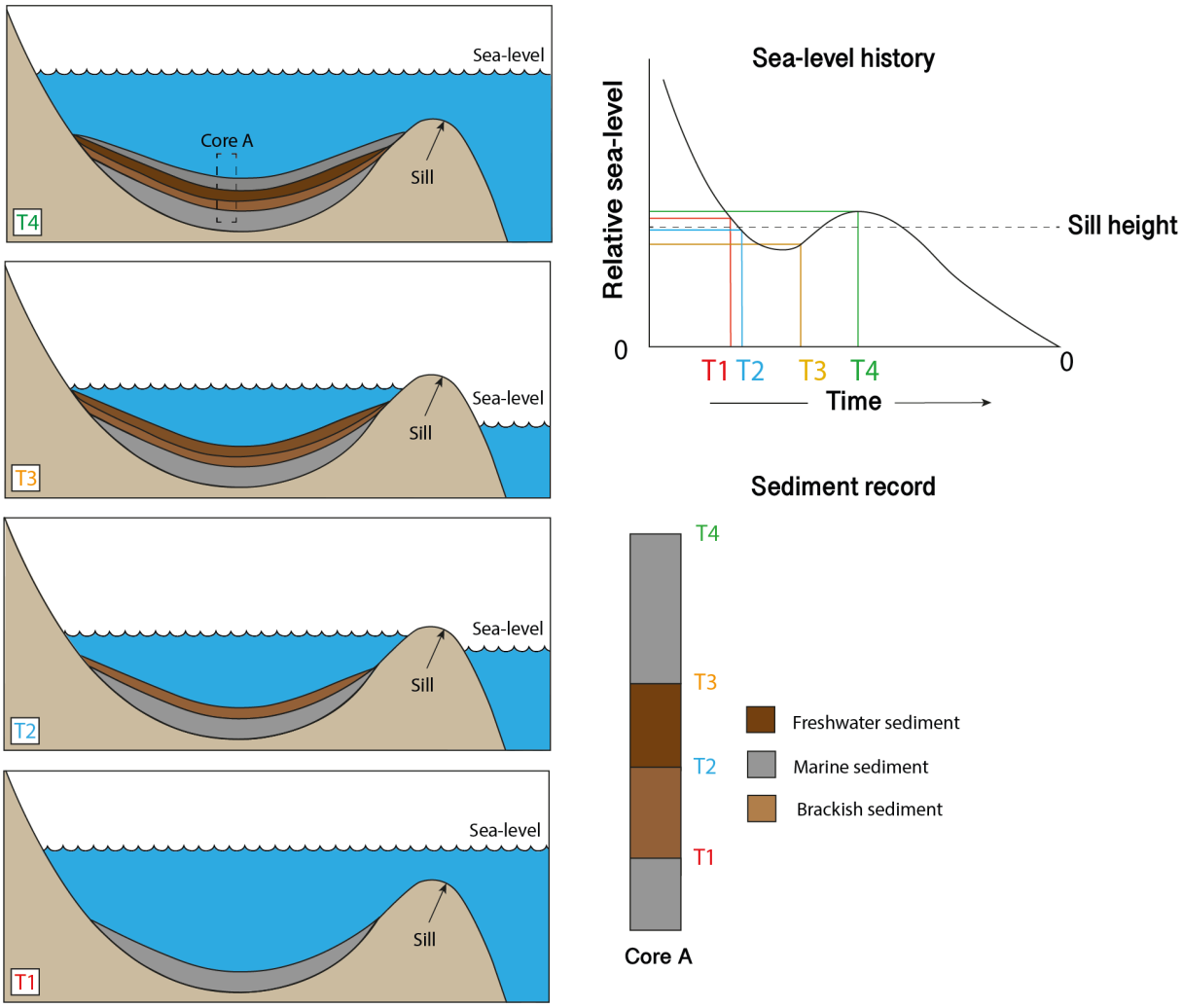


**Figure 4:** Schematic diagram of an isolation basin during changes in RSL. T1 depicts connection of the basin to the open sea and the resultant marine sediment deposited in the basin. At T2 sea level is such that the basin is only connected to the sea at high tide. At T3 RSL has fallen causing the basin to become isolated from the open sea resulting in the deposition of freshwater sediment. T4 sees a subsequent rise in RSL and a return to a marine connection between the basin and open water leading to marine sedimentation once again. The sea-level history graph shows how sea level is changing over time to cause periods of connection and isolation within the basin. The sediment core A catalogues the alternation between periods of marine and freshwater sedimentation; dates at the transition between types of sedimentation as seen on the RSL history graph constrain the timings of RSL rise and fall (adapted from Long et al., 2011 and Zwartz et al., 1998).

In summary, the complex RSL histories across the British Isles, particularly Scotland, resulting from the growth and retreat of the BIIS make the region unique and particularly suited to palaeoenvironmental reconstructions. As discussed traditionally biological proxies such as foraminifera have been utilised for such reconstructions however such efforts are hampered in regions of poor microfossil preservation. In such regions, the conventional biostratigraphic approach to RSL reconstruction is not possible. Therefore, the exploration of other proxies and their ability to reconstruct RSL is imperative to ascertain RSL histories from a wider range of areas, including those previously not understood due to a lack of biostratigraphic evidence. Improving existing and developing new RSL reconstructions through the use of such proxies will better constrain model predictions and improve the understanding of regional RSL and as a consequence glacial history. The development of such proxies will be applicable to basins globally and therefore have far-reaching implications.

## 5. Geographical Location and Study Site

The Assynt region of the UK is situated in northwest Scotland on its western shore. The region is sparsely populated and located due North of Ullapool (Fig. 2). The region is widely regarded as a site of geological scientific interest due to the presence of some of the most ancient lithologies in the UK. Notably, the Lewisian Gneiss comprises much of the bedrock of the Assynt region (Figure 5) which formed during the late Archean, with the north-western edge of the region overlain by Torridonian Group sedimentary rocks (Johnstone & Mykura, 1989). The predominance of crystalline Lewisian basement and subsequent glacial cycles have resulted in characteristic 'knock and lochan' topography as warmed-based glaciers scoured extensive areas creating a setting ideal for lake development (Krabbendam & Bradwell, 2014).

Isolation basins record connection to and isolation from the open sea dependent on relative sea level with freshwater and marine sediments being deposited during periods of regression and ingression respectively (Lloyd, 2000). Sediment sequences from the isolation basin at Loch Duart Marsh on Assynt's North coast (Fig. 1), were investigated in October 2020 based on the initial study of Hamilton et al. (2015). Present-day, Loch Duart Marsh is an elevated saltwater marsh on the western shore of Loch Nedd connected to a tidal basin to the northwest at high tide (Fig. 2). A bedrock sill of Lewisian gneiss exposed at an altitude of 1.95m OD, with overlying boulders, is present at the tidal basin's southern margin where it connects to Loch Duart Marsh only at high tide (Fig. 6). The marsh itself is c. 53 x 23m with a fringing salt marsh surrounded by woodland. The marsh is accessed via a trail extending down from the steep topography of Lewisian Gneiss to the southwest. The sedimentology of Loch Duart Marsh records 15 ka within which a period of isolation is recorded (Hamilton et al., 2015).

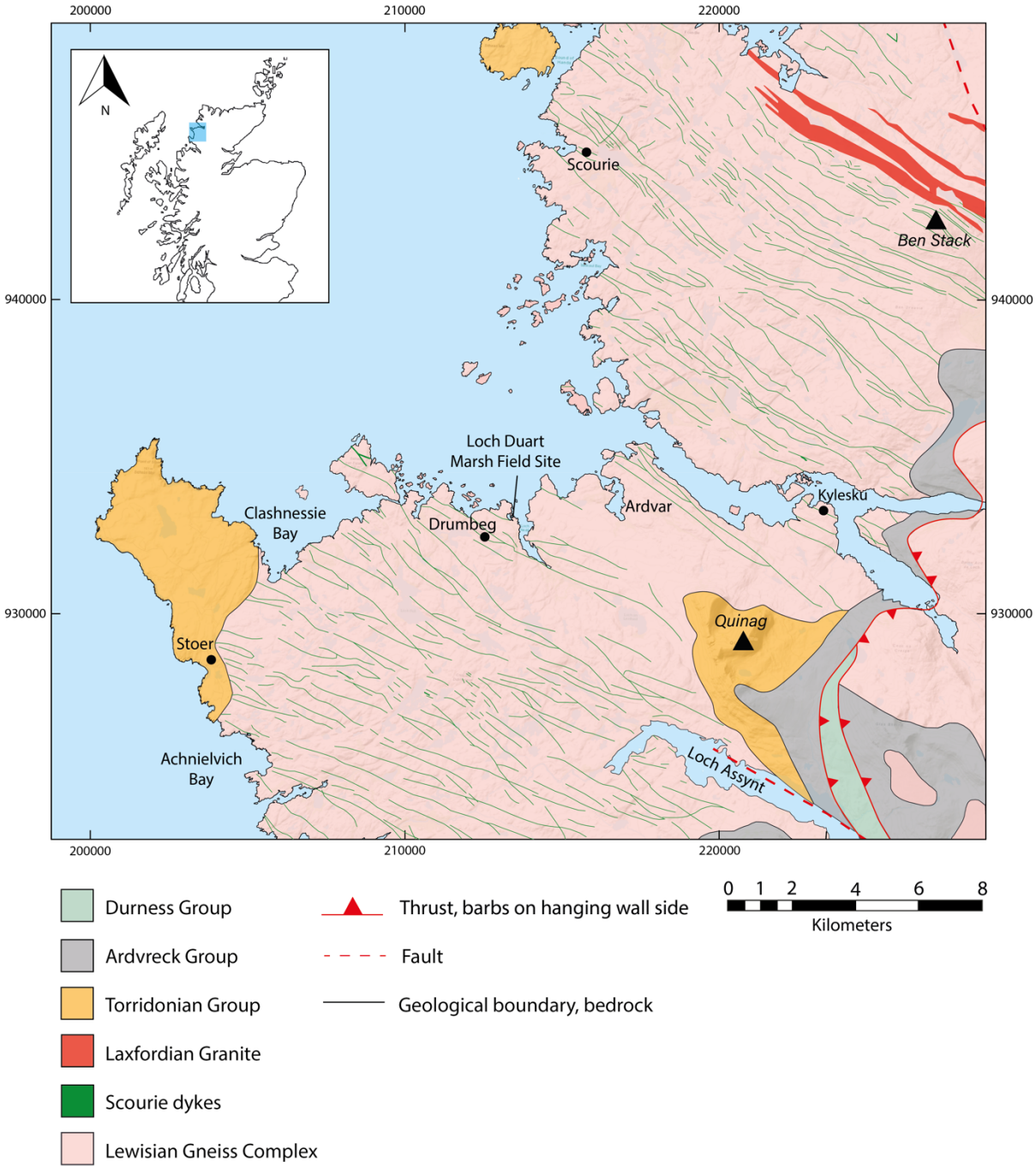


**Figure 5:** Map of Scotland with the location of 7 sites modelled marked by yellow stars the corresponding Map of the region surrounding the field site showing the local geology and geological features with a stratigraphic column to the right showing the local geology and geological features with a stratigraphic column to the right showing the lithologies present. Key locations including the position of the Loch Duart Marsh field site and topographic features. The inset map shows the extent of the map.

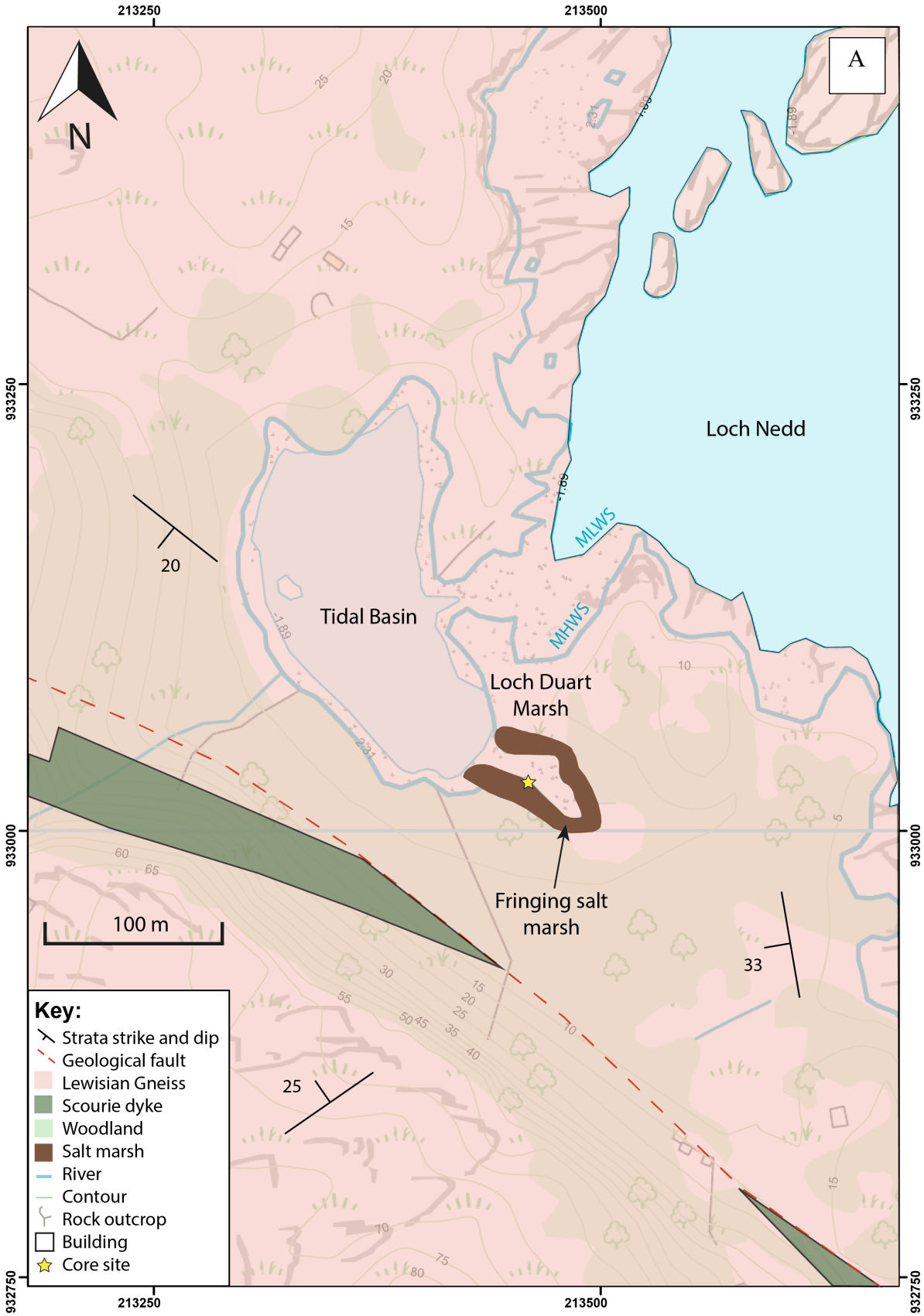
213250
213500
933250
933000
932750
A
N
Loch Nedd
MLWS
MHWS
Tidal Basin
Loch Duart
Marsh
Fringing salt
marsh
20
33
25
100 m
Key:
Strata strike and dip
Geological fault
Lewisian Gneiss
Scourie dyke
Woodland
Salt marsh
River
Contour
Rock outcrop
Building
Core site


**Figure 6:** A – Geological map showing the Loch Duart Marsh Field site with the key lithologies present in the area. The location where the core sections were collected is marked by a yellow star and is the same site as that of Hamilton et al. (2015). B – Aerial photograph of field site area sourced from Digimap.

## 6. Methodology

Previous work at the study site identified stratigraphic changes, the depth of the basin's sill and logged the sediments using the Tröels-Smith (1955) descriptive scheme (Hamilton et al., 2015). Built upon this research, this study collected a new set of cores from the same study site of Hamilton et al. (2015) using a Russian corer. The Russian coring method was chosen as the Russian corer contains the sediment collected within its chamber once collected at the desired depth and therefore the core section is not contaminated by younger sediments when the core section is retrieved. As the Russian corer has a 10 cm nosecone at its base two sites within close proximity of <1 m were cored simultaneously with sections overlapping by at least 10 cm to record and obtain the full stratigraphic section in the region whilst accounting for the disturbance caused by the 10 cm nosecone at the base of the Russian core. The total recovery of the cores was excellent and a total of 5 were used for this study (0-50, 40-90, 120-170, 140-190 and 170-220 cm). The composite stratigraphic log of these core sections is referred to as LDM-20-JT in this study. Once collected the samples were transferred to hard plastic tubes and wrapped in plastic film before transport back to Durham where they were refrigerated upon arrival.

Palaeoenvironmental reconstruction through the core is based upon osmium as an isotopic ($^{187}Os/^{188}Os$) tracer which is supported by foraminifera identification, carbon, sulphur and nitrogen elemental and isotopic analysis together with X-ray fluorescence, CT scanning and radiocarbon dating. Prior to sampling for geochemical analysis, the lower three core sections (120-170, 140-190 and 170-220 cm) were CT scanned using the Geotek X-ray CT core imaging system at the Department of Geography of Durham University. This was used to identify internal sedimentary structures and clasts and to ascertain the boundaries of the lithological units, which in addition to lithological observations, were used to correlate the core of this

study (LDM-JT-20) with that of a previous study at the same field site conducted by Hamilton et al. (2015) (see results for further details).

Each of the five Russian core sections recovered from Loch Duart Marsh underwent X-ray fluorescence analysis in the Geography department at Durham University using the Geotek X-ray fluorescence (XRF) spectrometer. This instrument was used to obtain high-resolution (down and across core resolution of 1 and 5mm, respectively) elemental abundance data from the surface of the sediment cores by bombarding the sample with high energy X-rays. To prepare the cores for XRF scanning the surface to be scanned was flattened by gently using a microscope slide over the core's surface to ensure it was level and free of contamination.

For Re-Os analysis at the Durham Geochemistry Centre (Laboratory for Sulphide and Source Rock Geochronology and Geochemistry and Arthur Holmes Laboratory), samples (N=37) 1 cm in stratigraphic height and 2 cm wide were extracted from the Russian core sections. The samples were oven-dried at 60°C for ~12 hours following this they were ground to a fine powder using an agate pestle and mortar before being passed through a 50 $\mu$m sieve to ensure homogenous grain size of the powdered sample. Between 0.2 and 0.5g of the powdered samples were added to Carius tubes in addition to, a known amount of a mixed $^{190}Os$ and $^{185}Re$ tracer solution and 8 mL of $Cr^{VI}$ –$H_2SO_4$ solution before being heated at 220°C for 48 hours (Selby & Creaser, 2003). The Os was purified using solvent extraction ($CHCl_3$) with back extraction into HBr, and $CrO_3$-$H_2SO_4$-HBr micro-distillation. The Re fraction was purified using NaOH–$C_3H_6O$ solvent extraction and anion chromatography. The Re and Os fractions were loaded onto Ni and Pt filaments, respectively (Selby, 2007). Isotopic measurements were performed using a ThermoElectron TRITON mass spectrometer via static Faraday collection for Re and ion-counting using a secondary electron multiplier in peak-hopping mode for Os.

The total analytical protocol blanks are 11 ± 2 pg for Re, 0.10 ± 0.02 pg for Os, with a $^{187}Os/^{188}Os$ of 0.21 ± 0.03 (1SD, N=4).

For TOC and $\delta^{13}C_{org}$ analysis sedimentary samples (N=26) were acidified with 10% $H_3PO_4$ prior to analysis for organic carbon (%TOC) and $\delta^{13}C_{org}$ in a Costech 4010 Elemental Analyzer coupled to a Thermo Delta V+ via a Conflo IV interface in the Northwestern Stable Isotope Biogeochemistry Laboratory (NUSIBL). Briefly, samples were combusted over a column of $Cr_2O_3$ held at 980ºC and a Cu reduction column held at 705ºC. Elemental information was estimated via cross-calibration with acetanilide organic standards, and $\delta^{13}C_{org}$ was determined via the repeated analyses of Indiana University acetanilide and urea standards (Schimmelmann et al., 2009). Uncertainty estimates from three duplicates in each run are 0.2% for wt% $C_{org}$ and 0.24‰ for $\delta^{13}C_{org}$.

Total sulphur were assayed via combustion in a Costech 4010 Elemental Analyzer coupled to a Thermo Delta V+ mass spectrometer via a Conflo IV interface at NUSIBL. Samples were combusted over a column containing tungstic oxide ($WO_3$ held at 980ºC and wt% S was estimated via cross-calibration with sulfanilidamide standards.

The strong relationship between foraminifera taxa and salinity accurately enables marine, brackish-water and freshwater phases of the isolation process to be characterised (Lloyd, 2000). To isolate and analyse the foraminifera present, sections 1 by 1 cm were taken at stratigraphic intervals of no more than 10 cm. These were then washed with distilled water over 500 $\mu$m and 63 $\mu$m sieves. All foraminifera from the 63–500 $\mu$m fraction were wet picked and counted under a binocular microscope. Taxonomy for foraminifera follows Murray (1971 and 1979).

Radiocarbon dating of both bulk sediment samples and shell fragments from the transition from freshwater to marine deposition provides chronological constraints for the period of marine ingression at this interval. Radiocarbon measurements were conducted by Beta Analytic and calibrated using BetaCal3.21 and MARINE13 calibration curve for the calcareous shell

material and BetaCal4.20 and IntCal20 calibration curve for the plant and organic sediment material (Reimer et al., 2013; Reimer et al., 2020) with the 2-sigma age range reported in Table 1. Radiocarbon measurement on a mixed sample of foraminifera was conducted at Laboratory for the Analysis of Radiocarbon, Bern using MIni CArbon DAting System (MICADAS) AMS (Szidat et al., 2014). The radiocarbon date from the foraminifera sample was subsequently calibrated using the OxCal programme version 4.4 (Bronk Ramsey, 2009) using the MARINE 13 calibration curve (Reimer et al., 2013).

## 7. Results

The results from the LDM-20-JT core collected from Loch Duart Marsh are presented as a summary of the foraminifera, scatter graphs, alongside biplots of C/N and C/S. The radiocarbon-dated transitions of Loch Duart Marsh along with depth age modelling provide an accurate temporal record of sedimentation changes at this site. The core collected is 220 cm in depth and is comprised of four distinct lithological units. Subsequently, the core is divided and discussed in these four units based on changes in the Wt% C, N and S, C/N, $\delta^{13}C_{org}$, $\delta^{34}S$, XRF, $^{187}Os/^{188}Os$ and Re and $^{192}Os$ data; these zones, in general, follow the changes in the foraminifera fauna and broadly lithology (Figs. 7, 8, 9, 10, 11, 12).

The coring sites LDM-13-1 (Hamilton et al., 2015) and LDM-20-JT (this study) are separated by a distance of ~5 m. Given the close proximity of the core sites both cored intervals record virtually identical sedimentology. The stratigraphy is characterised by four units (as recorded by Hamilton et al., 2015), Unit 1 – Late Glacial marine; Unit 2 – Late Glacial to Early-Holocene freshwater; Unit 3 – Early to Late-Holocene marine, and Unit 4 – Late Holocene intertidal (Fig. 7). Here stratigraphic changes (utilising physical sedimentology aided by CT imagery), radiocarbon dates and $^{187}Os/^{188}Os$ are utilised to correlate the two cores (Fig. 7).

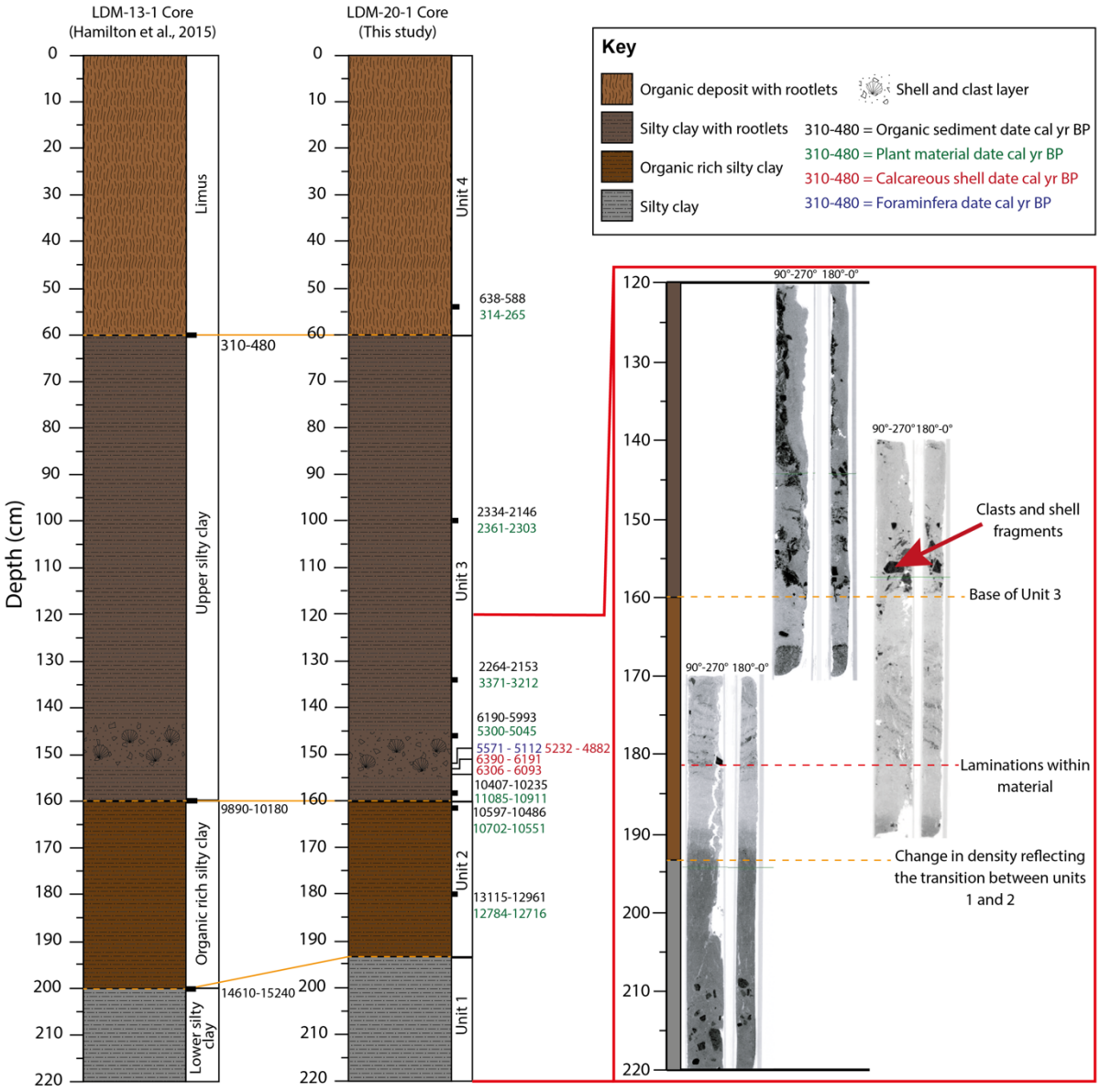


**Figure 7:** A correlation panel of cores LDM-13-1 from Hamilton et al. (2015) and LDM-20-JT from this study. Core images and lithological observations in addition to CT scans of the three stratigraphically deepest core sections (see the exploded view to the right of sections 120-170, 140-190 and 170-220 cm) were used for correlation. Dashed yellow lines represent the lithological correlation.

## Unit 1: Late Glacial marine

Unit 1, the lowermost unit of core LDM-20-JT, spans 220 cm to 193 cm and is characterised by a pale grey silty clay. The grain size at the base of the unit is predominantly clay becoming more silt dominated up section. Laminations and any sediment structures are absent however clasts up to 2 cm in size are visible in the CT scan (Fig. 7). Through the collection and study of these clasts, they were identified as Lewisian gneiss. The thickness of Unit 1 (27 cm) is similar to the lower silty clay unit (20 cm) of LDM-13-1 (Hamilton et al., 2015), with its upper transition with Unit 2 (see below) yielding a radiocarbon bulk sediment age of 14610-15240 cal. yr BP suggesting deposition during the late glacial (Hamilton et al., 2015). The unit lacks abundant foraminifera with only a small number of specimens of *Miliammina fusca* identified at 199 cm, and *Charophyte* oogonia dominating the transition between Units 1 and 2 (Fig. 8). Carbon and nitrogen concentrations are relatively constant throughout Unit 1, with mean values of 1.49 and 0.13 wt%, respectively (Fig. 9). The C/N ratios are relatively low and show little variation up section ranging between 12.13 and 12.41 (Fig. 9). Three $\delta^{13}C_{org}$ analyses show the base of Unit 1 to possess a $\delta^{13}C_{org}$ value of -14.96 ‰, with lighter values (~ -19 ‰) determined for the middle and upper portions of the unit (Fig. 9). Based on the combination of the relatively low $\delta^{13}C_{org}$ and low C/N, Unit 1 plots between the ranges of marine POC, marine DOC and C4 terrestrial plants in Figure 10A with fields defined by carbon source. Unit 1 also plots within the marine field in Figure 10B with fields defined from isolation basin samples from Mackie et al. (2005). Both $\delta^{13}C$ vs. C/N ratio biplots are presented here to identify both carbon source and to compare the results to previous isolation basin studies and the salinity fields generated as a result.

Unit 1 is characterised by low C/S ratios of < 1 in addition to a relatively low total sulphur content of 1.26 to 1.37 wt% with samples from Unit 1 forming a well-defined group within the marine field in C vs S space (Fig. 12).

The XRF elemental counts show homogeneity in Cu across this unit, similarly, Se remains consistent over the lower 25 cm of this unit but increases prior to the transition between units 1 and 2 (Fig. 11). The highest Al, Si, K, Ti, and Fe counts were also recorded in the bottom section of Unit 1, the peaks are present between 210 and 215 cm before a gradual decrease in counts up section.

Rhenium and osmium elemental abundances of Unit 1 range between 1.34 and 3.62 ppb for Re, and 86.8 and 106.3 ppt for Os (Fig. 9). The sampled sections of this unit have moderate to radiogenic $^{187}Os/^{188}Os$ compositions ranging between 1.06 and 2.38 (N = 11). This unit shows a consistent gradual trend to more radiogenic values from 1.06 to 1.41 through the lowermost 16 cm of the unit, with the $^{187}Os/^{188}Os$ values at the upper transition of this unit between 204.5 cm and 195.5 cm showing a more significant shift to more radiogenic values from 1.53 to 2.38 (Fig. 9).

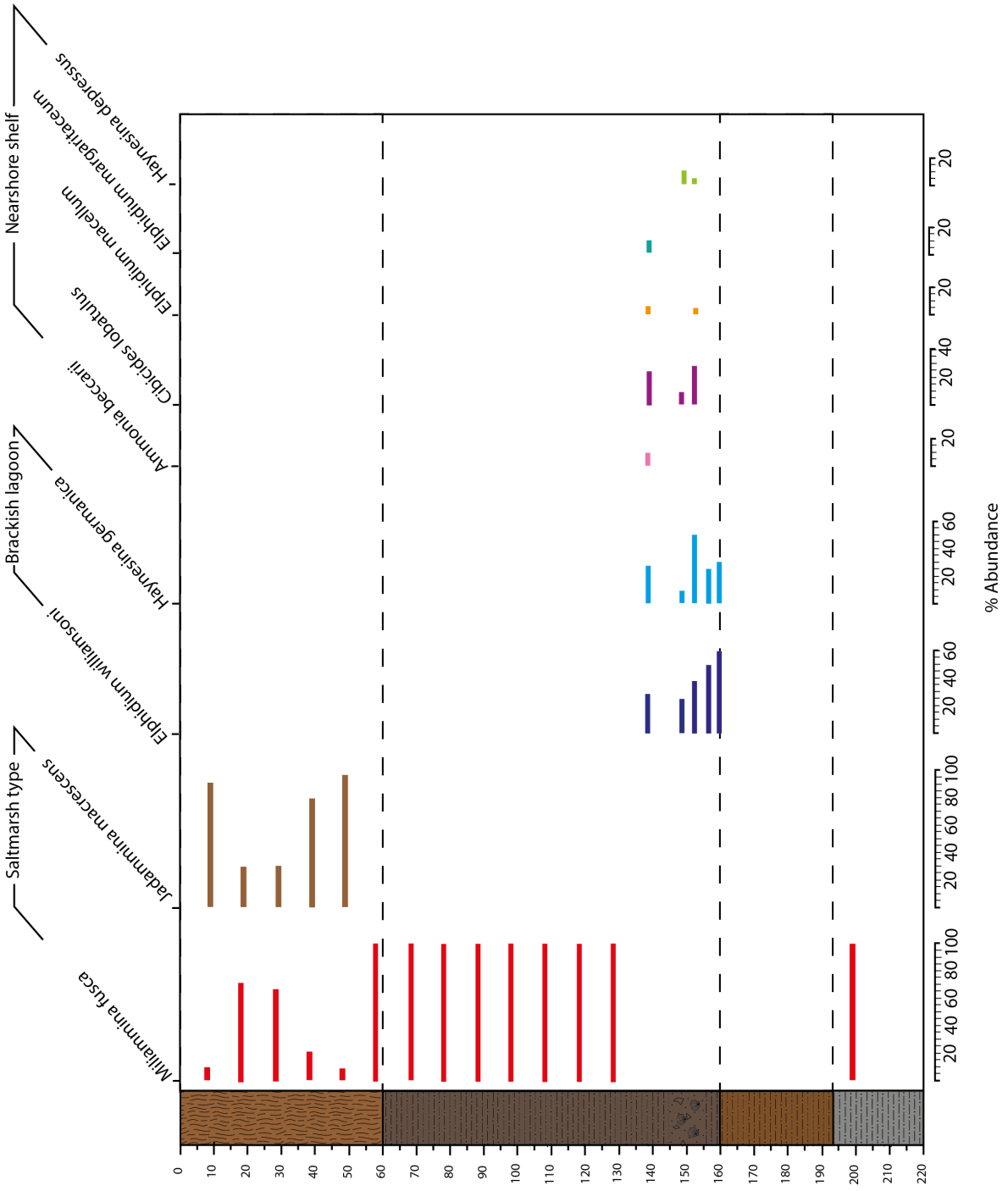


**Figure 8:** Foraminifera assemblage from LDM-20-JT core illustrating the transition from marine to freshwater conditions between Units 1 and 2 and from marine to intertidal between Units 3 and 4. The foraminifera fauna shown in the diagram are represented as percent abundance of the total count. Horizontal dashed lines show sedimentological changes in the core.

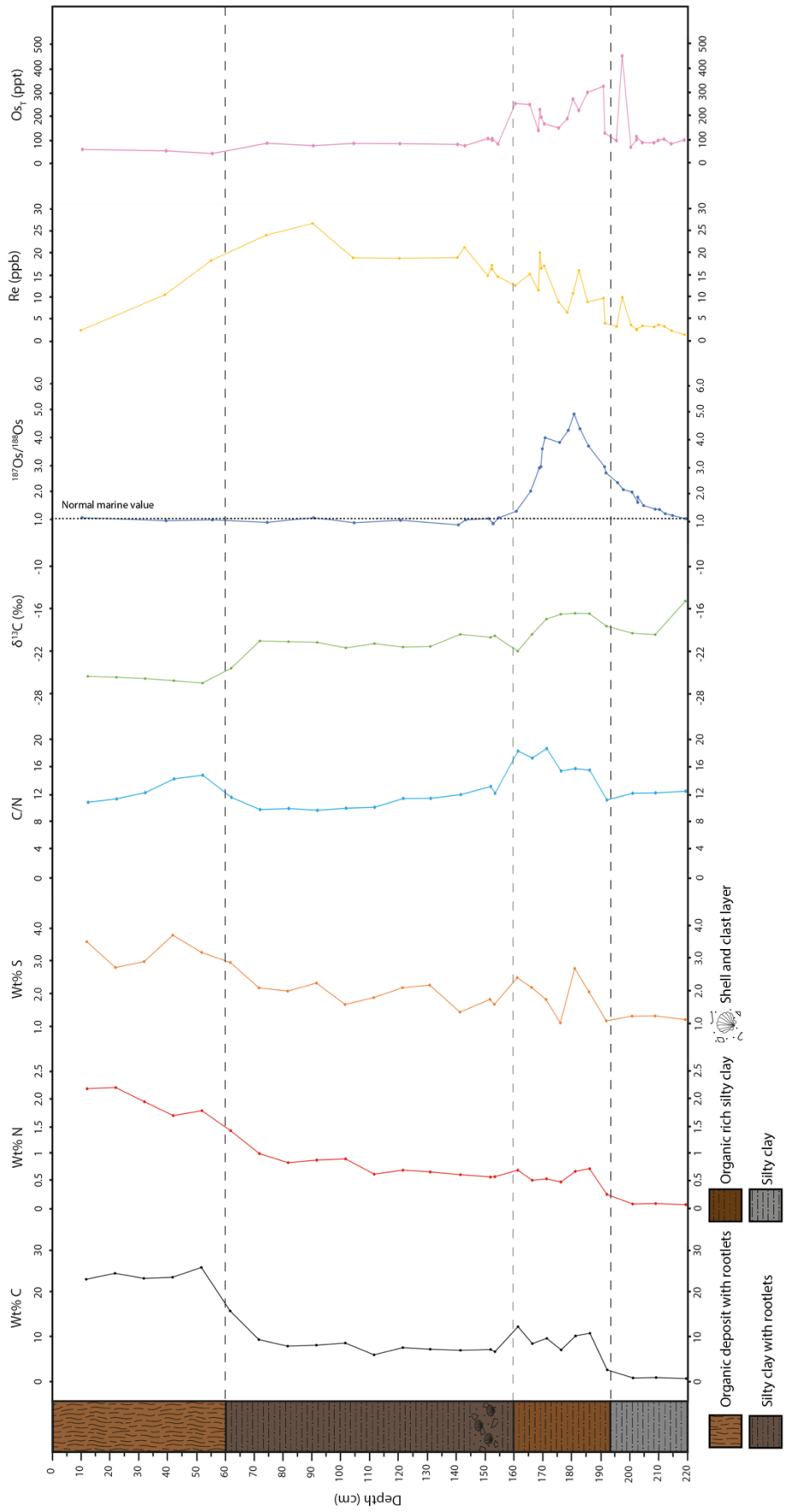


**Figure 9:** Proxy comparison for LDM-20-JT, including wt% C, wt% N, wt% S, C/N, δ C (‰), Os/ Os, Re (ppb) and OsT (ppt) data. Horizontal dotted lines show sedimentological changes in the core.

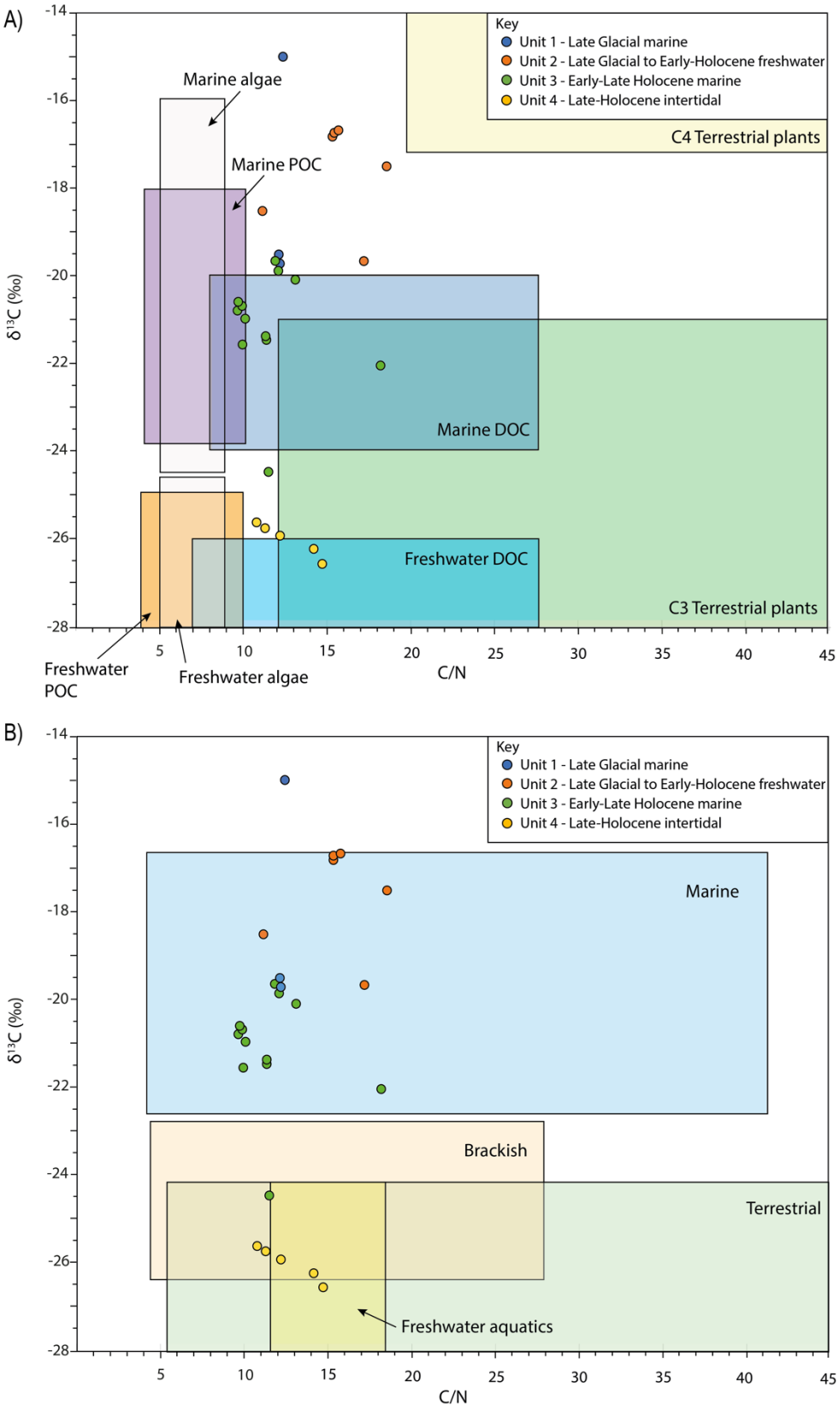


**Figure 10:** C/N and $\delta^{13}C$ from bulk organic material from the LDM-20-JT core. A) The typical $\delta^{13}C$ and C/N ranges for organic inputs to coastal environments fields are based on Lamb et al., (2006). B) The marine, brackish, freshwater aquatics and terrestrial 'fields' of data are taken from Mackie et al. (2005).

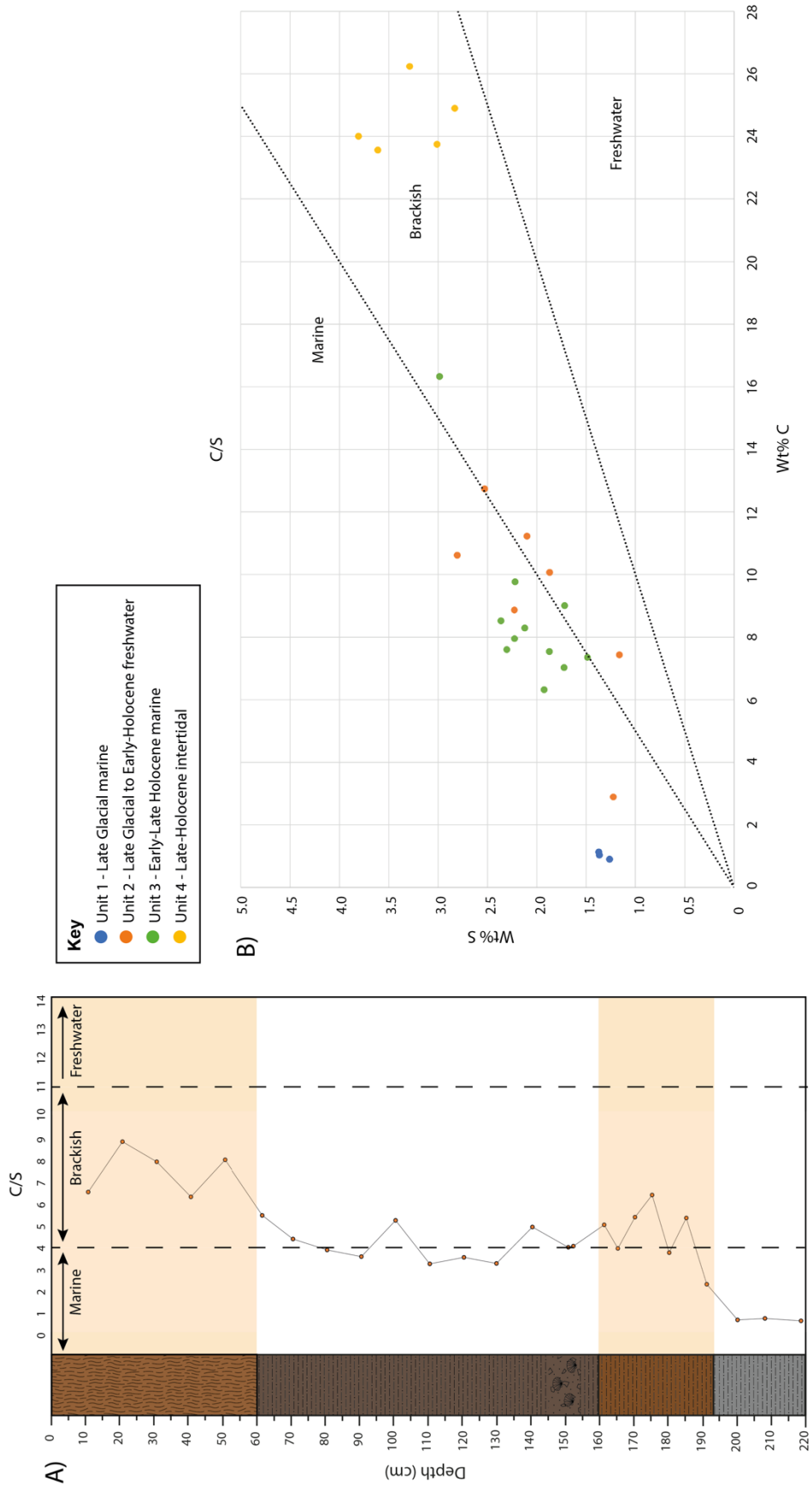


**Figure 11:** Graph of C/S vs stratigraphic depth with marine, brackish and freshwater fields defined by Lee et al., (2021). Box plot of wt% C vs wt% S with the marine, brackish and freshwater fields defined by dashed lines.

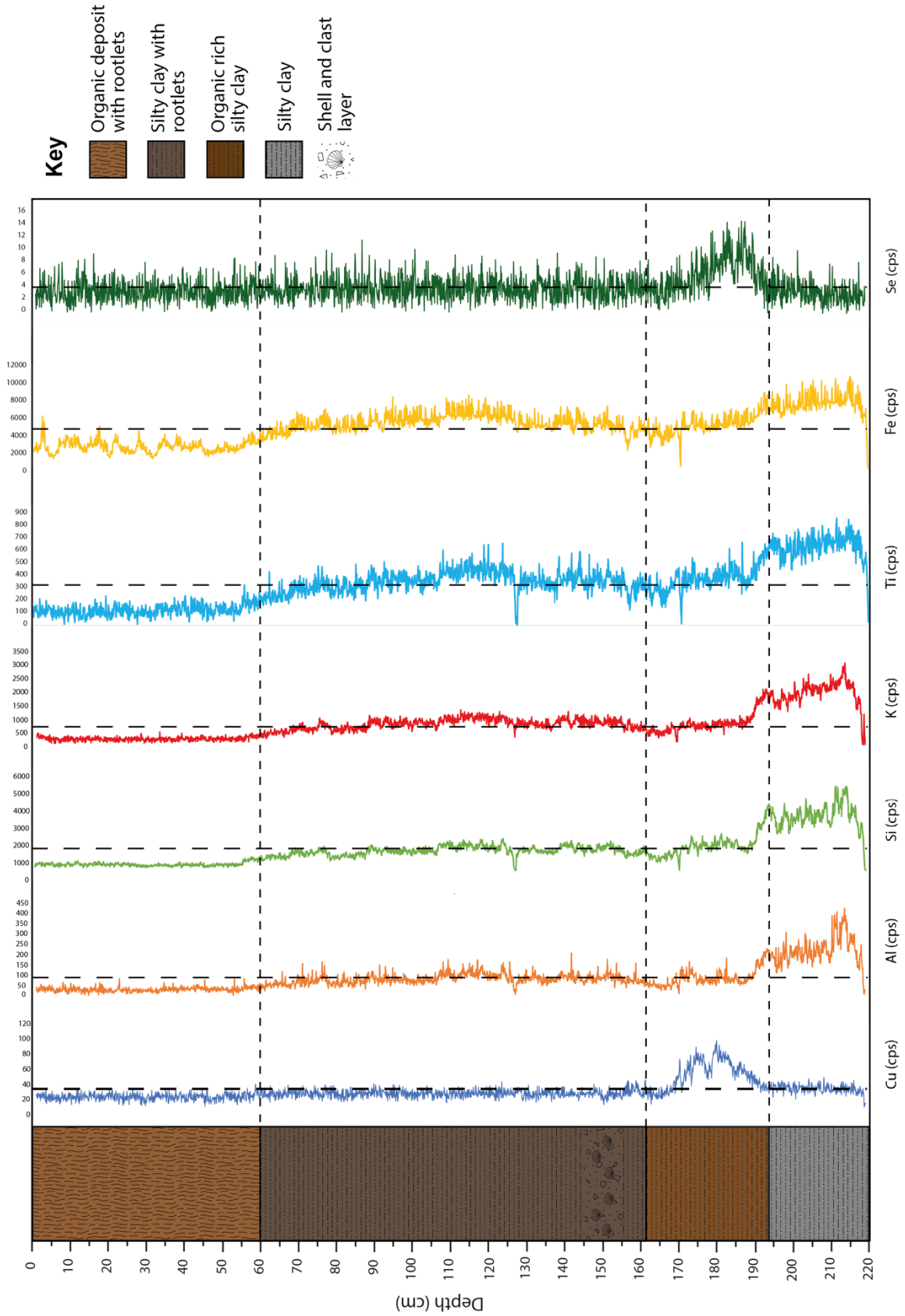


**Figure 12:** XRF scans for eleven elements (Cu, Al, Si, K, Ti, Fe, Se) presented for LDM-20-JT. Horizontal dotted lines show sedimentological changes in the core and vertical dashed lines represent the mean value of the records.

**Table 1:** New Radiocarbon ages from core LDM-20-JT, Loch Duart Marsh, Assynt

| Study site | Laboratory code | $^{14}C$ age ± 2σ ($^{14}C$ yr BP) | Calibrated age (cal yr BP) | Depth in core (cm) | Sample type |
|---|---|---|---|---|---|
| **Loch Duart Marsh** | Beta - 600245 | 560 +/- 30 BP | 638 - 588 | 54 | Organic sediment |
| **Loch Duart Marsh** | Beta - 601750 | 230 +/- 30 BP | 314 - 265 | 54 | Plant material |
| **Loch Duart Marsh** | Beta - 600246 | 2220 +/- 30 BP | 2334 - 2146 | 100 | Organic sediment |
| **Loch Duart Marsh** | Beta - 601751 | 2310 +/- 30 BP | 2361 - 2303 | 100 | Plant material |
| **Loch Duart Marsh** | Beta - 600247 | 2250 +/- 30 BP | 2264 - 2153 | 134 | Organic sediment |
| **Loch Duart Marsh** | Beta - 601752 | 3080 +/- 30 BP | 3371 - 3212 | 134 | Plant material |
| **Loch Duart Marsh** | Beta - 600248 | 5300 +/- 30 BP | 6190 - 5993 | 146 | Organic sediment |
| **Loch Duart Marsh** | Beta - 601753 | 4500 +/- 30 BP | 5300 - 5045 | 146 | Plant material |
| **Loch Duart Marsh** | BE-16154.1.1 | 4907+/- 81 BP | 5571 - 5112 | 153.5 | Foraminifera sample |
| **Loch Duart Marsh** | Beta - 579376 | 4680 +/- 30 BP | 5232 - 4882 | 153.5 | Calcareous shell fragment |
| **Loch Duart Marsh** | Beta - 579374 | 5770 +/- 30 BP | 6390 - 6191 | 154 | Calcareous shell fragment |
| **Loch Duart Marsh** | Beta - 579375 | 5690 +/- 30 BP | 6306 - 6093 | 154.5 | Calcareous shell fragment |
| **Loch Duart Marsh** | Beta - 590878 | 9150 +/- 30 BP | 10407 - 10235 | 158 | Organic sediment |
| **Loch Duart Marsh** | Beta-590335 | 9560 +/- 30 BP | 11085 - 10911 | 158 | Plant material |
| **Loch Duart Marsh** | Beta - 590336 | 9390 +/- 30 BP | 10702 - 10551 | 162 | Plant material |
| **Loch Duart Marsh** | Beta - 590957 | 9330 +/- 30 BP | 10597 - 10486 | 162 | Organic sediment |
| **Loch Duart Marsh** | Beta - 600249 | 11130 +/- 30 BP | 13115 - 12961 | 180 | Organic sediment |
| **Loch Duart Marsh** | Beta - 601754 | 10800 +/- 40 BP | 12784 - 12716 | 180 | Plant material |

## Unit 2: Late Glacial to Early-Holocene freshwater

Unit 2 (193 to 160 cm) is a dark brown, fine-grained organic-rich silty clay. Rootlets are abundant throughout this unit and grain size throughout is predominantly clay, coarsening to silt accompanied by the appearance of laminations between 180 and 170 cm. Within this interval, at 180 cm, plant material and bulk organic ages of 12784 – 12716 and 13115 – 12961 cal yr BP respectively constrain the lower section of Unit 2 as Late Glacial in age. Radiocarbon dates of plant material and bulk organics at 162 cm yield ages of 10702 - 10551 and 10597 - 10486 cal yr BP, respectively, indicating an Early Holocene age for the upper transition of the unit. This unit correlates to the silty clay with organics unit of Hamilton et al. (2015), in this study they recorded a thickness of 42 cm whereas here a 33 cm thickness is recorded likely due to stratigraphic changes across the basin. The radiocarbon ages from Hamilton et al. (2015) and this study are consistent and constrain deposition of this unit to between the Late Glacial and Early-Holocene (Fig. 7). As noted above *Charophyte* oogonia are abundant at the basal transition of this unit. The abundance of *Charophyte* oogonia is only recorded in the basal few centimetres of Unit 2 and no foraminifera are preserved throughout this unit (Fig. 8).

The profiles of carbon and nitrogen follow a similar trend throughout this unit. An increase in both elements is seen across the transition from Unit 1 with peaks at 185.5 cm with values of 11.23 and 0.73 wt% for carbon and nitrogen, respectively. In the uppermost 10 cm of this unit, carbon oscillates between 7.43 and 10.07 wt% before reaching a second peak at 160.5 cm (12.75 wt%) at the upper transition of Unit 2. Nitrogen also varies over this section with 0.48-0.54 wt% recorded between 165.5 and 175.5 cm before a final peak of 0.70 wt% at the transition between Units 2 and 3.

The C/N ratios throughout this unit show an overall increasing trend, from 11.16 to 17.22, between 191.5 cm and 165.5 cm. This trend is punctuated by a brief plateau of ~15.5 between

185.5 and 175.5 cm prior to a notable peak in the C/N ratio at 170.5 cm (18.60). Unit 2 is characterised by a broad peak in $\delta^{13}C$ with an increase in $\delta^{13}C$ values to -16.70 ‰, with values subsequently decreasing to -22.07 at the upper transition to Unit 3. Samples from Unit 2 form a group in C/N vs $\delta^{13}C$ space and sit in and between the marine DOC and C4 terrestrial plant fields defined in Figure 10 A and within the marine field of Figure 10 B.

The wt% S values are highly variable through Unit 2. The section is punctuated by a peak at 180.5 cm (2.80 wt% S) preceding a rapid decrease to 1.16 wt% at 175.5 cm. An overall increasing trend follows over the remaining 15 cm of this section to 2.53 wt% at 160.5 cm. C/S ratios also oscillate throughout this unit between 2.4 and 6.4 with samples largely lying within the brackish field and three samples at 191.5, 180.5 and 165.5 cm within the marine field (Fig. 11). This unit is also characterized by notable peaks in Cu and Se counts between 190 and 165 cm juxtaposed against decreases in Al, Si, K, Ti and Fe (Fig. 12). The rhenium and osmium elemental abundances of this unit range between 3.97 and 20.8 ppb for Re, and 131.8 and 328.5 ppt for Os. This unit is characterised by a significant increase in $^{187}Os/^{188}Os$ values, increasing from 2.73 at the base of the unit to a broad peak with the most radiogenic values recorded in the core over this section. The shift to highly radiogenic $^{187}Os/^{188}Os$ compositions peaks at 4.89 between 191 and 180 cm. Following this peak, a trend towards less radiogenic values is observed with a brief reversal of this trend at 170.5 cm creating a second peak in $^{187}Os/^{188}Os$ values (Fig. 9). The trend to less radiogenic values continues up section with a value of 1.33 recorded at the upper transition of this unit (161 cm).

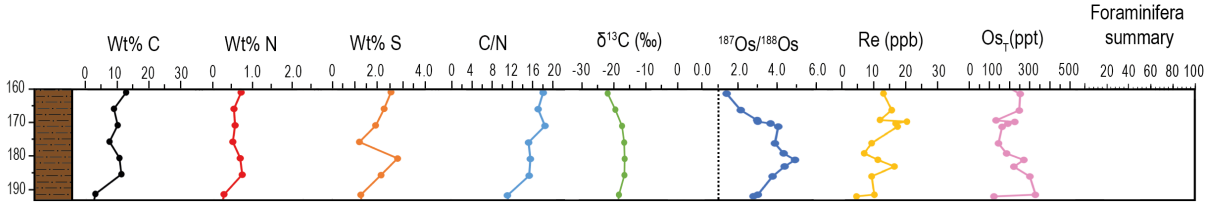


**Figure 13:** Summary diagram of results of Unit 2. Lithostratigraphy, Wt % C, Wt% N, Wt% S, C/N, $\delta^{13}C$, $^{187}Os/^{188}Os$, Re (ppb), $Os_T$ (ppt) and foraminifera summary (see Figure 9 for lithological classification)

## Unit 3: Early-Late Holocene marine

Unit 3 is composed of a dark grey fine-grained silty clay extending between 160 and 60 cm. Within this is a 10 cm layer comprised of clasts and fragmented shells up to 3 cm in diameter present between 145 to 155 cm, the rest of the unit is devoid of any sedimentary structures (Fig. 7). Grain size across the section is predominantly clay with increasing silt content up section. Unit 3 correlates with the upper silty clay unit of the LDM-13-1 core between 158 and 60cm (Hamilton et al., 2015). The lower boundary has been dated in both studies yielding a bulk sediment age of 9890-10180 cal yr BP (Hamilton et al., 2015) and organic sediment and plant material ages from this study (158 cm) of 10407-10235 cal yr BP and 11085-10911 cal yr BP respectively. Both plant material and organic sediment radiocarbon dates throughout Unit 3 at depths of 146, 134 and 100 cm record Middle to Late-Holocene ages further constraining deposition (Table 1). The upper boundary has been dated yielding a bulk sediment age of 310-480 cal yr BP (Hamilton et al., 2015) suggesting that the deposition of Unit 3 occurred from the Early to Late Holocene.

Unit 3 sees the greatest diversity of foraminifera species of the core (Fig. 8). The first species to appear occurring in initially low numbers are *Elphidium williamsoni* and *Haynesina germanica* in addition to a singular specimen of *Haynesina orbiculare*. The abundance of both *Elphidium williamsoni* and *Haynesina germanica* specimens increases up section and they dominate alongside *Cibicides lobatulus* between 160 and 139 cm (Fig. 8). The relative abundance of *Elphidium williamsoni* and *Cibicides lobatulus* decreases from 38.6 % to 22.9 % and from 24.0 to 11.4 %, respectively, between 153.5 and 149.5 cm, whilst *Haynesina germanica* increases from 26.6 to 31.4 %. At a depth of 140 cm within the core, *Elphidium williamsoni, Haynesina germanica* and *Cibicides lobatulus* all exceed 20 % of the total count. *Elphidium macellum*, *Elphidium margeritaceum, Ammonia beccarii* and *Haynesina depressus*

also occur in relatively low numbers between 155 and 139 cm. However, from 130 cm upwards, all calcareous species disappear, and the fauna is dominated by the agglutinated species, *Miliammina fusca* throughout the remainder of this zone, although the number of specimens is low.

In addition to the organic sediment and plant material ages collected from Unit 3, three calcareous shell samples were extracted and dated yielding ages of 5232 - 4882, 6390 - 6191, 6306 – 6093 cal yr BP at depths of 153.5, 154 and 154.5 cm respectively. A sample of mixed foraminifera was also extracted from a depth of 153.5 cm and yielded an age of 5571 – 5112 cal yr BP.

Both C and N show a similar trend with a consistent increase up section, an increase from 7.03 to 9.77 wt % C and 0.70 to 1 wt% N is observed between 152.5 and 70.5 cm. Peaks in both are seen at 60.5 cm with values of 16.34 wt% C and 1.42 wt% N. In Unit 3, there is a sharp decrease in the C/N ratio from the boundary with Unit 2 from 18 to 12. The $\delta^{13}C$ values show a decrease of approximately 2‰ from -20‰ to -22‰ at the transition between Units 2 and 3. Samples from Unit 3 form a well-defined field in the C/N vs. $\delta^{13}C$ plot and sit within the marine DOC field (Fig. 10A). In addition, the samples of Unit 3 cluster within the marine field with only the stratigraphically highest sample (60-61 cm) lying in the centre of the brackish field of Figure 10B.

The abundance of S varies over this section ranging between 1.72 and 2.98 wt%, but broadly increases up section reaching a high of 2.98 wt% at 60.5 cm. Low C/S ratios of between 3.3 and 5.5 are recorded throughout Unit 3 and samples plot between the marine and brackish fields defined in Figure 11. Between 90 cm and 60 cm, an increase in C/S ratio is recorded with samples consistently within the brackish field towards the upper transition of Unit 3.

The XRF elemental counts show no discernible trends in Cu, Al, Si, K, and Se across this section however although consistent, all trends show values marginally higher than recorded in Unit 2. Titanium and Fe are also largely stable, with a slight increase in both present across the centre Unit 3 (Fig. 12). The Re and Os elemental abundances of this unit range between 14.63 and 26.78 ppb for Re, and 78.8 and 108.8 ppt for Os. This unit sees little variation in $^{187}Os/^{188}Os$ with a broadly flat profile up section. Samples from this unit have an $^{187}Os/^{188}Os$ signature of between 0.83 and 1.09 distinctly lower than those of Unit 2 (Fig. 9).

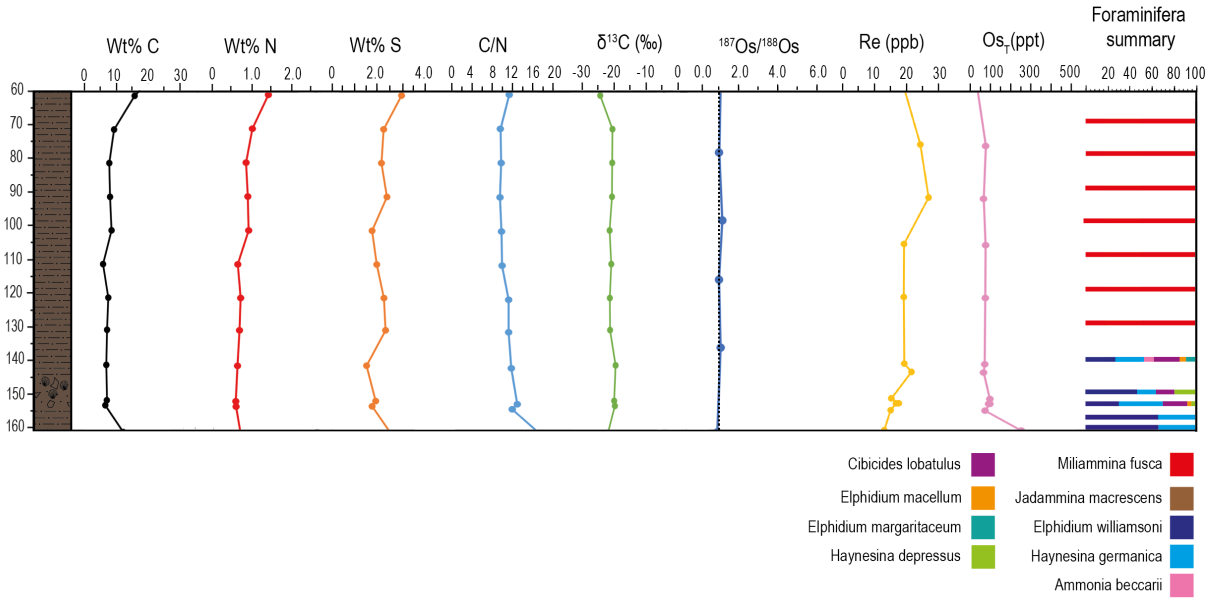


**Figure 14:** Summary diagram of results of Unit 3. Lithostratigraphy, Wt % C, Wt% N, Wt% S, C/N, $\delta^{13}C$, $^{187}Os/^{188}Os$, Re (ppb), $Os_T$ (ppt) and foraminifera summary (see Figure 9 for lithological classification)

## Unit 4: Late-Holocene intertidal

The uppermost unit is a fine-grained organic deposit with rootlets becoming increasingly abundant up section and extends from 60 cm to 0 cm. Unit 4 correlates to the limus lithological unit of Hamilton et al. (2015) and both are an identical thickness (Fig. 7). As discussed, the transition between Units 3 and 4 dates to the Late-Holocene, organic sediment and plant material radiocarbon ages at 54 cm conducted in this study yield ages of 638-588 cal yr BP and 314-266 cal yr BP respectively further supporting a Late-Holocene age for Unit 4.

A total of six samples were analysed with two foraminifera species identified to determine the biostratigraphy of Unit 4. Throughout the unit, *Miliammina fusca* and *Jadammina macrescens* are present with the latter generally more dominant throughout the section. At the base of this unit, *Miliammina fusca* is the only species present, however, up section *Jadammina macrescens* appears and dominates the section comprising 92% of the total count at 49.5 cm. The abundance of *Jadammina macrescens* subsequently decreases to 30-33 % of the total count between 29.5 cm and 19.5 cm whilst *Miliammina fusca* becomes more dominant. *Jadammina macrescens* regains dominance at the uppermost section of this unit increasing to 91 % of the total count at 9.5 cm (Fig. 8).

Carbon in Unit 4 varies between 23.56 and 26.24 wt% which is significantly higher compared to the lower values of Unit 3. A sharp increase from 9.77 wt% at 70.5 cm to a peak of 26.24 wt% at 50.5 cm is present across the transition between Units 3 and 4 (Fig. 9). In Unit 4 nitrogen is the highest of the 4 units comprising the core with values between 1.78 and 2.20 wt%. An overall increasing trend, from 1.78 to 2.18 wt%, between 50.5 cm and the surface is seen (Fig. 9). This trend is interrupted by a decrease in nitrogen content at 40.5 cm (1.69 wt%). Unit 4 has relatively low $\delta^{13}C$ values between -26.59 and -25.65 ‰. A peak in C/N ratios of 14.2 to

14.7 between 40.5 and 50.5 cm is followed by a gradual decrease to lower values up section falling to 10.82 at 10.5 cm. In $\delta^{13}C$ vs C/N space, the samples plot into and just above the freshwater DOC field (Fig. 10A). Additionally, the samples form a defined group within the overlapping brackish, freshwater aquatic and terrestrial fields of Figure 10B.

In Unit 4 sulphur varies with two peaks at 40.5 cm (3.81 wt%) and 10.5 cm (3.61 wt%) bracketing lower values of 2.83 - 3.01 wt% (Fig. 9). The relatively high C/S ratios of Unit 4 mean the samples form a well-defined group within the brackish field defined in Figures 11A & B.

The XRF elemental counts show no apparent trend in Cu, Al, Si, K, Ti, Fe, and Se between 55 cm and the surface of the core, however, a gradual decrease in these elements is recorded in the lower 5 cm of Unit 4 being most pronounced in Ti and Fe (Fig. 12). The elemental abundance of osmium shows a similar trend with values of 46.2 – 63 ppt whereas rhenium decreases up section from 18.30 to 2.37 ppb. The $^{187}Os/^{188}Os$ compositions are relatively constant throughout the unit ranging from 0.98 to 1.09 (Fig. 9).

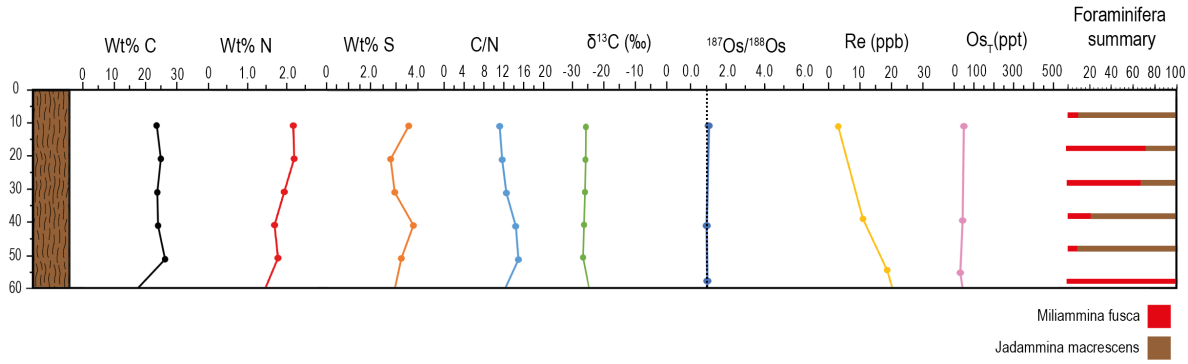


**Figure 15:** Summary diagram of results of Unit 4. Lithostratigraphy, Wt % C, Wt% N, Wt% S, C/N, $\delta^{13}C$, $^{187}Os/^{188}Os$, Re (ppb), $Os_T$ (ppt) and foraminifera summary (see Figure 9 for lithological classification)

# 8. Discussion

This chapter presents the interpretations and implications of the proxies used to understand the palaeoenvironment of the Loch Duart Marsh core based on the results presented in the previous chapter. An age-depth model with calculated sedimentation rates is presented to constrain the history of sedimentation throughout the core. In addition, the common practice of utilising biostratigraphic evidence, in this study foraminifera, for RSL reconstruction is paralleled with XRF and isotopic proxies to assess both evaluate their potential for palaeoenvironmental reconstruction.

## 8.1 Age depth model

As presented in the previous chapter, 18 samples were radiocarbon dated throughout the core using bulk sediment, plant, foraminifera, and calcareous shell material (Table 1). All 18 dates from this study were combined with the bulk sediment dates at 160 and 195 cm from Hamilton et al. (2015) and used to determine the most accurate temporal model of sedimentation and establish an age-depth model spanning the past 15000 years. Using the Bayesian approach using the rbacon package in R to create an age-depth model 80% of the dates were determined to overlap with the age-depth model. This age-depth model is supported by the close agreement between the chronology presented here and that of Hamilton et al. (2015). Firstly, the bulk organic samples of the Hamilton et al. (2015) study produced similar radiocarbon ages to those presented here. Secondly, the sea-level curve produced by Hamilton et al. (2015) is consistent with other dated contacts of nearby sites and agrees with GIA model predictions during the Mid to Late-Holocene.

The age-depth model (Fig. 16) of calibrated ages (see Table 1) suggests a consistent sedimentation rate of 0.01 cm/yr throughout Unit 1 which spans 17289 to 14511 cal yr BP (determined using age-depth model see Figure 16). Sedimentation remains broadly consistent throughout Unit 2 with an average sedimentation rate of 0.008 cm/yr with this unit spanning 14511 to 10230 cal yr BP. The sedimentation rate increases briefly at the transition between Unit's 2 and 3 between 163 and 156 cm to 0.014 cm/yr. This increase suggests a change in sedimentary environment and supports the interpretation of a transition from a freshwater to marine setting across these units (Hamilton et al., 2015). A rise in sea level, which agrees with the sea-level curve produced by Hamilton et al. (2015), resulted in marine inundation causing increased sedimentation rates and increased transport of inorganic material into the basin across the boundary between Unit 2 and Unit 3. The sedimentation rate varies throughout Unit 3 and a hiatus in sedimentation is inferred at 155.5 cm. This hiatus is inferred as organic and plant material dates from a depth of 158 cm yield ages of 10407 – 10235 and 11085 – 10911 cal yr BP respectively whilst just 3.5 cm stratigraphically higher in the core a calcareous shell fragment yielded an age of 6306 – 6093 cal yr BP. This shell age is in close agreement with two other calcareous shell fragments collected at 154 cm (6390 – 6191 cal yr BP) and 153.5 cm (5232 – 4882 cal yr BP) in addition to a foraminifera radiocarbon date at 153.5 cm (5571 – 5112 cal yr BP). Such a dramatic shift to younger radiocarbon dates over such a short stratigraphic interval is not coherent with the age-depth relationship of the rest of the core, therefore, implying a hiatus at this time. Furthermore, without including a hiatus the age-depth model created in rbacon yields a model with which only 70% of the dates overlap whereas with a hiatus included at 155.5 cm 80% of the dates overlap with the model. The hiatus was determined to be at 155.5 cm as this depth best satisfied the age-depth model. This proposed hiatus in sedimentation coincides with the base of the shell and clast layer within Unit 3 suggesting an erosional surface is present at this depth. This combined with the abundance of

broken shells and clasts within the 10 cm layer between 145 and 155 cm suggests a high energy erosive event such as a storm. This inferred erosive event occurs within Unit 3 rather than at its base suggesting it is not the result of sudden marine ingression into the basin. Furthermore, the abundance of reworked shells and clasts is not seen throughout the rest of the core suggesting a high energy event transported them. The exact nature of this event is beyond the scope of this study as no regional event is known to be contemporaneous with this hiatus, this study estimates 35 cm of sediment was removed during the event and the available chronology determined through this study indicates this event occurred between 8787 and 6509 cal yr BP (estimated from the age-depth model Fig. 16). Further research on this core interval should aim to elucidate the cause and absolute timing of the erosive event. Within Unit 3 a sedimentation rate of 0.033 cm/yr on average is recorded between 133 and 100 cm. This relatively high sedimentation rate at 133 cm correlates with a marked transition in foraminifera species from calcareous to agglutinated forms. This change in foraminifera fauna combined with the gradual decrease up section in sedimentation rate to 0.022 cm/yr is interpreted to reflect a reduced input of sediment into the basin likely the result of a gradual fall in sea level. This is as during periods of lower sea level infilling of sediment reduces accommodation space within basins resulting in reduced sedimentation rates (Rasmussen et al., 2020). This is supported by the sea-level curve produced by Hamilton et al. (2015). This trend continues into Unit 4 with a sedimentation rate of 0.024 cm/yr (Fig. 16).

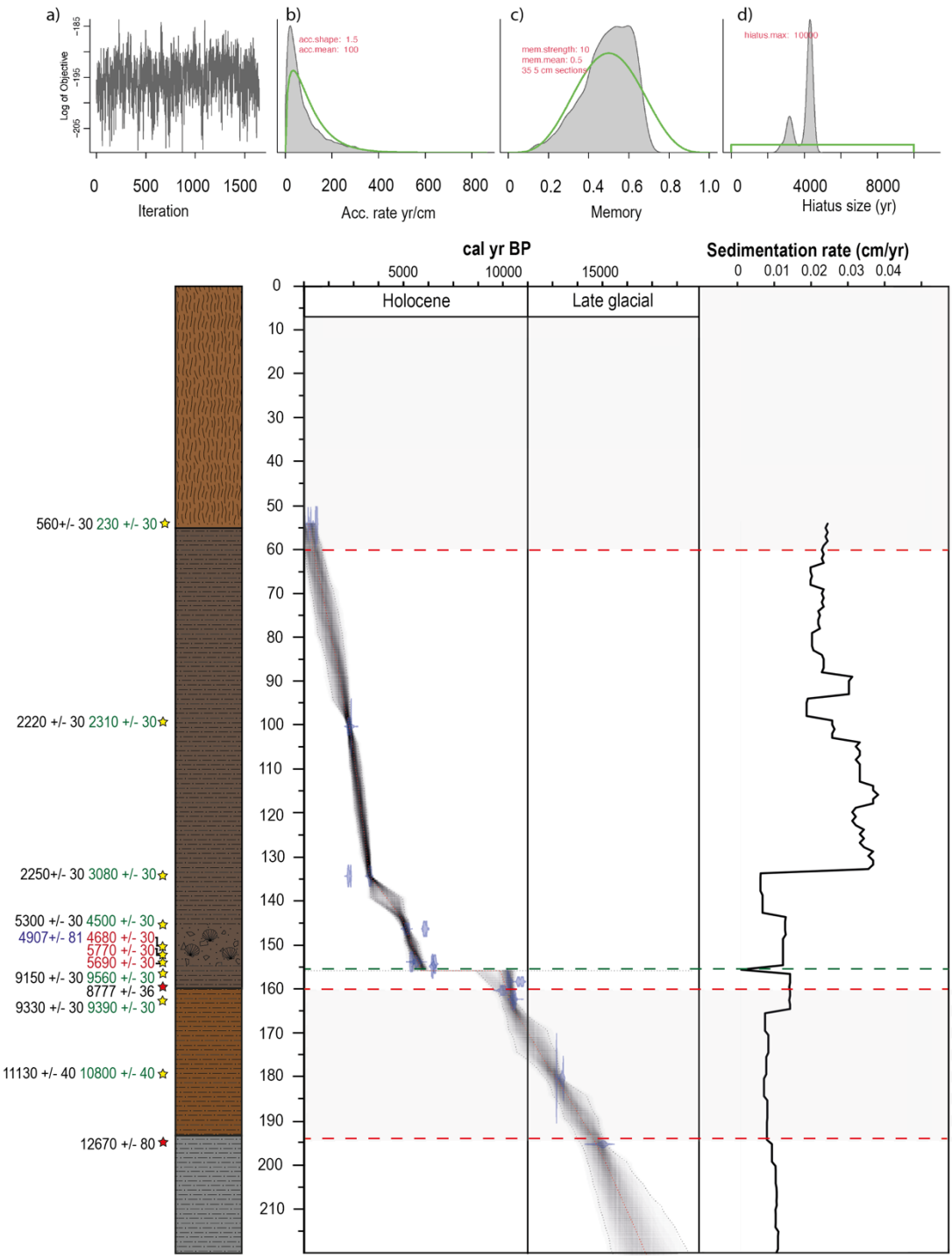


**Figure 16:** Age model for the LDM-20-JT core using rbacon (Blaauw & Christen, 2011) package (version 2.3.9.1) in R. Organic sediment (black), plant material (green), shell (red) and foraminifera (blue) radiocarbon ages are shown with ages from this study (yellow star) and those from Hamilton et al. (2015) (red star). The age-depth model shows calibrated $^{14}C$ ages depicted in blue with the most accurate age model presented by a red dotted line. The grey stippled lines indicate 95% confidence intervals. Calculated sedimentation rates are depicted on the adjacent plot. Plot A depicts iteration history, plots B and C show prior, depicted by green lines, and posterior, shown by grey histograms, distributions for accumulation rate (Plot B), memory (Plot C) and hiatus size (Plot D).

## 8.2 Faunal interpretation from Loch Duart Marsh

Unit 1 lacks abundant foraminifera fauna with only a limited number of specimens of *Miliammina fusca* identified at 199 cm indicating brackish conditions. The lower samples within this zone are barren of foraminifera however Hamilton et al. (2015) found brackish and fully marine diatom species in this section of the core implying marine deposition. One sample from 199 cm has 10 specimens of *Milliamina fusca*, a species that is found in brackish environments, often close to the transition to freshwater conditions. This indicates Unit 1 experienced at least some marine influence. The presence of only *Miliammina fusca* near the upper boundary of Unit 1 implies the transition between Unit 1 and Unit 2 was deposited during the period just prior to final isolation from marine inundation as this species has been suggested to be one that can tolerate the lowest salinity and most highly variable conditions likely due to its infaunal mode of life, such conditions are plausible during the final stages of basin isolation (Lloyd & Evans, 2002).

The transition between Units 1 and 2 is dominated by the oogonia of *charophytes*, green algae which live submerged in fresh and brackish water (Moore, 1986). The freshwater habitat of *charophyte* oogonia suggests an influx of freshwater during the transition to Unit 2. This unit is barren of any foraminifera implying that marine inundation has ceased, and the basin has now entered a phase of isolation and is entirely freshwater. This absence of foraminifera coupled with the presence of *charophyte* oogonia within Unit 2 provides biostratigraphic evidence that supports the conclusion of a period of freshwater sedimentation as a result of basin isolation during the Late Glacial as suggested by the diatom flora presented by Hamilton et al. (2015).

Unit 3 sees the greatest diversity of foraminifera within the core. A significant increase in diversity is recorded with 7 different species present, dominated by *Elphidium williamsoni* and

*Haynesina germanica*, but with *Cibicides lobatulus* also common (Fig. 8). *Haynesina germanica* is a euryhaline species able to tolerate very low salinities ranging from 0 to 35‰ and is common in brackish lagoons and estuaries (Murray, 1979). Similarly, *Elphidium williamsoni* is a brackish lagoonal or estuarine species therefore its dominance at the base of Unit 3 implies the inundation of the basin by the sea during the Early Holocene.

The dominant species present between 155 and 140 cm are those that prefer fully marine conditions including *Elphidium macellum, Cibicides lobatulus* in addition to the less abundant *Elphidium margeritaceum*. The introduction of species preferring fully marine conditions suggests continued marine inundation across the basin sill related to a relative sea-level rise associated with global melting of mid-latitude ice masses at this time (10259 to 4497 cal yr BP between 160 and 140 cm estimated from the age-depth model Fig. 16). In summary, 160 to 140 cm records the highest abundance and diversity of species with some of the species indicative of normal marine salinity, but the dominant species indicative of brackish lagoonal/estuarine conditions. This point, therefore, marks the maximum marine transgression during the Holocene in this area. At 153.5 cm the foraminifera abundance rapidly increases resulting in the highest abundance of foraminifera within the core.

Above 130 cm Unit 3 shows a significant reduction in species diversity. The foraminiferal species discussed that favour fully marine conditions disappear and *Miliammina fusca* dominates the foraminiferal assemblage, but the number of specimens is low. The rapid decrease in diversity coupled with the dominance of *Miliammina fusca*, a species with a wide-ranging salinity tolerance indicates a change from a basin with near marine salinity to one with clearly reduced and varying salinity. This is controlled by tidal inundation at high tides and leads to a dilution of the marine water by freshwater from the surrounding drainage basin. This trend continues into Unit 4 with an assemblage dominated by *Miliammina fusca* at the transition between Units 3 and 4 showing the continued removal of marine conditions. As sea

level continues to fall, tidal inundation is reduced, perhaps only occurring at high tide. The reduction in basin water salinity and perhaps an increase in the variability of conditions cause the change in the fauna inhabiting the basin. *Jadammina macrescens* is a euryhaline species often associated with upper salt marsh environments (Scott & Medioli, 1980). *Jadammina macrescens* has been found in modern tidal lagoons at the limit of marine inundation therefore its presence implies a lagoonal setting that is close to freshwater conditions (Lloyd & Evans, 2002). The site today is actually at the transition from a lagoon to a saltmarsh suggesting that the lagoon has since been infilled by sedimentation and the site has transitioned to a modern-day saltmarsh environment.

Foraminifera assemblage analysis has typically been relied upon as it is one facet of the biostratigraphic approach to understanding past sea-level change with clear records of sea level depicted through changes in the dominant species of foraminifera across a site (e.g., Shennan et al., 2000; Lloyd & Evans, 2002). Therefore, the environmental interpretations from this robust proxy discussed above will be compared with those from more novel methods not reliant on biostratigraphy to ascertain their merit.

## 8.3 $\delta^{13}C$ and C/N

The interpretations based on biostratigraphic evidence both from the diatom analysis of Hamilton et al. (2015) and the foraminifera analysis presented here suggest an initial period of marine deposition within the basin before isolation of the basin resulting in subsequent freshwater deposition as a result of RSL fall. Subsequently, the microfossil evidence suggests a return to marine conditions following a rise in RSL with a gradual reduction in marine influence across the Mid to Late-Holocene.

One approach to environmental reconstruction not reliant on microfossils is the use of stable carbon isotopes ($\delta^{13}C$) and C/N ratios from bulk organic matter. These geochemical proxies possess the ability to provide information regarding the source of organic material and carbon storage in coastal environments (e.g., Müller & Mathesius, 1999; Andrews et al., 2000). Building on this work the technique has been developed and applied to Holocene sediments to interpret palaeosalinity and consequently changes in relative sea level through the examination of coastal sediments (Emeis et al., 2003; Khan et al., 2019). Specific to this study is the application of $\delta^{13}C$ and C/N to Late Quaternary isolation basin sediments as a result of their ability to distinguish changes in the origin of organic matter (e.g., Mackie et al., 2005; Leng & Lewis, 2017). Mackie et al. (2005) linked $\delta^{13}C$ to salinity and further defined freshwater (-33 to -24 ‰), brackish (-26 to -22‰) and marine (-22 to -17 ‰) $\delta^{13}C$ fields (Fig. 10B). The change in the dominant carbon source between terrestrial and marine is recorded in the sedimentary sequences recovered from isolation basins and used to infer marine ingression and regressions and consequently RSL.

Low C/N values 4-10 indicate algal aquatic material which can be marine or freshwater in origin, higher C/N values >20 indicate higher-order plant material typically terrestrial

vegetation (Meyers, 1994). Unit 1 is defined by relatively high $\delta^{13}C$ values (-19.73 ‰ to -14.96 ‰) and low C/N ratios (12.13 -12.41) (Fig. 10). Based on the fields defined in Figure 10A, the majority of the samples plot between the ranges of marine POC, marine DOC and C4 terrestrial plants, indicating a mixed source largely dominated by marine POC and DOC input with perhaps to a lesser extent an influence from C4 terrestrial plants. In addition, the cluster of samples from Unit 1 within the marine field of Figure 10B supports the interpretation of marine deposition of this unit.

In contrast to Unit 1, Unit 2 has relatively high C/N ratios and high $\delta^{13}C$ values with peaks in both occurring over this unit recording the highest values within the core. In addition, the increase in wt% C (from 4 to 18 %) between Units 1 and 2 is likely due to an increase in productivity within the basin associated with the change in the aquatic environment. A subsequent decrease in wt% C from 10.62 to 7.43 % between 180.5 and 170.5 cm suggests a brief decrease in productivity at this time. Utilising this study's age-depth model this decrease is found to be contemporaneous with the Loch Lomond Stadial suggesting this decrease in productivity and therefore wt% C may be due to the cooler climate. This is in agreement with Hamilton et al. (2015) which noted a reduction in organic carbon at a similar depth. Similar findings linking reduced organic content to the Loch Lomond Stadial have been noted in North Scotland (Sissons, 1979; Timms et al., 2021). The shift to higher C/N ratios in this unit indicates a shift to a greater input of higher-order plant material (typically terrestrial vegetation rather than aquatic algae) in the organic fraction. This supports the interpretation of a transition to freshwater conditions as a reduction in marine algal contribution is replaced by an increase in terrestrial plant organic matter that is both washed into the isolation basin and associated with the growth of freshwater aquatic plants. The high $\delta^{13}C$ values of this unit mean the samples do not plot within the freshwater fields of the $\delta^{13}C$ vs C/N plots (Fig. 10A & B) as would be expected based on the biostratigraphic data from this study (absence of foraminifera and

abundance of *charophyte* oogonia at the transition to Unit 2). Samples from this unit instead cluster towards the C4 terrestrial field. Previous work on Unit 2 at Loch Duart identified the presence of the aquatic plant *Myriophyllum alterniflorum* at a depth of 195 cm (Hamilton et al., 2015). The $\delta^{13}C$ signature of this aquatic plant has been recorded to have a median of -18‰ and an interquartile range of between -22 and -12 ‰ (Chappuis et al., 2017). Therefore, the dominance of *Myriophyllum alterniflorum* within this unit is the likely cause of the relatively high $\delta^{13}C$ signature of Unit 2 compared to the adjacent units and offers an explanation as to why the samples lie outside the freshwater DOC, POC and algae fields.

Unit 3 is characterised by $\delta^{13}C$ and C/N values that plot largely within the marine DOC and marine POC fields with only two samples falling above the marine DOC field. The sharp decline in C/N ratios at the transition between Units 2 and 3 coupled with the slight increase in $\delta^{13}C$ over the same section suggests an increase in the amount of marine organic material and a decrease in freshwater/terrestrial organic material. The broadly consistent trends in both $\delta^{13}C$ and C/N over this unit suggests marine deposition. At 70 cm a decline in $\delta^{13}C$ coupled with an increase in C/N ratios suggests a decrease in the amount of marine organic matter, and an increase in freshwater aquatic and terrestrial organic matter at the transition between Units 3 and 4. Furthermore, the samples of Unit 3 cluster within the marine field with one sample lying in the centre of the brackish field of figure 10B which supports the interpretation of the marine deposition of Unit 3 with a decreasing marine influence up section.

The increase in C/N ratios and decrease in $\delta^{13}C$ values continues into Unit 4 with a maximum peak in C/N accompanied by a trough in $\delta^{13}C$ recorded at 50cm suggesting a further decrease in the input of marine organic matter and the increase in freshwater carbon inputs. Whilst the samples of Unit 4 cluster within and adjacent to freshwater DOC and C3 terrestrial plant fields three of the samples have higher $\delta^{13}C$ than the freshwater DOC field suggesting another phase

of increased marine organic carbon input. The $\delta^{13}C$ signature of Unit 4 is the lowest recorded throughout the core and with values significantly lower than those recorded within Unit 3 which has an inferred marine depositional setting this implies that Unit 4 was deposited in a less marine-influenced environment, but that marine input was still present as evidenced by the three outliers from the freshwater DOC field (Fig. 10B). Further supporting this, the samples of Unit 4 cluster within the overlapping brackish, freshwater aquatic and terrestrial fields of figure 10B supporting the interpretation of brackish environment of deposition with reduced marine input compared to Unit 3.

A clear trend is recorded showing a transition from the marine environment of Unit 1 through to a terrestrial plant dominated freshwater setting for Unit 2. Subsequently, marine conditions return recorded by the deposition of Unit 3 before a gradual reduction in marine conditions with the gradual increase in freshwater deposition of Unit 4. A clear decrease in $\delta^{13}C$ is recorded across units 1, 3 and 4 with this continued reduction in $\delta^{13}C$ clearly indicating increasing terrestrial plant and freshwater derived and organic material as a result of perturbations in relative sea level (RSL). The correlation between the isotopic data and the foraminiferal assemblage supports the interpretation of changes in the level of marine inundation of the basin. The relative inundation of marine water is a major factor controlling the source of organic material, and therefore the $\delta^{13}C$ and C/N values measured through the core presented here.

## 8.4 Sulphur

Previous research has shown the utility and merit of sulphur in palaeoenvironmental reconstruction (e.g., Berner, 1984; Lim et al., 2015; Lee et al., 2021). Sulphur content and C/S ratios are the focus of many of these studies as these proxies have the ability to distinguish between marine and freshwater environments. This ability to distinguish environment is derived from the sensitivity of C/S ratios to palaeosalinity this sensitivity is a result of sedimentary pyrite formation which forms more readily in marine sediments. Therefore, the C/S ratios of sediments reflect their depositional environment with marine sediments being characterised by low C/S ratios (0.5–5) and freshwater sediments possessing high ratios (≥10) (Berner, 1984). Further brackish fields with C/S ratios of 4 to 11 and 11 to 17 have been defined as brackish water that is more affected by marine and freshwater respectively (Lim et al., 2015). In addition to the use of C/S ratios in palaeoenvironmental reconstruction, the total sulphur abundance also has the ability to distinguish between sediments deposited under marine and freshwater conditions as marine conditions yield sulphur abundances of between 0.3 and 3% (Lim et al., 2019). The low C/S ratio of < 1 in Unit 1 coupled with a low total sulphur content (an average of 1.31 wt%) indicates a reductive marine environment of deposition with samples from Unit 1 forming a well-defined group within the marine field in C vs S space (Fig. 12).

Increases in TOC and C/S ratios indicate a shift to a more freshwater dominated environment for Unit 2 however the increase in wt% S that marks the transition to Unit 2 means the samples from Unit 2 do not lie within the freshwater field defined in Figure 12. One explanation for this is that stratification of the water within the basin occurred once the basin became isolated with denser saline water becoming isolated from the less dense and less brackish waters above this led to anoxic conditions due to the prevention of mixing within the basin (Balascio et al., 2011). An increase in the abundance of sulphur recorded here indicates such stratification as the

reduction of sulphur requires anoxic conditions. Further study incorporating $\delta^{34}S$ of pyrite and organic sulphur aims to further elucidate this sulphur anomaly in order to further understand conditions within the basin at this time.

Unit 3 is characterised by a relatively low sulphur content of <3 wt% S and low C/S ratios between 3 and 5 suggesting a marine environment of deposition for this unit. Between 90 and 60 cm an increase in C/S ratio is recorded with samples entering the brackish field towards the upper transition of Unit 3. This suggests a decrease in marine influence into the basin at this time as a result of RSL fall an interpretation supported by the foraminiferal data.

The relatively high C/S ratios of Unit 4 plot within the brackish field which agrees with the biostratigraphic reconstruction, however the high wt% C of the unit (23 - 26%) means that the C/S method of distinguishing freshwater from marine environments is less reliable. For samples high in carbon, the availability of iron becomes the limiting factor on pyrite formation rather than the abundance of organic matter therefore high C/S ratios can be recorded during marine deposition. As a result, using C/S ratios as a proxy for palaeosalinity is less suitable for sediments with an organic carbon content of >15% (Berner, 1984).

## 8.5 Osmium ($^{187}Os/^{188}Os$)

The osmium (Os) isotope composition ($^{187}Os/^{188}Os$) of sedimentary units have been shown to be a powerful mechanism to establish the $^{187}Os/^{188}Os$ of the water column during deposition (e.g., Ravizza & Turekian, 1989; Cohen et al., 1999; Kuroda et al., 2016; Paquay & Ravizza, 2012; Du Vivier et al., 2014, 2015). The $^{187}Os/^{188}Os$ of seawater at the time of sediment deposition is interpreted to reflect an input balance between two sources: (1) the weathering of upper continental crust via riverine input yielding radiogenic Os ($^{187}Os/^{188}Os$ ~1.4), (2) the input of mantle-derived Os from submarine volcanism, cosmic dust and hydrothermal fluids yielding unradiogenic Os ($^{187}Os/^{188}Os$ ~0.12) (Peucker-Ehrenbrink & Ravizza, 2000). The input balance of these two sources combined with the short residence time of osmium allows temporally short fluctuations to be identified such as glacial-interglacial cycles making it a unique and powerful tracer for palaeoceanographic changes (Rooney et al., 2016; Peucker-Ehrenbrink and Ravizza, 2000). Typically, seawater has a distinct osmium-isotope composition compared to that of fresh river water, with present-day seawater having a $^{187}Os/^{188}Os$ value of ~1.06 (Sharma et al., 1997; Levasseur, 1998; Burton et al., 1999; Peucker-Ehrenbrink & Ravizza, 2000; Cohen, 2004; Rooney et al., 2016).

A lack of marine influence within freshwater systems means the input of unradiogenic sources of osmium such as submarine volcanism and hydrothermal fluids is nil. As a result, freshwater systems yield their osmium isotopic signature from the weathering of the surrounding geology yielding typically radiogenic osmium. The impact of local superficial and bedrock geology is important as preferential weathering of very radiogenic sediments such as organic-rich sediments tend to bias the isotopic composition of runoff towards more radiogenic values (Peucker-Ehrenbrink & Ravizza, 2000). This point is illustrated in a study of riverine osmium signatures and the geology of their associated drainage basins with rivers such as the Xijing

and ChangJiang which drain sedimentary and igneous lithologies yielding osmium signatures of 2.3 and 1.9 (Peucker-Ehrenbrink & Ravizza, 2000).

The lower transition of Unit 1 in this study yields a marine osmium signature of 1.059 supporting the interpretation of a marine depositional setting. The trend towards slightly more radiogenic values up section eventually culminating in the highly radiogenic values (up to 4.887) which characterise Unit 2 has two possible explanations. Firstly, an increased input of weathered material could cause the peak in radiogenic osmium because as discussed above weathered material provides the radiogenic source of osmium. Secondly, isolation of the basin as a result of relative sea-level fall restricted connection to the open ocean and allowed the radiogenic signal to dominate. Previous research from this site (Hamilton et al., 2015) alongside the additional proxy evidence presented here, most significantly the foraminiferal data, identify a shift from marine conditions during the deposition of Unit 1 to freshwater conditions throughout Unit 2 produced by a fall in relative sea level. Such a fall in sea level would cause isolation of the basin from marine inundation and marine sources of osmium leading to a relative increase in osmium sources from terrestrial runoff with a more radiogenic signal. This interpretation is also supported by a study in which a similar increase towards radiogenic osmium values within a shallow epeiric setting of the Late Cretaceous Western Interior Seaway was attributed to restriction from the ocean due to a relative fall in sea level (Du Vivier et al., 2014; Jones et al., 2020).

The highly radiogenic signature of Unit 2 here is of note as the values are more radiogenic than known for non-marine/lacustrine systems such as the Eocene Green River Formation (1.3 to 1.5; Cumming et al., 2012) and the Aptian Ipubi Formation black shale (1.8 to 2.0; Lúcio et al., 2020). Therefore, their highly radiogenic signature is interpreted to be a result of radiogenic osmium derived from weathering of old continental crust. In particular, the preferential weathering of minerals such as biotite in felsic systems is interpreted to contribute to highly

radiogenic values (Peucker-Ehrenbrink & Blum, 1998). Such minerals are present within the Lewisian gneiss which is known to form the bedrock surrounding Loch Duart Marsh (Figure 5) and can yield highly radiogenic values (Burton et al., 2000). Consequently, weathering of the knowingly radiogenic Lewisian Gneiss which surrounds Loch Duart Marsh, and the potential preferential weathering of biotite likely yields the highly radiogenic osmium composition of Unit 2.

Following the peak in radiogenic osmium, values decrease as the upper transition of Unit 2 is approached, with $^{187}Os/^{188}Os$ reaching near marine osmium isotopic values. This suggests a return to a marine environment of deposition due to a RSL rise ending the period of isolation within the basin and restoring the marine connection. The osmium isotopic signature of Units 3 and 4 varies little up the core with values remaining consistently close to the osmium signature of marine water implying continued marine inundation. At the upper transition of Unit 4, the increase from 0.983 (39 - 40cm) to 1.095 (10 - 11 cm) could suggest a decrease in marine influence as it is the most radiogenic value recorded since the termination of basin isolation possibly suggesting another reduction in sea level at this time but not to the same extent as recorded by Unit 2 given the value is only moderately more radiogenic than the normal marine osmium signature. Although the shift to a more radiogenic value is not significant enough in magnitude to definitively draw the conclusion of reduced marine input the interpretation does agree with the results of both the previous biostratigraphic and elemental analysis.

The biostratigraphic evidence and the bulk carbon isotope data identify a gradual trend of reducing marine conditions from a strong marine influence throughout the lower section of Unit 3 followed by a gradual reduction in marine conditions up section. The osmium data presented here appears less sensitive to this more subtle shift in marine influence. Once the site enters a marine phase of deposition at the base of Unit 3 the osmium values shift to typical

open ocean signal, however as the site experiences a reducing marine signal, as suggested by other proxies presented here, at the upper transition of Unit 4 the expected change to more radiogenic osmium values is not pronounced suggesting that the system is less sensitive to subtle changes in marine influence.

Despite this, the close agreement between the reconstruction of relative sea-level based on the $^{187}Os/^{188}Os$ data and the interpretations from the biostratigraphic and stable isotope methods ($\delta^{13}C$, C/N and C/S) imply that the $^{187}Os/^{188}Os$ isotope system can be an effective tracer of relative sea-level within isolation basins. With periods of freshwater deposition during basin isolation as a result marine regression recorded by perturbations towards more radiogenic values and periods of marine deposition during connection of the basin to the open ocean recorded by values consistent with the present-day normal marine osmium isotopic signature. Although the system appears less sensitive to brackish phases its ability to distinguish freshwater from marine periods of deposition demonstrates the effectiveness of osmium as a tracer for sea level and its potential use at sites with poor preservation of microfossils.

## 8.6 XRF data implications on depositional setting

A total of 51 elements were scanned, here seven of these elements (Cu, Al, Si, Ti, Fe, K and Se) are discussed because they showed significant changes across the core. Across Unit 1 peaks in Al, Si, Ti, Fe and K are recorded and reach the highest values far above the mean for each element (Fig. 12). This is interpreted to be due to the high clay content of Unit 1 as clays are phyllosilicates comprised primarily of silica, aluminium and water, often with significant amounts of iron and alkalies (Grim, 1968).

The peaks recorded in both selenium (Se) and Copper (Cu) are of interest as they are not common constituents of the sediment and peaks are only seen in Unit 2 despite Unit 3 having a similar lithological composition therefore both Se and Cu are discussed in depth in the following sections.

**Copper**

The broad peak in copper (Cu) recorded across Unit 2 is of interest as values across this unit are significantly higher than the rest of the core reaching a peak of 100 cps within Unit 2 compared to a mean value of ~30 cps throughout Units 1, 3 and 4 (Fig. 12). Copper is primarily delivered to sediments in association with OM (organometallic complexes) (Tribovillard et al., 2006). Cu is released through the decomposition of such organometallic complexes and can coprecipitate with pyrite under reducing conditions (Moore, 1988; Huerta-Diaz & Morse, 1990). This is as under reducing conditions, Cu (II) is reduced to Cu (I) and may be incorporated in pyrite, and accumulate (Tribovillard et al., 2006). Reduced Cu can also form sulphide phases including CuS and $CuS_2$ (Luther et al., 1980). Therefore, a high abundance of Cu indicates both an abundance of OM delivered Cu to the sediments and that reducing conditions occurred allowing the fixation of Cu (Tribovillard et al., 2006). The interpretation of reducing conditions during the deposition of Unit 2 agrees with the isolation basin setting of Loch Duart Marsh and the interpretation of sea level at this time. A reduction in relative sea-level restricting the basin from marine influence would result in salinity stratification and anoxic conditions allowing such reducing conditions.

**Selenium**

Throughout Unit 2 a clear peak in selenium (Se) is observed. This peak occurs between 165 and 195 cm with values reaching up to 14 cps with a mean of around 9 cps at the peak's maximum (Fig. 12). High organic matter and selenium have been extensively studied and the literature agrees that high organic matter content correlates to increased selenium concentrations (Zhang & Moore, 1997; Tolu et al., 2014). For example, the high organic matter content of the soils in some regions of Northeast China has led to selenium deficiency in its inhabitants due to the immobilisation of selenium and hence reduced bioavailability (Wang & Gao, 2001). Further to this, redox conditions are a key influence on Se concentration as this determines the Se species present in a given environment (Eich-Greatorex et al., 2007). Selenate ($SeO_4^{2-}$) which is soluble, and mobile is the dominant species when oxidising conditions are present whilst selenite ($SeO_3^{2-}$) which adsorbs more strongly onto soil organic matter (Lévesque, 1974) is more dominant when reducing conditions are met (Wen et al., 2014).

Therefore, the high Se content of Unit 2 is interpreted to be due to an abundance of organic matter as evidenced by the high wt% C of this unit in combination with reducing conditions leading to the strong complexation of Se, likely in the form of selenite, with the abundant organic matter and fixation within the sediment. This agrees with the interpretation based on sulphur and copper data of a period of anoxia during the deposition of Unit 2 due to stratification within the basin as a result of RSL fall and basin isolation.

## 9. Late Glacial to Holocene RSL change

The results and interpretations presented match closely with those of Hamilton et al. (2015) with isolation contacts identified within the biostratigraphy, lithostratigraphy, isotopic and elemental analysis. The interpretations based on the foraminifera, $\delta^{13}C$, C/N, S, Os and XRF data all agree and are utilised to reconstruct RSL during the Late Glacial and through the Holocene.

### Late Glacial RSL fall

The clay-rich nature of Unit 1 and the biostratigraphic and elemental data presented suggest a marine environment of deposition during the Late Glacial due to a period of connection between the basin and the open sea after the local deglaciation in the region. This interpretation agrees with model predictions of high RSL during the deposition of Unit 1 (Fig. 17). The isolation contact at Loch Duart Marsh, identified through foraminifera fauna (this study) and diatom flora (Hamilton et al., 2015), records a sharp decline in marine influence and transition to freshwater conditions. This is recorded at 194 cm within LDM-20-JT which correlates to 200 cm within the Hamilton et al. (2015) core which is dated at 14610 to 15240 cal yr BP. This age is in agreement with the age-depth model of this study (Fig. 16) yielding a Late Glacial age for basin isolation. The transition to radiogenic osmium values, combined with high $\delta^{13}C$ and C/N supports a transition to an isolated freshwater setting allowing the deposition of freshwater sediments of Late Glacial age. This period of basin isolation is interpreted to be due to a fall in RSL at this time with an index point recording falling sea level with a RSL value of 0.15 +/- 0.59 below present at 14610 to 15240 cal yr BP (Hamilton et al., 2015). This interpretation agrees with model predictions of low RSL during the deposition of Unit 2 (Fig. 17). This Late Glacial fall in RSL is interpreted to be a result of glacio-isostatic rebound

following deglaciation causing RSL to fall relative to the basin's sill isolating the basin from the open sea (Peltier, 2002; Ballantyne & Gordon, 2021).

**RSL rise and the Mid Holocene highstand**

Following the Late Glacial to Early-Holocene period of isolation and resultant freshwater sedimentation, a subsequent transition to marine sedimentation is inferred through biostratigraphy with the sudden appearance of abundant foraminifera at the base of Unit 3 (Fig. 10). Initially, the fauna is dominated by calcareous species indicating normal marine conditions along with brackish lagoon species, while previous research identifies the influx of polyhalobous (marine) diatoms (Hamilton et al., 2015). This interpretation is further supported by a shift to less radiogenic osmium values with values approaching that of present-day normal seawater in addition to relative low C/N ratios and high $\delta^{13}C$ indicating an increased influence of marine organic material and a decrease in freshwater derived material. Similarly low wt% sulphur and relatively low C/S ratios also support a transition to marine deposition as discussed. Radiocarbon bulk sediment dates at 158 and 162 cm of 10409 to 10235 and 10597 to 10486 cal yr BP, respectively constrain this marine ingression to the early Holocene.

A sea-level index point dated at 9888 to 10183 yr cal BP from Loch Duart Marsh documents RSL rise at the transition from the organic silt to blue-grey silty clay (Hamilton et al., 2015) – the transition from Unit 2 to Unit 3 in this study which is concurrent with model predictions of Bradley et al. (2011) and Kuchar et al. (2012) (Fig. 17). This combined data supports the interpretation of RSL rise at this time just prior to the mid-Holocene highstand a period in which eustatic sea-level rise due to the melting of mid-latitude ice sheets outpaced glacio-isostatic uplift resulting in rising RSL (Lloyd, 2000; Ballantyne & Gordon, 2021).

**Holocene RSL fall**

The upper section of Unit 3 and the transition into Unit 4 illustrates a reducing marine influence recorded within the biostratigraphy with decreasing numbers of fully marine foraminifera coupled with the appearance and dominance of brackish lagoonal and saltmarsh species that tolerate lower salinities observed up section and a similar trend seen within diatoms towards freshwater/low salinity species (Hamilton et al., 2015). The isotopic and elemental analysis discussed further supports this interpretation with relatively high C/N ratios and low $\delta^{13}C$ values recorded within the upper section of Unit 3 and within Unit 4 suggesting a decrease in the input of marine organic matter and the increase in freshwater carbon inputs. The interpretation of RSL fall agrees with the Bradley et al. (2011) and Kuchar et al. (2012) model predictions which show RSL fall throughout the upper section of Unit 3 and into Unit 4 (Fig. 17). This gradual reduction in marine influence from the mid-Holocene highstand reflects a change from relative sea-level rise to relative sea-level fall and is a consequence of the rate of glacio-isostatic uplift becoming greater than the rate of eustatic sea-level rise due to the melting of global ice masses (Shennan et al., 1999; Lloyd, 2000).

The multiproxy data presented here indicates continued connection of the site to the sea throughout the Holocene as supported by the nature of the modern environment as the site is flooded at high tides and is fringed by saltmarsh vegetation. This is supported by Unit 4 forming a defined field within and above freshwater DOC suggesting the environment is not completely freshwater. Additionally, the osmium signature of the upper section of the core remains close to that of present-day seawater, hence does not support a return to fully freshwater conditions. The site today is at the transition from a lagoon to a saltmarsh suggesting the lagoon has been infilled by sedimentation and the site has transitioned to a saltmarsh environment.

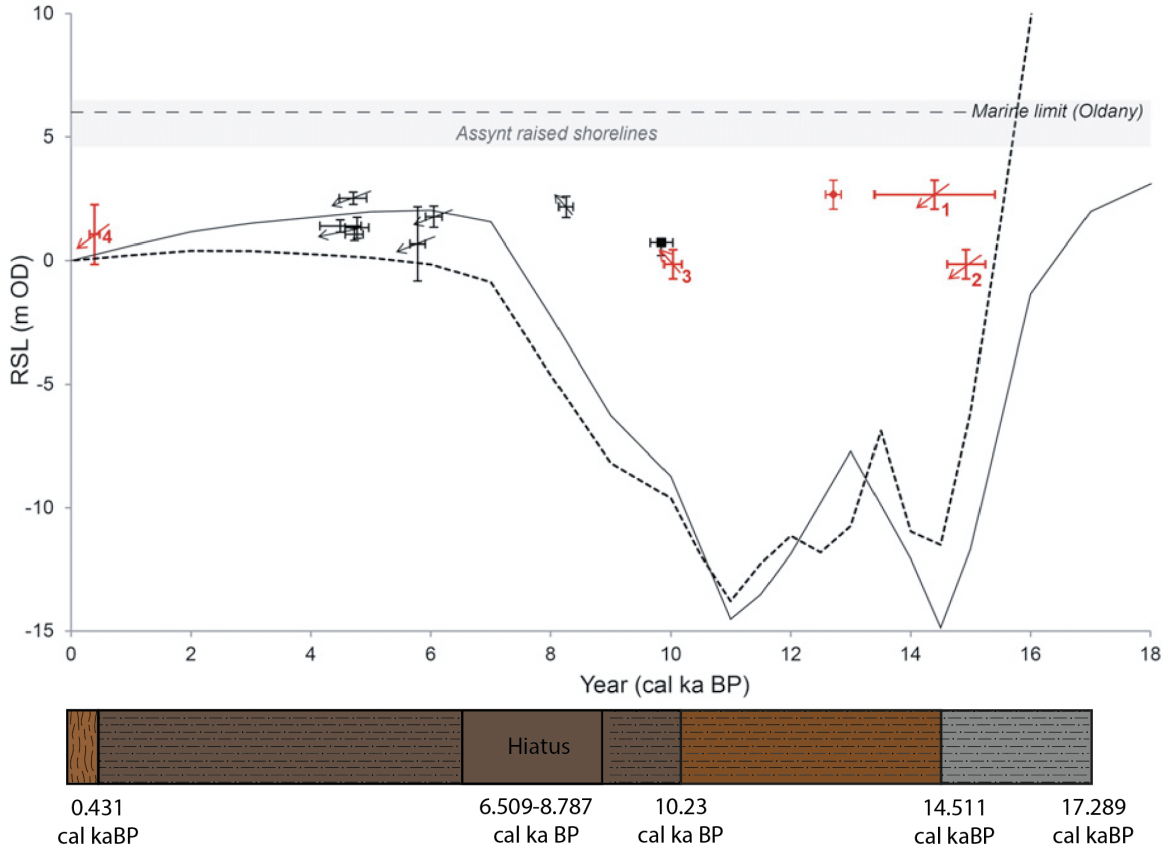


**Figure 17:** RSL curves from Kuchar et al. (2012) (dashed black line) and Bradley et al. (2011) (solid black line) model predictions for Assynt, sea-level index points from Coigach (Shennan et al., 2000) are denoted in black, and those from Duart in red. An index point based on radiocarbon material is represented by the red diamond and the black solid square denotes a limiting index point. The arrows indicate the positive or negative tendency associated with each sea-level index point. Underneath the graph, the stratigraphic units of Loch Duart Marsh are presented with the dates of the transitions between units annotated the dates are estimated from the age-depth model for this study (Fig. 16). RSL figure from Hamilton et al. (2015).

## Conclusions

The aims of this research were to use a multidisciplinary approach encompassing biostratigraphic, isotopic and elemental methods to produce a paleoenvironment history for the Loch Duart Marsh field site and local area and to investigate the potential of additional proxies for palaeoenvironmental and sea-level reconstruction. An isolation basin was chosen for this study due to its usefulness for relative sea-level reconstruction. The paleoenvironment record reconstructed from the LDM-20-JT core has allowed the reconstruction of RSL at this site over the last 15,000 years. This research builds on previous research in the area focused on diatoms to reconstruct the paleoenvironment, the results of this study both agree with and develop this palaeo-reconstruction. Here, a more detailed age-depth model has been developed to further constrain environmental changes and the rate of sedimentation through the core allowing the identification of an erosional surface possibly the result of a storm event.

Secondly, through the combined efforts of biostratigraphy, $\delta^{13}C$, C/N, C/S and XRF a record of RSL has been reconstructed and based on this wide range of proxies this study has tested the validity of additional methods to reconstruct RSL from isolation basins. The results from $\delta^{13}C$ and C/N analysis here broadly agree with previous studies applying these proxies to isolation basins. The application of C/S to an isolation basin here highlights the suitability of this proxy in distinguishing marine from freshwater sedimentation. Arguably most notably the osmium isotopes analysis presented displays its suitability as a technique to reconstruct relative sea-level through the identification of basin isolation and connection to the sea.

During the Late Glacial RSL was such that the basin was connected to the open sea allowing marine deposition as evidenced by the high $\delta^{13}C$ and low C/N and C/S ratios. However, RSL fell during the Late Glacial as a result of glacial isostatic rebound causing a fall in RSL recorded

through the absence of marine foraminifera, high C/N and peaks in sulphur, copper and selenium suggesting a period of anoxia within the basin due to reduced marine input as a result of basin isolation. RSL then increased again due to the melting of mid-latitude ice masses outpacing the rate of isostatic rebound leading once again to connection between the basin and the open sea. This is evidenced by the abundance of marine foraminifera, low $\delta^{13}C$, C/N and C/S within the unit dated to the Early-Late Holocene. RSL is interpreted to have subsequently fallen as reducing marine conditions up section are evidenced by a reduction in the abundance of marine foraminifera, increased C/N and decreased $\delta^{13}C$ suggesting an increase in freshwater inputs. A saltmarsh setting is interpreted for the upper section of the Loch Duart Marsh core which correlates to the Late-Holocene with a more limited marine influence than previously. This fall in sea level is due to isostatic rebound outpacing eustatic sea-level rise causing RSL fall across the Late-Holocene to the present day.

The foraminifera data presented here agree with the biostratigraphic interpretations based on diatoms from Hamilton et al. (2015), this biostratigraphic framework combined with the well-established use of $\delta^{13}C$, C/N and C/S as a proxy for RSL provides a means to test more novel proxies against. The novel method of RSL reconstruction using osmium as an isotopic tracer was employed here to assess its suitability for determining past RSL. By comparison with both the biostratigraphic and relatively robust proxies for RSL change of $\delta^{13}C$ and C/N and sulphur, the ability of osmium as a tracer of RSL has been demonstrated with periods of connection between the basin and the sea recorded by osmium values similar to that of modern seawater and a period of isolation from the basin characterised by distinctly more radiogenic osmium values reflecting a decreased input of unradiogenic sources due to a reduced marine influence.

In summary, the findings of this study concur with and develop an existing paleoenvironmental history of the area elucidating RSL changes from the Late Glacial to the Late-Holocene. Furthermore, the suitability of osmium as an isotopic tracer of RSL has been demonstrated, a method that could be vital in understanding past relative sea-level in areas devoid of microfossil preservation and therefore yields the possibility of expanding our knowledge of RSL changes to previously unstudied sites.

## References


Andrews, J. E., Samways, G., Dennis, P. F., & Maher, B. A. (2000). Origin, abundance and storage of organic carbon and sulphur in the Holocene Humber Estuary: Emphasizing human impact on storage changes. *Geological Society Special Publication*, *166*, 145–170. https://doi.org/10.1144/GSL.SP.2000.166.01.09

Balascio, N. L., Zhang, Z., Bradley, R. S., Perren, B., Dahl, S. O., & Bakke, J. (2011). A multi-proxy approach to assessing isolation basin stratigraphy from the Lofoten Islands, Norway. *Quaternary Research*, *75*(1), 288–300. https://doi.org/10.1016/j.yqres.2010.08.012

Ballantyne, C. K. (2007). Glacial landforms, ice sheets | Trimlines and Palaeonunataks. *Encyclopedia of Quaternary Science*, 892–903. https://doi.org/10.1016/B0-44-452747-8/00100-9

Ballantyne, C.K. (2010). Extent and deglacial chronology of the last British–Irish Ice Sheet: implications of exposure dating using cosmogenic isotopes. *Journal of Quaternary Science: Published for the Quaternary Research Association*, *25*(4), 515-534. https://doi.org/10.1002/jqs.1310

Ballantyne, C. K., and Gordon, J. (2021). *Landscapes and Landforms of Scotland*. 1st ed. Cham: Springer, p.244.

Bamber, J. L., Oppenheimer, M., Kopp, R. E., Aspinall, W. P., & Cooke, R. M. (2019). Ice sheet contributions to future sea-level rise from structured expert judgment. *Proceedings of the National Academy of Sciences of the United States of America*, *166*(23), 11195–11200. https://doi.org/10.1073/pnas.1817205116

Benn, D.I. (1992). The genesis and significance of 'hummocky moraine': evidence from the Isle of Skye, Scotland. *Quaternary Science Reviews*, *11*(7-8), 781-799. https://doi.org/10.1016/0277-3791(92)90083-K

Berner, R. A., & Raiswell, R. (1984). C/S method for distinguishing freshwater from marine sedimentary rocks. *Geology*, *12*(6), 365–368. https://doi.org/10.1130/0091-7613(1984)12<365:CMFDFF>2.0.CO;2

Bickerdike, H. L., Evans, D. J. A., Stokes, C. R. and Ó Cofaigh, C. (2018a). The glacial geomorphology of the Loch Lomond (Younger Dryas) Stadial in Britain: a review. *Journal of Quaternary Science*, *33*(1), 1-54. https://doi.org/10.1002/jqs.3010

Bickerdike, H. L., Ó Cofaigh, C., Evans, D. J. A., & Stokes, C. R. (2018b). Glacial landsystems, retreat dynamics and controls on Loch Lomond Stadial (Younger Dryas) glaciation in Britain. *Boreas*, *47*(1), 202–224. https://doi.org/10.1111/bor.12259

Blaauw, M., & Christeny, J. A. (2011). Flexible paleoclimate age-depth models using an autoregressive gamma process. *Bayesian Analysis*, *6*(3), 457–474. https://doi.org/10.1214/11-BA618

Boulton, G.S.. Peacock, J. D. and Sutherland, D.G. (1991). Quaternary. In Craig, G.Y. (ed.) The Geology of Scotland. Geological Society Special Publication, London, 503-544.

Bowen, D. Q., Rose, J., McCabe, A. M., & Sutherland, D. G. (1986). Correlation of quaternary glaciations in England, Ireland, Scotland and Wales. *Quaternary Science Reviews*, *5*(C), 299–340. https://doi.org/10.1016/0277-3791(86)90194-0

Bradley, S.L., Milne, G.A., Shennan, I. and Edwards, R. (2011). An improved glacial isostatic adjustment model for the British Isles. *Journal of Quaternary Science*, *26*(5), 541- 552. https://doi.org/10.1002/jqs.1481

Bradwell, T., Fabel, D., Stoker, M., Mathers, H., McHargue, L., and Howe, J. (2008). Ice caps existed throughout the Lateglacial Interstadial in northern Scotland. *Journal of Quaternary Science, 23*(5), 401–407. https://doi.org/10.1002/jqs.1181

Bradwell, T., Small, D., Fabel, D., Clark, C. D., Chiverrell, R. C., Saher, M. H., Dove, D., Callard, S. L., Burke, M. J., Moreton, S. G., Medialdea, A., Bateman, M. D., Roberts, D. H., Golledge, N. R., Finlayson, A., Morgan, S., & Cofaigh, C. (2021). Pattern, style and timing of British–Irish Ice Sheet retreat: Shetland and northern North Sea sector. *Journal of Quaternary Science*, *36*(5), 681–722. https://doi.org/10.1002/jqs.3163

Bronk Ramsey, C. (2009). Bayesian analysis of radiocarbon dates. *Radiocarbon, 51*(1), 337–360.

Burton, K. W., Bourdon, B., Birck, J. L., Allègre, C. J., & Hein, J. R. (1999). Osmium isotope variations in the oceans recorded by Fe-Mn crusts. *Earth and Planetary Science Letters*, *171*(1), 185–197. https://doi.org/10.1016/S0012-821X(99)00139-9

Burton, K. W., Capmas, F., Birck, J. L., Allègre, C. J., & Cohen, A. S. (2000). Resolving crystallisation ages of Archean mafic-ultramafic rocks using the Re-Os isotope system. *Earth and Planetary Science Letters*, *179*(3–4), 453–467. https://doi.org/10.1016/S0012-821X(00)00134-5

Chappuis, E., Seriñá, V., Martí, E., Ballesteros, E., & Gacia, E. (2017). Decrypting stable isotope ($\delta^{13}C$ and $\delta^{15}N$) variability in aquatic plants. *Freshwater Biology*, *62*(11), 1807– 1818. https://doi.org/10.1111/fwb.12996

Clark, P. U., Dyke, A. S., Shakun, J. D., Carlson, A. E., Clark, J., Wohlfarth, B., Mitrovica, J. X., Hostetler, S. W., & McCabe, A. M. (2009). The Last Glacial Maximum. *Science*, *325*(5941), 710–714. https://doi.org/10.1126/science.1172873

Clark, C. D., Hughes, A. L. C., Greenwood, S. L., Jordan, C., & Sejrup, H. P. (2012). Pattern and timing of retreat of the last British-Irish Ice Sheet. *Quaternary Science Reviews*, *44*, 112–146. https://doi.org/10.1016/j.quascirev.2010.07.019

Clark, C. D., Ely, J. C., Greenwood, S. L., Hughes, A. L. C., Meehan, R., Barr, I. D., Bateman, M. D., Bradwell, T., Doole, J., Evans, D. J. A., Jordan, C. J., Monteys, X., Pellicer, X. M., & Sheehy, M. (2018). BRITICE Glacial Map, version 2: a map and GIS database of glacial landforms of the last British–Irish Ice Sheet. *Boreas*, *47*(1), 11-e8. https://doi.org/10.1111/bor.12273

Clark, C. D., & Fabel, D. (2019). Early deglaciation of the British-Irish Ice Sheet on the Atlantic shelf northwest of Ireland driven by glacioisostatic depression and high relative sea

level. *Quaternary Science Reviews*, *208*, 76–96. https://doi.org/10.1016/j.quascirev.2018.12.022

Cohen, A. S., Coe, A. L., Bartlett, J. M., & Hawkesworth, C. J. (1999). Precise Re-Os ages of organic-rich mudrocks and the Os isotope composition of Jurassic seawater. *Earth and Planetary Science Letters*, *167*(3–4), 159–173. https://doi.org/10.1016/S0012-821X(99)00026-6

Cohen, A. S. (2004). The rhenium-osmium isotope system: Applications to geochronological and palaeoenvironmental problems. *Journal of the Geological Society*, *161*(4), 729–734. https://doi.org/10.1144/0016-764903-084

Cumming, V. M., Selby, D., & Lillis, P. G. (2012). Re-Os geochronology of the lacustrine Green River Formation: Insights into direct depositional dating of lacustrine successions, Re-Os systematics and paleocontinental weathering. *Earth and Planetary Science Letters*, *359–360*, 194–205. https://doi.org/10.1016/j.epsl.2012.10.012

Davies, H. C., Dobson, M. R., & Whittington, R. J. (1984). A revised seismic stratigraphy for Quaternary deposits on the inner continental shelf west of Scotland between 55°30‘N and 57°30’N. *Boreas*, *13*(1), 49–66. https://doi.org/10.1111/j.1502-3885.1984.tb00059.x

Du Vivier, A. D. C., Selby, D., Sageman, B. B., Jarvis, I., Gröcke, D. R., & Voigt, S. (2014). Marine $^{187}Os/^{188}Os$ isotope stratigraphy reveals the interaction of volcanism and ocean circulation during Oceanic Anoxic Event 2. *Earth and Planetary Science Letters*, *389*, 23–33. https://doi.org/10.1016/j.epsl.2013.12.024

Du Vivier, A. D. C., Selby, D., Condon, D. J., Takashima, R., & Nishi, H. (2015). Pacific $^{187}Os/^{188}Os$ isotope chemistry and U-Pb geochronology: Synchroneity of global Os isotope change across OAE 2. *Earth and Planetary Science Letters*, *428*, 204–216. https://doi.org/10.1016/j.epsl.2015.07.020

Edwards, R. J. (2013). Sedimentary Indicators of Relative Sea-Level Changes - Low Energy. *Encyclopedia of Quaternary Science: Second Edition*, *December*, 396–408. https://doi.org/10.1016/B978-0-444-53643-3.00136-9

Eich-Greatorex, S., Sogn, T. A., Øgaard, A. F., & Aasen, I. (2007). Plant availability of inorganic and organic selenium fertiliser as influenced by soil organic matter content and pH. *Nutrient Cycling in Agroecosystems*, *79*(3), 221–231. https://doi.org/10.1007/s10705-007-9109-3

Emeis, K. C., Struck, U., Blanz, T., Kohly, A., & Voß, M. (2003). Salinity changes in the central Baltic Sea (NW Europe) over the last 10 000 years. *Holocene*, *13*(3), 411–421. https://doi.org/10.1191/0959683603hl634rp

Finlayson, A. and Bradwell, T. 2007. Evidence for Loch Lomond Stadial ice cap glaciation of the Beinn Dearg massif, northern Scotland. *Quaternary newsletter*, *113*, pp.10-17. http://nora.nerc.ac.uk/3462/1/QUATERNARY_NEWSLETTER_ARTICLE.pdf

Flemming, N. C. (1982). Multiple regression analysis of earth movements and eustatic sea-level change in the United Kingdom in the past 9000 years. *Proceedings of the Geologists' Association*, *93*(1), 113–125. https://doi.org/10.1016/S0016-7878(82)80035-7

Geikie, J. (1894). The Great Ice Age and its relation to the antiquity of Man. Edward Stanford, London.

Golledge, N. R. (2010). Glaciation of Scotland during the Younger Dryas stadial: A review. *Journal of Quaternary Science*, *25*(4), 550–566. https://doi.org/10.1002/jqs.1319 Golledge, N. R., Hubbard, A., & Sugden, D. E. (2008). High-resolution numerical simulation of Younger Dryas glaciation in Scotland. *Quaternary Science Reviews*, *27*(9–10), 888–904. https://doi.org/10.1016/j.quascirev.2008.01.019

Greenwood, S. L., & Clark, C. D. (2009). Reconstructing the last Irish Ice Sheet 2: a geomorphologically-driven model of ice sheet growth, retreat and dynamics. *Quaternary Science Reviews*, *28*(27–28), 3101–3123. https://doi.org/10.1016/j.quascirev.2009.09.014

Grim, R. (1968). *Clay mineralogy*. 2nd ed. New York: McGraw-Hill.

Haflidason, H., King, E.L., Kristensen, D.K., Helland, E., Duffy, M., Scourse, J.D., Austin, W.E.N., Sejrup, H.P. (1997). Marine Geological/geophysical Cruise Report on the Western Irish Margin: Donegal Bay, Clew Bay, GalwayBay, Irish Shelf and Rockall Trough. University of Bergen, Bergen.

Hamilton, C. A., Lloyd, J. M., Barlow, N. L. M., Innes, J. B., Flecker, R., & Thomas, C. P. (2015). Late Glacial to Holocene relative sea-level change in Assynt, northwest Scotland, UK. *Quaternary Research (United States)*, *84*(2), 214–222. https://doi.org/10.1016/j.yqres.2015.07.001

Hubbard, A. (1999). High-resolution modeling of the advance of the Younger Dryas ice sheet and its climate in Scotland. *Quaternary Research*, *52*(1), 27–43. https://doi.org/10.1006/qres.1999.2055

Huerta-Diaz, M. A., & Morse, J. W. (1990). A quantitative method for determination of trace metal concentrations in sedimentary pyrite. *Marine Chemistry*, *29*(C), 119–144. https://doi.org/10.1016/0304-4203(90)90009-2

Johnstone, G. & Mykura, W. (1989). British Regional Geology: The Northern Highlands of Scotland 4th ed., British Geological Survey

Jones, M.M., Sageman, B.B., Selby, D., Jicha, B.R., Singer, B.S., Titus, A.L. (2021). Regional chronostratigraphic synthesis of the Cenomanian-Turonian OAE2 interval, Western Interior Basin (USA): New Re-Os chemostratigraphy and $^{40}Ar/^{39}Ar$ geochronology. *Geological Society of America, Bulletin, 133 (5-6), p. 1090-1104,* https://doi.org/10.1130/B35594.1

Khan, N. S., Vane, C. H., Engelhart, S. E., Kendrick, C., & Horton, B. P. (2019). The application of $\delta^{13}C$, TOC and C/N geochemistry of mangrove sediments to reconstruct Holocene paleoenvironments and relative sea levels, Puerto Rico. *Marine Geology*, *415*(January), 105963. https://doi.org/10.1016/j.margeo.2019.105963

Kuchar, J., Milne, G., Hubbard, A., Patton, H., Bradley, S., Shennan, I., & Edwards, R. (2012). Evaluation of a numerical model of the British-Irish ice sheet using relative sea-level data: Implications for the interpretation of trimline observations. *Journal of Quaternary Science*, *27*(6), 597–605. https://doi.org/10.1002/jqs.2552

Kopp, R. E., DeConto, R. M., Bader, D. A., Hay, C. C., Horton, R. M., Kulp, S., Oppenheimer, M., Pollard, D., & Strauss, B. H. (2017). Evolving Understanding of Antarctic Ice-Sheet Physics and Ambiguity in Probabilistic Sea-Level Projections. *Earth's Future*, *5*(12), 1217–1233. https://doi.org/10.1002/2017EF000663

Krabbendam, M., & Bradwell, T. (2014). Quaternary evolution of glaciated gneiss terrains: Pre-glacial weathering vs. glacial erosion. *Quaternary Science Reviews*, *95*, 20–42. https://doi.org/10.1016/j.quascirev.2014.03.013

Kulp, S. A., & Strauss, B. H. (2019). New elevation data triple estimates of global vulnerability to sea-level rise and coastal flooding. *Nature Communications*, *10*(1). https://doi.org/10.1038/s41467-019-12808-z

Kuroda, J., Jiménez-Espejo, F. J., Nozaki, T., Gennari, R., Lugli, S., Manzi, V., Roveri, M., Flecker, R., Sierro, F. J., Yoshimura, T., Suzuki, K., & Ohkouchi, N. (2016). Miocene to Pleistocene osmium isotopic records of the Mediterranean sediments. *Paleoceanography*, *31*(1), 148–166. https://doi.org/10.1002/2015PA002853

Lamb, A. L., Wilson, G. P., & Leng, M. J. (2006). A review of coastal palaeoclimate and relative sea-level reconstructions using $\delta^{13}C$ and C/N ratios in organic material. *Earth-Science Reviews*, *75*(1–4), 29–57. https://doi.org/10.1016/j.earscirev.2005.10.003

Lambeck, K. (1993). Glacial rebound of the British Isles—I. Preliminary model results. *Geophysical Journal International*, *115*(3), 941–959. https://doi.org/10.1111/j.1365-246X.1993.tb01503.x

Lambeck, K. (1995). Late Devensian and Holocene shorelines of the British Isles and North Sea from models of glacio-hydro-isostatic rebound. *Journal - Geological Society (London)*, *152*(3), 437–448. https://doi.org/10.1144/gsjgs.152.3.0437

Lambeck, K., Rouby, H., Purcell, A., Sun, Y., & Sambridge, M. (2014). Sea level and global ice volumes from the Last Glacial Maximum to the Holocene. *Proceedings of the National Academy of Sciences of the United States of America*, *111*(43), 15296–15303. https://doi.org/10.1073/pnas.1411762111

Lee, H., Lee, J. Y., & Shin, S. (2021). Middle holocene coastal environmental and climate change on the southern coast of Korea. *Applied Sciences (Switzerland)*, *11*(1), 1–14. https://doi.org/10.3390/app11010230

Leng, M. J., & Lewis, J. P. (2017). C/N ratios and carbon isotope composition of organic matter in estuarine environments. In K. Saunders, K. Weckström, P. Gell, & G. Skilbeck (Eds.), Applications of Paleoenvironmental Techniques in Estuarine Studies Springer Netherlands. doi:10.1007/978-94-024-0990-1_9

Levasseur, S., Birck, J.-L., & Allègre, C. J. (1998). Direct Measurement of Femtomoles of Osmium and the $^{187}Os/^{186}Os$ Ratio in Seawater. *Science*, *282*(5387), 272–274. http://www.jstor.org/stable/2897666

Lévesque, M. (1974). Selenium distribution in Canadian soil profiles. *Canadian Journal of Soil Science*, 54(1), pp.63-68. https://doi.org/10.4141/cjss74-008

Lim, J., Lee, J.Y., Kim, J.C., Hong, S.S. and Yang, D.Y. (2015). Holocene environmental change at the southern coast of Korea based on organic carbon isotope ($\delta^{13}C$) and C/S ratios. *Quaternary International*, *384*, 160-168. https://doi.org/10.1016/j.quaint.2015.05.017

Lim, J., Lee, J. Y., Hong, S. S., Park, S., Lee, E., & Yi, S. (2019). Holocene coastal environmental change and ENSO-driven hydroclimatic variability in East Asia. *Quaternary Science Reviews*, *220*, 75–86. https://doi.org/10.1016/j.quascirev.2019.07.041

Lloyd, J. (2000). Combined foraminiferal and thecamoebian environmental reconstruction from an isolation basin in NW Scotland: Implications for sea-level studies. *Journal of Foraminiferal Research*, *30*(4), 294–305. https://doi.org/10.2113/0300294

Lloyd, J. M., & Evans, J. R. (2002). Contemporary and fossil foraminifera from isolation basins in northwest Scotland. *Journal of Quaternary Science*, *17*(5–6), 431–443. https://doi.org/10.1002/jqs.719

Long, A. J., Woodroffe, S. A., Roberts, D. H., & Dawson, S. (2011). Isolation basins, sea-level changes and the Holocene history of the Greenland Ice Sheet. *Quaternary Science Reviews*, *30*(27–28), 3748–3768. https://doi.org/10.1016/j.quascirev.2011.10.013

Lúcio, T., Souza Neto, J. A., & Selby, D. (2020). Late Barremian / Early Aptian Re-Os age of the Ipubi Formation black shales: Stratigraphic and paleoenvironmental implications for Araripe Basin, northeastern Brazil. *Journal of South American Earth Sciences*, *102*(February). https://doi.org/10.1016/j.jsames.2020.102699

Luther, G. W., Meyerson, A. L., Krajeswki, J. J., & Hires, R. (1980). Metal sulfides in estuarine sediments. *J. Sediment. Petrol.*, *50*(4), 1117–1120. https://doi.org/10.1306/212f7b94-2b24-11d7-8648000102c1865d

Mackie, E. A. V., Leng, M. J., Lloyd, J. M., & Arrowsmith, C. (2005). Bulk organic δ13 C and C/N ratios as palaeosalinity indicators within a Scottish isolation basin. *Journal of Quaternary Science*, *20*(4), 303–312. https://doi.org/10.1002/jqs.919

Meyers, P. A. (1994). Preservation of elemental and isotopic source identification of sedimentary organic matter. *Chemical Geology*, *114*(3–4), 289–302. https://doi.org/10.1016/0009-2541(94)90059-0

Moore, J.A. (1986). Charophytes of Great Britain and Ireland. Botanical Society of the British Isles. ISBN: 9780901158161

Moore, J. N., Ficklin, W. H., & Johns, C. (1988). Partitioning of Arsenic and Metals in Reducing Sulfidic Sediments. *Environmental Science and Technology*, *22*(4), 432–437. https://doi.org/10.1021/es00169a011

Mörner, N. A. (1976). Eustasy and Geoid Changes. *The Journal of Geology,* 84(2), 123-151. https://www.jstor.org/stable/30065695

Mörner, N. A. (1980). Relative sea-level, tectono-eustasy, geoidal-eustasy and geodynamics during the Cretaceous. *Cretaceous Research*, *1*(4), 329–340. https://doi.org/10.1016/0195-6671(80)90042-7

Müller, A., & Mathesius, U. (1999). The palaeoenvironments of coastal lagoons in the southern Baltic Sea, I. The application of sedimentary C(org)/N ratios as source indicators of organic matter. *Palaeogeography, Palaeoclimatology, Palaeoecology*, *145*(1–3), 1–16. https://doi.org/10.1016/S0031-0182(98)00094-7

Murray, J. W. (1971), *An Atlas of British Recent Foraminiferids*: Heinemann, London, 245. Murray J. W., (1979). British Nearshore Foraminiferids. In *Synopses of the British Fauna (new series)*, Kermack DM, Barnes RSK (eds). Academic Press: London; 1–68.

Nygård, A., Sejrup, H. P., Haflidason, H., Cecchi, M., & Ottesen, D. (2004). Deglaciation history of the southwestern Fennoscandian Ice Sheet between 15 and 13 14C ka BP. *Boreas*, *33*(1), 1–17. https://doi.org/10.1080/03009480310006943

Neumann, B., Vafeidis, A. T., Zimmermann, J., & Nicholls, R. J. (2015). Future coastal population growth and exposure to sea-level rise and coastal flooding - A global assessment. *PLoS ONE*, *10*(3). https://doi.org/10.1371/journal.pone.0118571

Ó Cofaigh, C., Telfer, M. W., Bailey, R. M., & Evans, D. J. A. (2012). Late Pleistocene chronostratigraphy and ice sheet limits, southern Ireland. *Quaternary Science Reviews*, *44*, 160–179. https://doi.org/10.1016/j.quascirev.2010.01.011

Ó Cofaigh, C., Weilbach, K., Lloyd, J. M., Benetti, S., Callard, S. L., Purcell, C., Chiverrell, R. C., Dunlop, P., Saher, M., Livingstone, S. J., Van Landeghem, K. J. J., Moreton, S. G., Clark, C. D., & Fabel, D. (2019). Early deglaciation of the British-Irish Ice Sheet on the Atlantic shelf northwest of Ireland driven by glacioisostatic depression and high relative sea level. *Quaternary Science Reviews*, *208*, 76–96. https://doi.org/10.1016/j.quascirev.2018.12.022

Paquay, F. S., & Ravizza, G. (2012). Heterogeneous seawater $^{187}Os/^{188}Os$ during the Late Pleistocene glaciations. *Earth and Planetary Science Letters*, *349–350*, 126–138. https://doi.org/10.1016/j.epsl.2012.06.051

Peltier, W. R., Shennan, I., Drummond, R., & Horton, B. (2002). On the postglacial isostatic adjustment of the British Isles and the shallow viscoelastic structure of the Earth. *Geophysical Journal International*, *148*(3), 443–475. https://doi.org/10.1046/j.1365- 246x.2002.01586.x

Peucker-Ehrenbrink, B., & Blum, J. D. (1998). Re-Os isotope systematics and weathering of Precambrian crustal rocks: Implications for the marine osmium isotope record. *Geochimica et Cosmochimica Acta*, *62*(19–20), 3193–3203. https://doi.org/10.1016/S0016-7037(98)00227-0

Peucker-Ehrenbrink, B., & Ravizza, G. (2000). The marine osmium isotope record. *Terra Nova*, *12*(5), 205–219. https://doi.org/10.1046/j.1365-3121.2000.00295.x

Rasmussen, P., Pantopoulos, G., Jensen, J. B., Olsen, J., Røy, H., & Bennike, O. (2020). Holocene sedimentary and environmental development of Aarhus Bay, Denmark – a multi-proxy study. *Boreas*, *49*(1), 108–128. https://doi.org/10.1111/bor.12408

Ravizza, G., & Turekian, K. K. (1989). Application of the $^{187}$Re-$^{187}$Os system to black shale geochronometry. *Geochimica et Cosmochimica Acta*, *53*(12), 3257–3262. https://doi.org/10.1016/0016-7037(89)90105-1

Reimer, P. J., Bard, E., Bayliss, A., Beck, J. W., Blackwell, P. G., Bronk Ramsey, C., Grootes, P. M., Guilderson, T. P., Haflidason, H., Hajdas, I., Hatt'e, C., Heaton, T. J., Hoffmann, D. L., Hogg, A. G., Hughen, K. A., Kaiser, K. F., Kromer, B., Manning, S. W., Niu, M., Reimer, R. W., Richards, D. A., Scott, E. M., Southon, J. R., Staff, R. A., Turney, C. S. M., & van der Plicht, J. (2013). IntCal13 and Marine13 Radiocarbon Age Calibration Curves 0-50,000 Years cal BP. *Radiocarbon, 55*(4), 1869–1887.

Reimer, P. J., Austin, W. E. N., Bard, E., Bayliss, A., Blackwell, P. G., Bronk Ramsey, C., Butzin, M., Cheng, H., Edwards, R. L., Friedrich, M., Grootes, P. M., Guilderson, T. P., Hajdas, I., Heaton, T. J., Hogg, A. G., Hughen, K. A., Kromer, B., Manning, S. W., Muscheler, R., Palmer, J. G., Pearson, C., van der Plicht, J., Reimer, R. W., Richards, D. A., Scott, E. M., Southon, J. R., Turney, C. S. M., Wacker, L., Adolphi, F., Büntgen, U., Capano, M., Fahrni, S. M., Fogtmann-Schulz, A., Friedrich, R., Köhler, P., Kudsk, S., Miyake, F., Olsen, J., Reinig, F., Sakamoto, M., Sookdeo, A. and Talamo, S. (2020). The IntCal20 Northern Hemisphere Radiocarbon Age Calibration Curve (0-55 cal kBP). *Radiocarbon*, *62*(4), 725–757. https://doi.org/10.1017/RDC.2020.41

Rooney, A. D., Selby, D., Lloyd, J. M., Roberts, D. H., Lückge, A., Sageman, B. B., & Prouty, N. G. (2016). Tracking millennial-scale Holocene glacial advance and retreat using osmium isotopes: Insights from the Greenland ice sheet. *Quaternary Science Reviews*, *138*, 49–61. https://doi.org/10.1016/j.quascirev.2016.02.021

Schimmelmann, A., Albertino, A., Sauer, P. E., Qi, H., Molinie, R., & Mesnard, F. (2009). Nicotine, acetanilide and urea multi-level2H-,$^{13}$C- and$^{15}$N-abundance reference materials for continuous-flow isotope ratio mass spectrometry. *Rapid Communications in Mass Spectrometry*, *23*(22), 3513–3521. https://doi.org/10.1002/rcm.4277

Scott, D. B., & Medioli, F. S. (1980). Quantitative studies of marsh foraminiferal distributions in Nova Scotia: Implications for sea level studies. *Cushman Foundation for Foraminiferal Research Special Publication*, *17*, 58. http://ci.nii.ac.jp/naid/10010788003/en/

Selby, D., & Creaser, R. A. (2003). Re-Os geochronology of organic rich sediments: An evaluation of organic matter analysis methods. *Chemical Geology*, *200*(3–4), 225–240. https://doi.org/10.1016/S0009-2541(03)00199-2

Selby, D., Creaser, R. A., & Fowler, M. G. (2007). Re-Os elemental and isotopic systematics in crude oils. *Geochimica et Cosmochimica Acta*, *71*(2), 378–386. https://doi.org/10.1016/j.gca.2006.09.005

Sejrup, H. P., Hjelstuen, B. O., Dahlgren, K. I. T., Haflidason, H., Kuijpers, A., Nygård, A., Praeg, D., Stoker, M. S., & Vorren, T. O. (2005). Pleistocene glacial history of the NW

European continental margin. *Marine and Petroleum Geology*, *22*(9–10), 1111–1129. https://doi.org/10.1016/j.marpetgeo.2004.09.007

Sharma, M., Papanastassiou, D. A., & Wasserburg, G. J. (1997). The concentration and isotopic composition of osmium in the oceans. *Geochimica et Cosmochimica Acta*, *61*(16), 3287–3299. https://doi.org/10.1016/S0016-7037(97)00210-X

Shennan, I., Tooley, M.J., Davis, M.J. and Haggart, B.A. (1983). Analysis and interpretation of Holocene sea-level data. *Nature*, *302*(5907), pp.404-406. https://doi.org/10.1038/302404a0

Shennan, I., Innes, J. B., Long, A. J. & Zong, Y. (1993). Late Devensian and Holocene relative sea-level changes at Rumach, near Arisaig, northwest Scotland. *Norsk Geologisk Tiddskrift 73* (3), 161-174

Shennan, I., Innes, J. B., Long, A. J., & Zong, Y. (1994). Late Devensian and Holocene relative sea-level changes at Loch nan Eala, near Arisaig, northwest Scotland. *Journal of Quaternary Science*, *9*(3), 261–283. https://doi.org/10.1002/jqs.3390090307

Shennan, I. (1999). Global meltwater discharge and the deglacial sea-level record from northwest Scotland. *Journal of Quaternary Science*, *14*(7), 715–719. https://doi.org/10.1002/(SICI)1099-1417(199912)14:7<715::AID-JQS511>3.0.CO;2-G

Shennan, I., Lambeck, K., Horton, B., Innes, J., Lloyd, J., McArthur, J., Purcell, T. and Rutherford, M. (2000). Late Devensian and Holocene records of relative sea-level changes in northwest Scotland and their implications for glacio-hydro-isostatic modelling. *Quaternary Science Reviews*, *19*(11), 1103-1135. https://doi.org/10.1016/S0277-3791(99)00089-X

Shennan, I., Bradley, S., Milne, G., Brooks, A., Bassett, S. and Hamilton, S. (2006). Relative sea-level changes, glacial isostatic modelling and ice-sheet reconstructions from the British Isles since the Last Glacial Maximum. *Journal of Quaternary Science: Published for the Quaternary Research Association*, *21*(6), 585-599. https://doi.org/10.1002/jqs.1049

Shennan, I., Bradley, S. L., & Edwards, R. (2018). Relative sea-level changes and crustal movements in Britain and Ireland since the Last Glacial Maximum. *Quaternary Science Reviews*, *188*(May), 143–159. https://doi.org/10.1016/j.quascirev.2018.03.031

Sissons, J.B. (1967). The Evolution of Scotland's Scenery, Edinburgh: Oliver and Boyd.

Sissons, J. B. (1974). A Late-Glacial Ice Cap in the Central Grampians, Scotland. *Transactions of the Institute of British Geographers*, *62*(62), 95. https://doi.org/10.2307/621517

Sissons, J. B. (1977). The Loch Lomond Readvance in the northern mainland of Scotland. In *Studies in the Scottish Lateglacial Environment*., Gray, J. M, Lowe, J. J (eds). Pergamon Press: Oxford; 45–59. https://doi.org/10.1016/B978-0-08-020498-7.50009-1

Sissons, J. B. (1979). The Loch Lomond Stadial in the British Isles. *Nature*, *280*(5719), 199–203. https://doi.org/10.1038/280199a0

Sissons, J.B. (1983). Shorelines and isostasy in Scotland. In D. E. Smith & A. G. Dawson, eds. *Shorelines and Isostasy*. Academic Press, London, 209–226

Smith, D. E., Wells, J. M., Mighall, T. M., Cullingford, R. A., Holloway, L. K., Dawson, S. and Brooks, C. L. (2002) Holocene relative sea levels and coastal changes in the lower Cree valley and estuary, SW Scotland, U.K., *Transactions of the Royal Society of Edinburgh: Earth Sciences*. Royal Society of Edinburgh Scotland Foundation, 93(4), 301–331. doi: 10.1017/S0263593300000456.

Smith, D. E., Barlow, N. L. M., Bradley, S. L., Firth, C. R., Hall, A. M., Jordan, J. T., & Long, D. (2019). Quaternary sea level change in Scotland. In *Earth and Environmental Science Transactions of the Royal Society of Edinburgh 110* (1–2), 219–256. https://doi.org/10.1017/S1755691017000469

Sundelin, U. (1917). Fornsjöstudier inom Stångåns och Svartåns vattenområden, med särskild hänsyn till den sen- och postglaciala klimatutvecklingen. Akademisk Avhandling, Uppsala, Matematisk- Naturvetenskapliga Sektion. *Sveriges Geologiska Undersokning Series Ca*. *16*. 291

Szidat, S., Salazar, G. A., Vogel, E., Battaglia, M., Wacker, L., Synal, H.-A., & Türler, A. (2014). 14 C Analysis and Sample Preparation at the New Bern Laboratory for the Analysis of Radiocarbon with AMS (LARA). *Radiocarbon*, *56*(2), 561–566. https://doi.org/10.2458/56.17457

Thornton, S. F., & McManus, J. (1994). Application of organic carbon and nitrogen stable isotope and C/N ratios as source indicators of organic matter provenance in estuarine systems: Evidence from the tay estuary, Scotland. *Estuarine, Coastal and Shelf Science*, *38*(3), 219–233. https://doi.org/10.1006/ecss.1994.1015

Timms, R. G. O., Abrook, A. M., Matthews, I. P., Francis, C. P., Mroczkowska, A., Candy, I., Brooks, S. J., Milner, A. M., & Palmer, A. P. (2021). Evidence for centennial-scale Lateglacial and early Holocene climatic complexity from Quoyloo Meadow, Orkney, Scotland. *Journal of Quaternary Science*, *36*(3), 339–359. https://doi.org/10.1002/jqs.3282

Tolu, J., Thiry, Y., Bueno, M., Jolivet, C., Potin-Gautier, M., & Le Hécho, I. (2014). Distribution and speciation of ambient selenium in contrasted soils, from mineral to organic rich. *Science of the Total Environment*, *479–480*(1), 93–101. https://doi.org/10.1016/j.scitotenv.2014.01.079

Tribovillard, N., Algeo, T. J., Lyons, T., & Riboulleau, A. (2006). Trace metals as paleoredox and paleoproductivity proxies: An update. *Chemical Geology*, *232*(1–2), 12–32. https://doi.org/10.1016/j.chemgeo.2006.02.012

Troels-Smith, J. (1955). Karakterisering af lose jordater (Characterisation of Unconsolidated Sediments). *Geological Survey of Denmark IV*, 3, 1–73.

Wang, Z., & Gao, Y. (2001). Biogeochemical cycling of selenium in Chinese environments. *Applied Geochemistry*, *16*(11–12), 1345–1351. https://doi.org/10.1016/S0883-2927(01)00046-4

Wen, H., Carignan, J., Chu, X., Fan, H., Cloquet, C., Huang, J., Zhang, Y., & Chang, H. (2014). Selenium isotopes trace anoxic and ferruginous seawater conditions in the Early Cambrian. *Chemical Geology*, *390*, 164–172. https://doi.org/10.1016/j.chemgeo.2014.10.022

Wong, T.E., Bakker, A.M.R and Keller, K. (2017). Impacts of Antarctic fast dynamics on sea-level projections and coastal flood defense. *Climatic Change*, *144*(2), pp.347-364. https://doi.org/10.1007/s10584-017-2039-4

Zhang, Y. Q., & Moore, J. N. (1997). Interaction of selenate with a wetland sediment. *Applied Geochemistry*, *12*(5), 685–691. https://doi.org/10.1016/S0883-2927(97)00025-5

Zwartz, D., Bird, M., Stone, J., & Lambeck, K. (1998). Holocene sea-level change and ice-sheet history in the Vestfold Hills, East Antarctica. *Earth and Planetary Science Letters*, *155*(1–2), 131–145. https://doi.org/10.1016/s0012-821x(97)00204-5

**Appendix 1.1:** Raw foraminifera counts for Loch Duart Marsh

| Foraminifera species | | | | | | | | | |
|---|---|---|---|---|---|---|---|---|---|
| **Depth in core (cm)** | Miliammina fusca | Jadammina macrescens | Elphidium williamsoni | Haynesina germanica | Ammonia beccarii | Cibicides lobatulus | Elphidium macellum | Elphidium margaritaceum | Haynesina depressus |
| **9-10** | 7 | 73 | 0 | 0 | 0 | 0 | 0 | 0 | 0 |
| **19-20** | 69 | 30 | 0 | 0 | 0 | 0 | 0 | 0 | 0 |
| **29-30** | 32 | 16 | 0 | 0 | 0 | 0 | 0 | 0 | 0 |
| **39-40** | 11 | 38 | 0 | 0 | 0 | 0 | 0 | 0 | 0 |
| **49-50** | 8 | 92 | 0 | 0 | 0 | 0 | 0 | 0 | 0 |
| **59-60** | 17 | 0 | 0 | 0 | 0 | 0 | 0 | 0 | 0 |
| **69-70** | 24 | 0 | 0 | 0 | 0 | 0 | 0 | 0 | 0 |
| **79-80** | 27 | 0 | 0 | 0 | 0 | 0 | 0 | 0 | 0 |
| **89-90** | 25 | 0 | 0 | 0 | 0 | 0 | 0 | 0 | 0 |
| **99-100** | 24 | 0 | 0 | 0 | 0 | 0 | 0 | 0 | 0 |
| **109-110** | 21 | 0 | 0 | 0 | 0 | 0 | 0 | 0 | 0 |
| **119-120** | 20 | 0 | 0 | 0 | 0 | 0 | 0 | 0 | 0 |
| **129-130** | 18 | 0 | 0 | 0 | 0 | 0 | 0 | 0 | 0 |
| **139-140** | 0 | 0 | 10 | 11 | 3 | 9 | 2 | 0 | 0 |
| **149-150** | 0 | 0 | 8 | 17 | 0 | 4 | 0 | 0 | 4 |
| **153.5-154.5** | 13 | 0 | 90 | 62 | 0 | 56 | 8 | 0 | 4 |
| **160** | 0 | 0 | 7 | 5 | 0 | 0 | 0 | 0 | 0 |
| **169-170** | 0 | 0 | 0 | 0 | 0 | 0 | 0 | 0 | 0 |
| **179-180** | 0 | 0 | 0 | 0 | 0 | 0 | 0 | 0 | 0 |
| **189-190** | 0 | 0 | 0 | 0 | 0 | 0 | 0 | 0 | 0 |
| **195-196** | 0 | 0 | 0 | 0 | 0 | 0 | 0 | 0 | 0 |
| **199-200** | 10 | 0 | 0 | 0 | 0 | 0 | 0 | 0 | 0 |
| **209-210** | 0 | 0 | 0 | 0 | 0 | 0 | 0 | 0 | 0 |
| **219-220** | 0 | 0 | 0 | 0 | 0 | 0 | 0 | 0 | 0 |

**Appendix 1.2:** Raw counts of Charophyte oogonia for Loch Duart Marsh

| Depth in core (cm) | Charophyte oogonia |
|---|---|
| **9-10** | 0 |
| **19-20** | 0 |
| **29-30** | 0 |
| **39-40** | 0 |
| **49-50** | 0 |
| **59-60** | 0 |
| **69-70** | 0 |
| **79-80** | 0 |
| **89-90** | 0 |
| **99-100** | 0 |
| **109-110** | 0 |
| **119-120** | 0 |
| **129-130** | 0 |
| **139-140** | 0 |
| **149-150** | 1 |
| **153.5-154.5** | 4 |
| **160** | 0 |
| **169-170** | 4 |
| **179-180** | 0 |
| **189-190** | 0 |
| **195-196** | 60 |
| **199-200** | 20 |
| **209-210** | 0 |
| **219-220** | 0 |

**Appendix 2:** Table showing data received from Northwestern University on samples from the LDM-20-JT core. The samples were analysed for Wt% C, δ $^{13}$C VPDB, Wt% N, C/N, Wt% S and C/S.

NORTHWESTERN UNIVERSITY

*Department of Earth and Planetary Sciences*

*NU Stable Isotope Biogeochemistry Laboratory (NUSIBL)*

**2205 Tech Drive, 3-150 Hogan, Evanston, IL 60208 | Ph: 847.467.6346**
**Manager: Dr. Andrew Masterson | Ph: 847.467.6346 |E-mail: andyM@earth.northwestern.edu**

**Sample description: Loch TOC and wt% S**

**Analysis type: CN and S**

**Principal Investigator: Selby/Sageman**

**Sample preparation: GCS/ALM**

**Project and Chart String:** **N=26**

**Submission date: 01/02/2021** **Analysis Date: 01/04/2021**

| Identifier 1 | Wt% C | Wt% C dup | δ $^{13}$C VPDB | δ $^{13}$C VPDB dup | Wt% N | Wt% N dup | C/N | C/N dup | Wt% S | Wt% s dup | C/S |
|---|---|---|---|---|---|---|---|---|---|---|---|
| JT-01 | 23.56 | | -25.65 | | 2.18 | | 10.82 | | 3.61 | | 6.53 |
| JT-02 | 24.90 | | -25.78 | | 2.20 | | 11.33 | | 2.83 | | 8.80 |
| JT-03 | 23.76 | | -25.96 | | 1.94 | | 12.24 | | 3.01 | | 7.89 |
| JT-04 | 24.01 | | -26.26 | | 1.69 | | 14.21 | | 3.81 | | 6.31 |
| JT-05 | 26.24 | | -26.59 | | 1.78 | | 14.75 | | 3.29 | | 7.98 |
| JT-06 | 16.34 | | -24.49 | | 1.42 | | 11.54 | | 2.98 | | 5.47 |
| JT-07 | 9.77 | | -20.62 | | 1.00 | | 9.78 | | 2.22 | | 4.41 |
| JT-08 | 8.29 | | -20.72 | | 0.84 | | 9.92 | | 2.12 | | 3.91 |
| JT-09 | 8.53 | | -20.83 | | 0.88 | | 9.67 | | 2.36 | | 3.61 |
| JT-10 | 9.01 | | -21.59 | | 0.90 | | 9.97 | | 1.72 | | 5.25 |

| | | | | | | | | | | | |
|---|---|---|---|---|---|---|---|---|---|---|---|
| JT-11 | 6.33 | 6.58 | -21.00 | -20.92 | 0.63 | 0.66 | 10.10 | 10.04 | 1.93 | 1.76 | 3.29 |
| JT-12 | 7.95 | | -21.49 | | 0.70 | | 11.38 | | 2.22 | | 3.58 |
| JT-13 | 7.61 | | -21.39 | | 0.67 | | 11.40 | | 2.30 | | 3.30 |
| JT-14 | 7.35 | | -19.68 | | 0.62 | | 11.93 | | 1.49 | | 4.95 |
| JT-15 | 7.54 | | -20.11 | | 0.57 | | 13.12 | | 1.87 | | 4.03 |
| JT-16 | 7.03 | | -19.90 | | 0.58 | | 12.12 | | 1.72 | | 4.08 |
| JT-17 | 12.75 | | -22.07 | | 0.70 | | 18.24 | | 2.53 | | 5.05 |
| JT-18 | 8.87 | | -19.68 | | 0.52 | | 17.22 | | 2.23 | | 3.98 |
| JT-19 | 10.07 | | -17.52 | | 0.54 | | 18.59 | | 1.87 | | 5.39 |
| JT-20 | 7.43 | | -16.84 | | 0.48 | | 15.36 | | 1.16 | | 6.39 |
| JT-21 | 10.62 | 10.77 | -16.70 | -17.37 | 0.68 | 0.68 | 15.70 | 15.84 | 2.80 | 1.97 | 3.79 |
| JT-22 | 11.23 | | -16.75 | | 0.73 | | 15.49 | | 2.10 | | 5.35 |
| JT-23 | 2.90 | | -18.53 | | 0.26 | | 11.16 | | 1.22 | | 2.37 |
| JT-24 | 1.04 | | -19.53 | | 0.09 | | 12.13 | | 1.37 | | 0.76 |
| JT-25 | 1.13 | | -19.73 | | 0.09 | | 12.20 | | 1.37 | | 0.82 |
| JT-26 | 0.90 | 0.86 | -14.96 | -14.70 | 0.07 | 0.07 | 12.42 | 12.19 | 1.26 | 1.36 | 0.71 |

**Appendix 3:** Table showing rhenium and osmium isotopic analysis with associated errors

| Batch/Sample | Core | Depth (cm) | Re (ppb) | ± | $Os_T$ (ppt) | ± | $^{192}Os$ (ppt) | ± | $^{187}Re/^{188}Os$ | ± | $^{187}Os/^{188}Os$ | ± | rho | % Re Blank | % $^{187}Os$ Blank | % $^{188}Os$ Blank | $Os_i$ | ± |
|---|---|---|---|---|---|---|---|---|---|---|---|---|---|---|---|---|---|---|
| RO1193-1_JT31-10-11cm | LDM 2020 | 10-11 | 2.37 | 0.01 | 63.0 | 0.4 | 23.1 | 0.2 | 204.0 | 2.1 | 1.095 | 0.011 | 0.845 | 2.56 | 0.16 | 0.87 | 1.09 | 0.011 |
| RO1158-12_JT-17 | Archive 2016 | 39-40 | 10.46 | 0.01 | 56.9 | 0.2 | 21.1 | 0.1 | 985.0 | 4.8 | 0.983 | 0.006 | 0.808 | 0.32 | 0.08 | 0.38 | 0.983 | 0.006 |
| RO1187-1_JT35-55-56cm | LDM 2020 | 55-56 | 18.30 | 0.01 | 46.2 | 0.4 | 17.1 | 0.3 | 2129.5 | 31.1 | 1.011 | 0.023 | 0.638 | 0.34 | 0.12 | 0.59 | 1.011 | 0.023 |
| RO1158-12_JT-14 | Archive 2016 | 74-75 | 24.09 | 0.01 | 88.9 |  | 33.3 | 0.4 | 1440.4 | 16.7 | 0.921 | 0.018 | 0.608 | 0.14 | 0.05 | 0.24 | 0.920 | 0.018 |
| RO1193-3_JT9-90cm | LDM 2020 | 90 | 26.78 | 0.02 | 79.0 | 0.4 | 29.0 | 0.2 | 1840.1 | 10.1 | 1.093 | 0.007 | 0.861 | 0.15 | 0.08 | 0.46 | 1.09 | 0.007 |
| RO1158-12_JT-12 | Archive 2016 | 104-105 | 18.91 | 0.01 | 88.5 | 0.3 | 33.2 | 0.1 | 1134.3 | 3.5 | 0.908 | 0.004 | 0.776 | 0.18 | 0.05 | 0.24 | 0.908 | 0.004 |
| RO1193-4_JT12-120cm | LDM 2020 | 120 | 18.82 | 0.06 | 87.2 | 0.4 | 32.3 | 0.2 | 1158.8 | 6.8 | 0.998 | 0.006 | 0.724 | 0.22 | 0.08 | 0.42 | 1.00 | 0.006 |
| RO1187-9_JT18-140-141cm | LDM 2020 | 140-141 | 18.97 | 0.01 | 84.2 | 0.3 | 31.8 | 0.2 | 1185.8 | 5.7 | 0.832 | 0.005 | 0.722 | 0.16 | 0.08 | 0.32 | 0.831 | 0.005 |
| RO1096-1_142-144cm | Archive 2016 | 142-144 | 21.31 | 0.01 | 78.8 | 0.3 | 29.2 | 0.1 | 1452.6 | 5.0 | 1.013 | 0.004 | 0.817 | 0.16 | 0.05 | 0.28 | 1.013 | 0.004 |
| RO1187-8_JT15-150.5-151.5cm | LDM 2020 | 150.5-151.5 | 14.83 | 0.01 | 108.8 | 0.5 | 40.0 | 0.2 | 736.9 | 3.5 | 1.061 | 0.007 | 0.693 | 0.21 | 0.05 | 0.25 | 1.060 | 0.007 |
| RO1187-7_JT16-152-153cm | LDM 2020 | 152-153 | 17.21 | 0.04 | 102.4 | 0.4 | 38.5 | 0.2 | 890.2 | 4.0 | 0.887 | 0.005 | 0.667 | 0.18 | 0.06 | 0.26 | 0.886 | 0.005 |
| RO1191-5_JT16-152-153cm | LDM 2020 | 152-153 | 16.33 | 0.05 | 108.8 | 0.5 | 41.0 | 0.2 | 793.3 | 5.1 | 0.871 | 0.007 | 0.664 | 0.25 | 0.07 | 0.32 | 0.87 | 0.007 |
| RO1191-4_JT38-154-155cm | LDM 2020 | 154-155 | 14.63 | 0.04 | 85.8 | 0.4 | 31.5 | 0.2 | 924.3 | 6.2 | 1.091 | 0.009 | 0.714 | 0.28 | 0.08 | 0.42 | 1.09 | 0.009 |
| RO1193-5_JT17-160-161cm | LDM 2020 | 160-161 | 12.58 | 0.04 | 256.0 | 1.0 | 91.4 | 0.3 | 273.9 | 1.2 | 1.326 | 0.006 | 0.540 | 0.32 | 0.02 | 0.15 | 1.33 | 0.006 |

| | | | | | | | | | | | | | | | | | | |
|---|---|---|---|---|---|---|---|---|---|---|---|---|---|---|---|---|---|---|
| RO1187-5_JT18-165-166cm | LDM 2020 | 165-166 | 15.20 | 0.01 | 251.8 | 1.2 | 82.9 | 0.3 | 364.5 | 1.3 | 2.067 | 0.011 | 0.702 | 0.27 | 0.02 | 0.16 | 2.07 | 0.011 |
| RO1191-3_JT37-168-169cm | LDM 2020 | 168-169 | 11.49 | 0.04 | 142.9 | 1.0 | 43.3 | 0.3 | 528.5 | 3.5 | 2.914 | 0.023 | 0.643 | 0.36 | 0.02 | 0.31 | 2.91 | 0.023 |
| RO1096-2_169cm | Archive 2016 | 169 | 20.08 | 0.01 | 230.4 | 1.0 | 69.5 | 0.2 | 575.0 | 1.4 | 2.960 | 0.010 | 0.691 | 0.17 | 0.01 | 0.12 | 2.960 | 0.010 |
| RO1158-6_JT-06 | Archive 2016 | 169-170 | 16.49 | 0.01 | 197.8 | 1.0 | 56.1 | 0.2 | 584.3 | 1.9 | 3.614 | 0.016 | 0.711 | 0.21 | 0.01 | 0.14 | 3.614 | 0.016 |
| RO1191-2_JT19-170-171cm | LDM 2020 | 170-171 | 17.09 | 0.05 | 171.0 | 1.3 | 46.8 | 0.3 | 726.2 | 4.6 | 4.020 | 0.031 | 0.662 | 0.24 | 0.01 | 0.29 | 4.02 | 0.031 |
| RO1187-3_JT20-175-176cm | LDM 2020 | 175-176 | 8.79 | 0.01 | 153.5 | 1.0 | 42.7 | 0.2 | 409.7 | 1.8 | 3.846 | 0.023 | 0.717 | 0.34 | 0.01 | 0.23 | 3.846 | 0.023 |
| RO1191-1_JT36-178-179cm | LDM 2020 | 178-179 | 6.43 | 0.03 | 192.3 | 1.9 | 51.4 | 0.4 | 248.9 | 2.4 | 4.292 | 0.053 | 0.582 | 0.63 | 0.01 | 0.25 | 4.29 | 0.053 |
| RO1187-2_JT21-180-181cm | LDM 2020 | 180-181 | 10.80 | 0.01 | 274.2 | 1.8 | 69.8 | 0.3 | 307.7 | 1.3 | 4.887 | 0.028 | 0.704 | 0.39 | 0.01 | 0.19 | 4.887 | 0.028 |
| RO1158-5_JT-05 | Archive 2016 | 182-183 | 16.06 | 0.01 | 226.7 | 1.2 | 60.4 | 0.2 | 529.2 | 1.6 | 4.346 | 0.018 | 0.698 | 0.21 | 0.01 | 0.13 | 4.346 | 0.018 |
| RO1181-6_JT22_185-186 | LDM 2020 | 185-186 | 8.82 | 0.01 | 302.0 | 1.6 | 84.9 | 0.3 | 206.6 | 0.7 | 3.715 | 0.016 | 0.709 | 0.47 | 0.01 | 0.16 | 3.715 | 0.016 |
| RO1158-4_JT-04 | Archive 2016 | 190.5-191.5 | 9.69 | 0.01 | 328.5 | 2.0 | 99.0 | 0.4 | 194.6 | 0.9 | 2.958 | 0.020 | 0.669 | 0.35 | 0.01 | 0.08 | 2.958 | 0.020 |
| RO1173-1_JT23 | LDM 2020 | 191-192 | 3.97 | 0.01 | 131.8 | 0.7 | 40.6 | 0.2 | 194.3 | 0.9 | 2.732 | 0.014 | 0.779 | 1.43 | 0.02 | 0.33 | 2.732 | 0.014 |
| RO1181-7_JT28_195-196 | LDM 2020 | 195-196 | 3.22 | 0.00 | 100.3 | 0.7 | 32.0 | 0.2 | 200.4 | 1.3 | 2.379 | 0.023 | 0.661 | 0.77 | 0.02 | 0.25 | 2.379 | 0.023 |
| RO1164-3_JT-03 | Archive 2016 | 197-198 | 9.88 | 0.01 | 455.1 | 2.3 | 149.1 | 0.6 | 131.8 | 0.5 | 2.120 | 0.012 | 0.676 | 0.57 | 0.00 | 0.04 | 2.120 | 0.012 |
| RO1173-2_JT24 | LDM 2020 | 200-201 | 3.57 | 0.01 | 72.4 | 0.4 | 23.9 | 0.2 | 296.5 | 1.9 | 2.032 | 0.014 | 0.881 | 1.59 | 0.06 | 0.56 | 2.032 | 0.014 |
| RO1158-2_JT-02 | Archive 2016 | 202-203 | 2.41 | 0.00 | 103.8 | 0.6 | 35.8 | 0.2 | 134.1 | 0.7 | 1.652 | 0.012 | 0.683 | 0.71 | 0.01 | 0.11 | 1.652 | 0.012 |
| RO1164-2_JT-02 | Archive 2016 | 202-203 | 2.68 | 0.00 | 117.4 | 0.5 | 39.6 | 0.1 | 134.6 | 0.5 | 1.848 | 0.009 | 0.659 | 1.27 | 0.01 | 0.10 | 1.848 | 0.009 |

| | | | | | | | | | | | | | | | | | | |
|---|---|---|---|---|---|---|---|---|---|---|---|---|---|---|---|---|---|---|
| RO1181-8_JT27_204-205 | LDM 2020 | 204-205 | 3.38 | 0.00 | 91.5 | 0.4 | 31.9 | 0.1 | 210.7 | 0.9 | 1.537 | 0.008 | 0.736 | 0.74 | 0.03 | 0.25 | 1.537 | 0.008 |
| RO1173-3_JT25 | LDM 2020 | 208-209 | 3.12 | 0.00 | 90.8 | 0.4 | 32.1 | 0.1 | 193.0 | 0.7 | 1.407 | 0.006 | 0.753 | 1.09 | 0.04 | 0.25 | 1.407 | 0.006 |
| RO1096-3_209-211cm | Archive 2016 | 209-211 | 3.62 | 0.00 | 100.9 | 0.7 | 35.8 | 0.3 | 201.2 | 1.6 | 1.391 | 0.016 | 0.707 | 0.47 | 0.02 | 0.11 | 1.391 | 0.016 |
| RO1180-5_JT29_211.5-212.5 | LDM 2020 | 211.5-212.5 | 3.22 | 0.00 | 106.3 | 0.4 | 38.3 | 0.1 | 167.0 | 0.7 | 1.238 | 0.007 | 0.664 | 1.06 | 0.03 | 0.21 | 1.238 | 0.007 |
| RO1180-3_JT30_214-215 | LDM 2020 | 214-215 | 2.24 | 0.01 | 86.8 | 0.7 | 31.5 | 0.3 | 141.6 | 1.6 | 1.175 | 0.023 | 0.545 | 1.51 | 0.04 | 0.26 | 1.175 | 0.023 |
| RO1173-4_JT26 | LDM 2020 | 218-220 | 1.34 | 0.00 | 102.7 | 0.4 | 37.8 | 0.1 | 70.7 | 0.3 | 1.059 | 0.004 | 0.575 | 2.53 | 0.04 | 0.21 | 1.059 | 0.004 |

**Appendix 4:** Beta Analytic report of radiocarbon dating analyses for samples taken from LDM-20-JT

Beta Analytic, Inc.
4985 SW 74th Court
Miami, FL 33155 USA
Tel: 305-667-5167
Fax: 305-663-0964
info@betalabservices.com

ISO/IEC 17025:2017-Accredited Testing Laboratory

## REPORT OF RADIOCARBON DATING ANALYSES

Jeremy Lloyd — Report Date: September 07, 2021

University of Durham — Material Received: August 12, 2021

| Laboratory Number | Sample Code Number | Conventional Radiocarbon Age (BP) or Percent Modern Carbon (pMC) & Stable Isotopes | |
|---|---|---|---|
| **Beta - 600245** | **LDM-54 organic sediment** | **560 +/- 30 BP** | IRMS δ13C: -25.0 o/oo |
| **(48.5%)** | **1312 - 1362 cal AD** | **(638 - 588 cal BP)** | |
| **(46.9%)** | **1386 - 1428 cal AD** | **(564 - 522 cal BP)** | |

Submitter Material: Organic Sediment/Gyttja
Pretreatment: (organic sediment) acid washes
Analyzed Material: Organic sediment
Analysis Service: AMS-Standard delivery
Percent Modern Carbon: 93.27 +/- 0.35 pMC
Fraction Modern Carbon: 0.9327 +/- 0.0035
D14C: -67.34 +/- 3.48 o/oo
Δ14C: -75.31 +/- 3.48 o/oo (1950:2021)
Measured Radiocarbon Age: (without d13C correction): 560 +/- 30 BP
Calibration: BetaCal4.20: HPD method: INTCAL20

Results are ISO/IEC-17025:2017 accredited. No sub-contracting or student labor was used in the analyses. All work was done at Beta in 4 in-house NEC accelerator mass spectrometers and 4 Thermo IRMSs. The "Conventional Radiocarbon Age" was calculated using the Libby half-life (5568 years), is corrected for total isotopic fraction and was used for calendar calibration where applicable. The Age is rounded to the nearest 10 years and is reported as radiocarbon years before present (BP), "present" = AD 1950. Results greater than the modern reference are reported as percent modern carbon (pMC). The modern reference standard was 95% the 14C signature of NIST SRM-4990C (oxalic acid). Quoted errors are 1 sigma counting statistics. Calculated sigmas less than 30 BP on the Conventional Radiocarbon Age are conservatively rounded up to 30. d13C values are on the material itself (not the AMS d13C). d13C and d15N values are relative to VPDB. References for calendar calibrations are cited at the bottom of calibration graph pages.

Beta Analytic, Inc.
4985 SW 74th Court
Miami, FL 33155 USA
Tel: 305-667-5167
Fax: 305-663-0964
info@betalabservices.com

ISO/IEC 17025:2017-Accredited Testing Laboratory

# REPORT OF RADIOCARBON DATING ANALYSES

Jeremy Lloyd

University of Durham

Report Date: September 07, 2021

Material Received: August 12, 2021

| Laboratory Number | Sample Code Number | Conventional Radiocarbon Age (BP) or Percent Modern Carbon (pMC) & Stable Isotopes | |
|---|---|---|---|
| **Beta - 600246** | **LDM-100 organic sediment** | **2220 +/- 30 BP** | IRMS δ13C: -21.2 o/oo |
| **(95.4%)** | **385 - 197 cal BC** | **(2334 - 2146 cal BP)** | |

Submitter Material: Organic Sediment/Gyttja
Pretreatment: (organic sediment) acid washes
Analyzed Material: Organic sediment
Analysis Service: AMS-Standard delivery
Percent Modern Carbon: 75.85 +/- 0.28 pMC
Fraction Modern Carbon: 0.7585 +/- 0.0028
D14C: -241.46 +/- 2.83 o/oo
Δ14C: -247.95 +/- 2.83 o/oo (1950:2021)
Measured Radiocarbon Age: (without d13C correction): 2160 +/- 30 BP
Calibration: BetaCal4.20: HPD method: INTCAL20

Results are ISO/IEC-17025:2017 accredited. No sub-contracting or student labor was used in the analyses. All work was done at Beta in 4 in-house NEC accelerator mass spectrometers and 4 Thermo IRMSs. The "Conventional Radiocarbon Age" was calculated using the Libby half-life (5568 years), is corrected for total isotopic fraction and was used for calendar calibration where applicable. The Age is rounded to the nearest 10 years and is reported as radiocarbon years before present (BP), "present" = AD 1950. Results greater than the modern reference are reported as percent modern carbon (pMC). The modern reference standard was 95% the 14C signature of NIST SRM-4990C (oxalic acid). Quoted errors are 1 sigma counting statistics. Calculated sigmas less than 30 BP on the Conventional Radiocarbon Age are conservatively rounded up to 30. d13C values are on the material itself (not the AMS d13C). d13C and d15N values are relative to VPDB. References for calendar calibrations are cited at the bottom of calibration graph pages.

Beta Analytic, Inc.
4985 SW 74th Court
Miami, FL 33155 USA
Tel: 305-667-5167
Fax: 305-663-0964
info@betalabservices.com

ISO/IEC 17025:2017-Accredited Testing Laboratory

# REPORT OF RADIOCARBON DATING ANALYSES

Jeremy Lloyd

University of Durham

Report Date: September 07, 2021

Material Received: August 12, 2021

| Laboratory Number | Sample Code Number | Conventional Radiocarbon Age (BP) or Percent Modern Carbon (pMC) & Stable Isotopes | |
|---|---|---|---|
| **Beta - 600247** | **LDM-134 organic sediment** | **2250 +/- 30 BP** | IRMS δ13C: -20.9 o/oo |
| **(64.8%)** | **315 - 204 cal BC** | **(2264 - 2153 cal BP)** | |
| **(30.6%)** | **392 - 347 cal BC** | **(2341 - 2296 cal BP)** | |

Submitter Material: Organic Sediment/Gyttja
Pretreatment: (organic sediment) acid washes
Analyzed Material: Organic sediment
Analysis Service: AMS-Standard delivery
Percent Modern Carbon: 75.57 +/- 0.28 pMC
Fraction Modern Carbon: 0.7557 +/- 0.0028
D14C: -244.29 +/- 2.82 o/oo
Δ14C: -250.75 +/- 2.82 o/oo (1950:2021)
Measured Radiocarbon Age: (without d13C correction): 2180 +/- 30 BP
Calibration: BetaCal4.20: HPD method: INTCAL20

Results are ISO/IEC-17025:2017 accredited. No sub-contracting or student labor was used in the analyses. All work was done at Beta in 4 in-house NEC accelerator mass spectrometers and 4 Thermo IRMSs. The "Conventional Radiocarbon Age" was calculated using the Libby half-life (5568 years), is corrected for total isotopic fraction and was used for calendar calibration where applicable. The Age is rounded to the nearest 10 years and is reported as radiocarbon years before present (BP), "present" = AD 1950. Results greater than the modern reference are reported as percent modern carbon (pMC). The modern reference standard was 95% the 14C signature of NIST SRM-4990C (oxalic acid). Quoted errors are 1 sigma counting statistics. Calculated sigmas less than 30 BP on the Conventional Radiocarbon Age are conservatively rounded up to 30. d13C values are on the material itself (not the AMS d13C). d13C and d15N values are relative to VPDB. References for calendar calibrations are cited at the bottom of calibration graph pages.

**Beta Analytic, Inc.**
4985 SW 74th Court
Miami, FL 33155 USA
Tel: 305-667-5167
Fax: 305-663-0964
info@betalabservices.com

ISO/IEC 17025:2017-Accredited Testing Laboratory

# REPORT OF RADIOCARBON DATING ANALYSES

Jeremy Lloyd

University of Durham

Report Date: September 07, 2021

Material Received: August 12, 2021

| Laboratory Number | Sample Code Number | Conventional Radiocarbon Age (BP) or Percent Modern Carbon (pMC) & Stable Isotopes | |
|---|---|---|---|
| **Beta - 600248** | **LDM-146 organic sediment** | **5300 +/- 30 BP** | IRMS δ13C: -21.6 o/oo |
| **(94.0%)** | **4241 - 4044 cal BC** | **(6190 - 5993 cal BP)** | |
| **( 1.4%)** | **4009 - 4001 cal BC** | **(5958 - 5950 cal BP)** | |

Submitter Material: Organic Sediment/Gyttja
Pretreatment: (organic sediment) acid washes
Analyzed Material: Organic sediment
Analysis Service: AMS-Standard delivery
Percent Modern Carbon: 51.70 +/- 0.19 pMC
Fraction Modern Carbon: 0.5170 +/- 0.0019
D14C: -483.04 +/- 1.93 o/oo
Δ14C: -487.46 +/- 1.93 o/oo (1950:2021)
Measured Radiocarbon Age: (without d13C correction): 5240 +/- 30 BP
Calibration: BetaCal4.20: HPD method: INTCAL20

Results are ISO/IEC-17025:2017 accredited. No sub-contracting or student labor was used in the analyses. All work was done at Beta in 4 in-house NEC accelerator mass spectrometers and 4 Thermo IRMSs. The "Conventional Radiocarbon Age" was calculated using the Libby half-life (5568 years), is corrected for total isotopic fraction and was used for calendar calibration where applicable. The Age is rounded to the nearest 10 years and is reported as radiocarbon years before present (BP), "present" = AD 1950. Results greater than the modern reference are reported as percent modern carbon (pMC). The modern reference standard was 95% the 14C signature of NIST SRM-4990C (oxalic acid). Quoted errors are 1 sigma counting statistics. Calculated sigmas less than 30 BP on the Conventional Radiocarbon Age are conservatively rounded up to 30. d13C values are on the material itself (not the AMS d13C). d13C and d15N values are relative to VPDB. References for calendar calibrations are cited at the bottom of calibration graph pages.

**Beta Analytic, Inc.**
4985 SW 74th Court
Miami, FL 33155 USA
Tel: 305-667-5167
Fax: 305-663-0964
info@betalabservices.com

ISO/IEC 17025:2017-Accredited Testing Laboratory

# REPORT OF RADIOCARBON DATING ANALYSES

Jeremy Lloyd

University of Durham

Report Date: September 07, 2021

Material Received: August 12, 2021

| Laboratory Number | Sample Code Number | Conventional Radiocarbon Age (BP) or Percent Modern Carbon (pMC) & Stable Isotopes | |
|---|---|---|---|
| **Beta - 600249** | **LDM-180 organic sediment** | **11130 +/- 30 BP** | IRMS δ13C: -16.8 o/oo |

**(91.9%) 11166 - 11012 cal BC (13115 - 12961 cal BP)**
**( 3.5%) 11001 - 10978 cal BC (12950 - 12927 cal BP)**

Submitter Material: Organic Sediment/Gyttja
Pretreatment: (organic sediment) acid washes
Analyzed Material: Organic sediment
Analysis Service: AMS-Standard delivery
Percent Modern Carbon: 25.02 +/- 0.09 pMC
Fraction Modern Carbon: 0.2502 +/- 0.0009
D14C: -749.81 +/- 0.93 o/oo
Δ14C: -751.95 +/- 0.93 o/oo (1950:2021)
Measured Radiocarbon Age: (without d13C correction): 11000 +/- 30 BP
Calibration: BetaCal4.20: HPD method: INTCAL20

Results are ISO/IEC-17025:2017 accredited. No sub-contracting or student labor was used in the analyses. All work was done at Beta in 4 in-house NEC accelerator mass spectrometers and 4 Thermo IRMSs. The "Conventional Radiocarbon Age" was calculated using the Libby half-life (5568 years), is corrected for total isotopic fraction and was used for calendar calibration where applicable. The Age is rounded to the nearest 10 years and is reported as radiocarbon years before present (BP), "present" = AD 1950. Results greater than the modern reference are reported as percent modern carbon (pMC). The modern reference standard was 95% the 14C signature of NIST SRM-4990C (oxalic acid). Quoted errors are 1 sigma counting statistics. Calculated sigmas less than 30 BP on the Conventional Radiocarbon Age are conservatively rounded up to 30. d13C values are on the material itself (not the AMS d13C). d13C and d15N values are relative to VPDB. References for calendar calibrations are cited at the bottom of calibration graph pages.

Beta Analytic, Inc.
4985 SW 74th Court
Miami, FL 33155 USA
Tel: 305-667-5167
Fax: 305-663-0964
info@betalabservices.com

ISO/IEC 17025:2017-Accredited Testing Laboratory

# REPORT OF RADIOCARBON DATING ANALYSES

Jeremy Lloyd

University of Durham

Report Date: September 07, 2021

Material Received: August 12, 2021

| Laboratory Number | Sample Code Number | Conventional Radiocarbon Age (BP) or Percent Modern Carbon (pMC) & Stable Isotopes | |
|---|---|---|---|
| **Beta - 601750** | **LDM-54 plant** | **230 +/- 30 BP** | IRMS δ13C: -27.7 o/oo |
| **(42.7%)** | **1636 - 1685 cal AD** | **(314 - 265 cal BP)** | |
| **(42.4%)** | **1732 - 1805 cal AD** | **(218 - 145 cal BP)** | |
| **( 9.1%)** | **1927 - Post AD 1950** | **(23 - Post BP 0)** | |
| **( 1.1%)** | **1530 - 1538 cal AD** | **(420 - 412 cal BP)** | |

Submitter Material: Plant material
Pretreatment: (plant material) acid/alkali/acid
Analyzed Material: Plant material
Analysis Service: AMS-Standard delivery
Percent Modern Carbon: 97.18 +/- 0.36 pMC
Fraction Modern Carbon: 0.9718 +/- 0.0036
D14C: -28.23 +/- 3.63 o/oo
Δ14C: -36.54 +/- 3.63 o/oo (1950:2021)
Measured Radiocarbon Age: (without d13C correction): 270 +/- 30 BP
Calibration: BetaCal4.20: HPD method: INTCAL20

Results are ISO/IEC-17025:2017 accredited. No sub-contracting or student labor was used in the analyses. All work was done at Beta in 4 in-house NEC accelerator mass spectrometers and 4 Thermo IRMSs. The "Conventional Radiocarbon Age" was calculated using the Libby half-life (5568 years), is corrected for total isotopic fraction and was used for calendar calibration where applicable. The Age is rounded to the nearest 10 years and is reported as radiocarbon years before present (BP), "present" = AD 1950. Results greater than the modern reference are reported as percent modern carbon (pMC). The modern reference standard was 95% the 14C signature of NIST SRM-4990C (oxalic acid). Quoted errors are 1 sigma counting statistics. Calculated sigmas less than 30 BP on the Conventional Radiocarbon Age are conservatively rounded up to 30. d13C values are on the material itself (not the AMS d13C). d13C and d15N values are relative to VPDB. References for calendar calibrations are cited at the bottom of calibration graph pages.

Beta Analytic, Inc.
4985 SW 74th Court
Miami, FL 33155 USA
Tel: 305-667-5167
Fax: 305-663-0964
info@betalabservices.com

ISO/IEC 17025:2017-Accredited Testing Laboratory

# REPORT OF RADIOCARBON DATING ANALYSES

Jeremy Lloyd

University of Durham

Report Date: September 07, 2021

Material Received: August 12, 2021

| Laboratory Number | Sample Code Number | Conventional Radiocarbon Age (BP) or Percent Modern Carbon (pMC) & Stable Isotopes | |
|---|---|---|---|
| **Beta - 601751** | **LDM-100 plant** | **2310 +/- 30 BP** | IRMS δ13C: -24.6 o/oo |
| **(78.1%)** | **412 - 354 cal BC** | **(2361 - 2303 cal BP)** | |
| **(17.3%)** | **284 - 229 cal BC** | **(2233 - 2178 cal BP)** | |

Submitter Material: Plant material
Pretreatment: (plant material) acid/alkali/acid
Analyzed Material: Plant material
Analysis Service: AMS-Standard delivery
Percent Modern Carbon: 75.01 +/- 0.28 pMC
Fraction Modern Carbon: 0.7501 +/- 0.0028
D14C: -249.91 +/- 2.80 o/oo
Δ14C: -256.33 +/- 2.80 o/oo (1950:2021)
Measured Radiocarbon Age: (without d13C correction): 2300 +/- 30 BP
Calibration: BetaCal4.20: HPD method: INTCAL20

Results are ISO/IEC-17025:2017 accredited. No sub-contracting or student labor was used in the analyses. All work was done at Beta in 4 in-house NEC accelerator mass spectrometers and 4 Thermo IRMSs. The "Conventional Radiocarbon Age" was calculated using the Libby half-life (5568 years), is corrected for total isotopic fraction and was used for calendar calibration where applicable. The Age is rounded to the nearest 10 years and is reported as radiocarbon years before present (BP), "present" = AD 1950. Results greater than the modern reference are reported as percent modern carbon (pMC). The modern reference standard was 95% the 14C signature of NIST SRM-4990C (oxalic acid). Quoted errors are 1 sigma counting statistics. Calculated sigmas less than 30 BP on the Conventional Radiocarbon Age are conservatively rounded up to 30. d13C values are on the material itself (not the AMS d13C). d13C and d15N values are relative to VPDB. References for calendar calibrations are cited at the bottom of calibration graph pages.

Beta Analytic, Inc.
4985 SW 74th Court
Miami, FL 33155 USA
Tel: 305-667-5167
Fax: 305-663-0964
info@betalabservices.com

ISO/IEC 17025:2017-Accredited Testing Laboratory

# REPORT OF RADIOCARBON DATING ANALYSES

Jeremy Lloyd

University of Durham

Report Date: September 07, 2021

Material Received: August 12, 2021

| Laboratory Number | Sample Code Number | Conventional Radiocarbon Age (BP) or Percent Modern Carbon (pMC) & Stable Isotopes | |
|---|---|---|---|
| **Beta - 601752** | **LDM-134 plant** | **3080 +/- 30 BP** | IRMS δ13C: -25.3 o/oo |
| **(95.4%)** | **1422 - 1263 cal BC** | **(3371 - 3212 cal BP)** | |

Submitter Material: Plant material
Pretreatment: (plant material) acid/alkali/acid
Analyzed Material: Plant material
Analysis Service: AMS-Standard delivery
Percent Modern Carbon: 68.15 +/- 0.25 pMC
Fraction Modern Carbon: 0.6815 +/- 0.0025
D14C: -318.47 +/- 2.55 o/oo
Δ14C: -324.30 +/- 2.55 o/oo (1950:2021)
Measured Radiocarbon Age: (without d13C correction): 3090 +/- 30 BP
Calibration: BetaCal4.20: HPD method: INTCAL20

Results are ISO/IEC-17025:2017 accredited. No sub-contracting or student labor was used in the analyses. All work was done at Beta in 4 in-house NEC accelerator mass spectrometers and 4 Thermo IRMSs. The "Conventional Radiocarbon Age" was calculated using the Libby half-life (5568 years), is corrected for total isotopic fraction and was used for calendar calibration where applicable. The Age is rounded to the nearest 10 years and is reported as radiocarbon years before present (BP), "present" = AD 1950. Results greater than the modern reference are reported as percent modern carbon (pMC). The modern reference standard was 95% the 14C signature of NIST SRM-4990C (oxalic acid). Quoted errors are 1 sigma counting statistics. Calculated sigmas less than 30 BP on the Conventional Radiocarbon Age are conservatively rounded up to 30. d13C values are on the material itself (not the AMS d13C). d13C and d15N values are relative to VPDB. References for calendar calibrations are cited at the bottom of calibration graph pages.

Beta Analytic, Inc.
4985 SW 74th Court
Miami, FL 33155 USA
Tel: 305-667-5167
Fax: 305-663-0964
info@betalabservices.com

ISO/IEC 17025:2017-Accredited Testing Laboratory

# REPORT OF RADIOCARBON DATING ANALYSES

Jeremy Lloyd

University of Durham

Report Date: September 07, 2021

Material Received: August 12, 2021

| Laboratory Number | Sample Code Number | Conventional Radiocarbon Age (BP) or Percent Modern Carbon (pMC) & Stable Isotopes | |
|---|---|---|---|
| **Beta - 601753** | **LDM-146 plant** | **4500 +/- 30 BP** | IRMS δ13C: -26.8 o/oo |
| **(95.4%)** | **3351 - 3096 cal BC** | **(5300 - 5045 cal BP)** | |

Submitter Material: Plant material
Pretreatment: (plant material) acid/alkali/acid
Analyzed Material: Plant material
Analysis Service: AMS-Standard delivery
Percent Modern Carbon: 57.11 +/- 0.21 pMC
Fraction Modern Carbon: 0.5711 +/- 0.0021
D14C: -428.90 +/- 2.13 o/oo
Δ14C: -433.79 +/- 2.13 o/oo (1950:2021)
Measured Radiocarbon Age: (without d13C correction): 4530 +/- 30 BP
Calibration: BetaCal4.20: HPD method: INTCAL20

Results are ISO/IEC-17025:2017 accredited. No sub-contracting or student labor was used in the analyses. All work was done at Beta in 4 in-house NEC accelerator mass spectrometers and 4 Thermo IRMSs. The "Conventional Radiocarbon Age" was calculated using the Libby half-life (5568 years), is corrected for total isotopic fraction and was used for calendar calibration where applicable. The Age is rounded to the nearest 10 years and is reported as radiocarbon years before present (BP), "present" = AD 1950. Results greater than the modern reference are reported as percent modern carbon (pMC). The modern reference standard was 95% the 14C signature of NIST SRM-4990C (oxalic acid). Quoted errors are 1 sigma counting statistics. Calculated sigmas less than 30 BP on the Conventional Radiocarbon Age are conservatively rounded up to 30. d13C values are on the material itself (not the AMS d13C). d13C and d15N values are relative to VPDB. References for calendar calibrations are cited at the bottom of calibration graph pages.

Beta Analytic, Inc.
4985 SW 74th Court
Miami, FL 33155 USA
Tel: 305-667-5167
Fax: 305-663-0964
info@betalabservices.com

ISO/IEC 17025:2017-Accredited Testing Laboratory

# REPORT OF RADIOCARBON DATING ANALYSES

Jeremy Lloyd

University of Durham

Report Date: September 07, 2021

Material Received: August 12, 2021

| Laboratory Number | Sample Code Number | Conventional Radiocarbon Age (BP) or Percent Modern Carbon (pMC) & Stable Isotopes | |
|---|---|---|---|
| **Beta - 601754** | **LDM-180 plant** | **10800 +/- 40 BP** | IRMS δ13C: -16.7 o/oo |

**(90.3%) 10835 - 10767 cal BC (12784 - 12716 cal BP)**
**( 5.1%) 10874 - 10846 cal BC (12823 - 12795 cal BP)**

Submitter Material: Plant material
Pretreatment: (plant material) acid/alkali/acid
Analyzed Material: Plant material
Analysis Service: AMS-Standard delivery
Percent Modern Carbon: 26.07 +/- 0.13 pMC
Fraction Modern Carbon: 0.2607 +/- 0.0013
D14C: -739.32 +/- 1.30 o/oo
Δ14C: -741.55 +/- 1.30 o/oo (1950:2021)
Measured Radiocarbon Age: (without d13C correction): 10660 +/- 40 BP
Calibration: BetaCal4.20: HPD method: INTCAL20

Results are ISO/IEC-17025:2017 accredited. No sub-contracting or student labor was used in the analyses. All work was done at Beta in 4 in-house NEC accelerator mass spectrometers and 4 Thermo IRMSs. The "Conventional Radiocarbon Age" was calculated using the Libby half-life (5568 years), is corrected for total isotopic fraction and was used for calendar calibration where applicable. The Age is rounded to the nearest 10 years and is reported as radiocarbon years before present (BP), "present" = AD 1950. Results greater than the modern reference are reported as percent modern carbon (pMC). The modern reference standard was 95% the 14C signature of NIST SRM-4990C (oxalic acid). Quoted errors are 1 sigma counting statistics. Calculated sigmas less than 30 BP on the Conventional Radiocarbon Age are conservatively rounded up to 30. d13C values are on the material itself (not the AMS d13C). d13C and d15N values are relative to VPDB. References for calendar calibrations are cited at the bottom of calibration graph pages.

**Beta Analytic, Inc.**
4985 SW 74th Court
Miami, FL 33155 USA
Tel: 305-667-5167
Fax: 305-663-0964
info@betalabservices.com

ISO/IEC 17025:2017-Accredited Testing Laboratory

# REPORT OF RADIOCARBON DATING ANALYSES

Jeremy Lloyd

University of Durham

Report Date: May 04, 2021

Material Received: April 21, 2021

| Laboratory Number | Sample Code Number | Conventional Radiocarbon Age (BP) or Percent Modern Carbon (pMC) & Stable Isotopes | |
|---|---|---|---|
| **Beta - 590335** | **LDM2020 - 158cm plant** | **9560 +/- 30 BP** | IRMS δ13C: -19.2 o/oo |

| | | |
|---|---|---|
| **(50.1%)** | **9136 - 8962 cal BC** | **(11085 - 10911 cal BP)** |
| **(45.3%)** | **8947 - 8773 cal BC** | **(10896 - 10722 cal BP)** |

Submitter Material: Organics
Pretreatment: (plant material) acid/alkali/acid
Analyzed Material: Plant material
Analysis Service: AMS-Standard delivery
Percent Modern Carbon: 30.42 +/- 0.11 pMC
Fraction Modern Carbon: 0.3042 +/- 0.0011
D14C: -695.81 +/- 1.14 o/oo
Δ14C: -698.41 +/- 1.14 o/oo (1950:2021)
Measured Radiocarbon Age: (without d13C correction): 9470 +/- 30 BP
Calibration: BetaCal4.20: HPD method: INTCAL20

Results are ISO/IEC-17025:2017 accredited. No sub-contracting or student labor was used in the analyses. All work was done at Beta in 4 in-house NEC accelerator mass spectrometers and 4 Thermo IRMSs. The "Conventional Radiocarbon Age" was calculated using the Libby half-life (5568 years), is corrected for total isotopic fraction and was used for calendar calibration where applicable. The Age is rounded to the nearest 10 years and is reported as radiocarbon years before present (BP), "present" = AD 1950. Results greater than the modern reference are reported as percent modern carbon (pMC). The modern reference standard was 95% the 14C signature of NIST SRM-4990C (oxalic acid). Quoted errors are 1 sigma counting statistics. Calculated sigmas less than 30 BP on the Conventional Radiocarbon Age are conservatively rounded up to 30. d13C values are on the material itself (not the AMS d13C). d13C and d15N values are relative to VPDB-1. References for calendar calibrations are cited at the bottom of calibration graph pages.

**Beta Analytic, Inc.**
4985 SW 74th Court
Miami, FL 33155 USA
Tel: 305-667-5167
Fax: 305-663-0964
info@betalabservices.com

ISO/IEC 17025:2017-Accredited Testing Laboratory

# REPORT OF RADIOCARBON DATING ANALYSES

Jeremy Lloyd

University of Durham

Report Date: May 04, 2021

Material Received: April 21, 2021

| Laboratory Number | Sample Code Number | Conventional Radiocarbon Age (BP) or Percent Modern Carbon (pMC) & Stable Isotopes | |
|---|---|---|---|
| **Beta - 590336** | **LDM2020 - 162cm plant** | **9390 +/- 30 BP** | IRMS δ13C: -19.7 o/oo |

| | | |
|---|---|---|
| **(87.6%)** | **8753 - 8602 cal BC** | **(10702 - 10551 cal BP)** |
| **( 7.8%)** | **8596 - 8561 cal BC** | **(10545 - 10510 cal BP)** |

Submitter Material: Organics
Pretreatment: (plant material) acid/alkali/acid
Analyzed Material: Plant material
Analysis Service: AMS-Standard delivery
Percent Modern Carbon: 31.07 +/- 0.12 pMC
Fraction Modern Carbon: 0.3107 +/- 0.0012
D14C: -689.30 +/- 1.16 o/oo
Δ14C: -691.96 +/- 1.16 o/oo (1950:2021)
Measured Radiocarbon Age: (without d13C correction): 9300 +/- 30 BP
Calibration: BetaCal4.20: HPD method: INTCAL20

Results are ISO/IEC-17025:2017 accredited. No sub-contracting or student labor was used in the analyses. All work was done at Beta in 4 in-house NEC accelerator mass spectrometers and 4 Thermo IRMSs. The "Conventional Radiocarbon Age" was calculated using the Libby half-life (5568 years), is corrected for total isotopic fraction and was used for calendar calibration where applicable. The Age is rounded to the nearest 10 years and is reported as radiocarbon years before present (BP), "present" = AD 1950. Results greater than the modern reference are reported as percent modern carbon (pMC). The modern reference standard was 95% the 14C signature of NIST SRM-4990C (oxalic acid). Quoted errors are 1 sigma counting statistics. Calculated sigmas less than 30 BP on the Conventional Radiocarbon Age are conservatively rounded up to 30. d13C values are on the material itself (not the AMS d13C). d13C and d15N values are relative to VPDB-1. References for calendar calibrations are cited at the bottom of calibration graph pages.

**Beta Analytic, Inc.**
4985 SW 74th Court
Miami, FL 33155 USA
Tel: 305-667-5167
Fax: 305-663-0964
info@betalabservices.com

ISO/IEC 17025:2017-Accredited Testing Laboratory

# REPORT OF RADIOCARBON DATING ANALYSES

Jeremy Lloyd

University of Durham

Report Date: May 04, 2021

Material Received: April 21, 2021

| Laboratory Number | Sample Code Number | Conventional Radiocarbon Age (BP) or Percent Modern Carbon (pMC) & Stable Isotopes | |
|---|---|---|---|
| **Beta - 590878** | **LDM2020 - 158cm organic sediment** | **9150 +/- 30 BP** | IRMS δ13C: -23.3 o/oo |

**(95.4%) 8458 - 8286 cal BC (10407 - 10235 cal BP)**

Submitter Material: Organics
Pretreatment: (organic sediment) acid washes
Analyzed Material: Organic sediment
Analysis Service: AMS-Standard delivery
Percent Modern Carbon: 32.01 +/- 0.12 pMC
Fraction Modern Carbon: 0.3201 +/- 0.0012
D14C: -679.88 +/- 1.20 o/oo
Δ14C: -682.62 +/- 1.20 o/oo (1950:2021)
Measured Radiocarbon Age: (without d13C correction): 9120 +/- 30 BP
Calibration: BetaCal4.20: HPD method: INTCAL20

Results are ISO/IEC-17025:2017 accredited. No sub-contracting or student labor was used in the analyses. All work was done at Beta in 4 in-house NEC accelerator mass spectrometers and 4 Thermo IRMSs. The "Conventional Radiocarbon Age" was calculated using the Libby half-life (5568 years), is corrected for total isotopic fraction and was used for calendar calibration where applicable. The Age is rounded to the nearest 10 years and is reported as radiocarbon years before present (BP), "present" = AD 1950. Results greater than the modern reference are reported as percent modern carbon (pMC). The modern reference standard was 95% the 14C signature of NIST SRM-4990C (oxalic acid). Quoted errors are 1 sigma counting statistics. Calculated sigmas less than 30 BP on the Conventional Radiocarbon Age are conservatively rounded up to 30. d13C values are on the material itself (not the AMS d13C). d13C and d15N values are relative to VPDB-1. References for calendar calibrations are cited at the bottom of calibration graph pages.

Beta Analytic, Inc.
4985 SW 74th Court
Miami, FL 33155 USA
Tel: 305-667-5167
Fax: 305-663-0964
info@betalabservices.com

ISO/IEC 17025:2017-Accredited Testing Laboratory

# REPORT OF RADIOCARBON DATING ANALYSES

Jeremy Lloyd

University of Durham

Report Date: May 04, 2021

Material Received: April 21, 2021

| Laboratory Number | Sample Code Number | Conventional Radiocarbon Age (BP) or Percent Modern Carbon (pMC) & Stable Isotopes | |
|---|---|---|---|
| **Beta - 590957** | **LDM2020 - 162cm organic sediment** | **9330 +/- 30 BP** | IRMS δ13C: -23.0 o/oo |

| | | |
|---|---|---|
| **(76.8%)** | **8648 - 8537 cal BC** | **(10597 - 10486 cal BP)** |
| **(10.7%)** | **8515 - 8474 cal BC** | **(10464 - 10423 cal BP)** |
| **( 7.9%)** | **8704 - 8670 cal BC** | **(10653 - 10619 cal BP)** |

Submitter Material: Organics
Pretreatment: (organic sediment) acid washes
Analyzed Material: Organic sediment
Analysis Service: AMS-Standard delivery
Percent Modern Carbon: 31.30 +/- 0.12 pMC
Fraction Modern Carbon: 0.3130 +/- 0.0012
D14C: -686.97 +/- 1.17 o/oo
Δ14C: -689.65 +/- 1.17 o/oo (1950:2021)
Measured Radiocarbon Age: (without d13C correction): 9300 +/- 30 BP
Calibration: BetaCal4.20: HPD method: INTCAL20

Results are ISO/IEC-17025:2017 accredited. No sub-contracting or student labor was used in the analyses. All work was done at Beta in 4 in-house NEC accelerator mass spectrometers and 4 Thermo IRMSs. The "Conventional Radiocarbon Age" was calculated using the Libby half-life (5568 years), is corrected for total isotopic fraction and was used for calendar calibration where applicable. The Age is rounded to the nearest 10 years and is reported as radiocarbon years before present (BP), "present" = AD 1950. Results greater than the modern reference are reported as percent modern carbon (pMC). The modern reference standard was 95% the 14C signature of NIST SRM-4990C (oxalic acid). Quoted errors are 1 sigma counting statistics. Calculated sigmas less than 30 BP on the Conventional Radiocarbon Age are conservatively rounded up to 30. d13C values are on the material itself (not the AMS d13C). d13C and d15N values are relative to VPDB-1. References for calendar calibrations are cited at the bottom of calibration graph pages.

**Beta Analytic, Inc.**
4985 SW 74th Court
Miami, FL 33155 USA
Tel: 305-667-5167
Fax: 305-663-0964
info@betalabservices.com

ISO/IEC 17025:2017-Accredited Testing Laboratory

# REPORT OF RADIOCARBON DATING ANALYSES

Jeremy Lloyd
University of Durham

Report Date: January 06, 2021
Material Received: December 21, 2020

| Laboratory Number | Sample Code Number | Conventional Radiocarbon Age (BP) or Percent Modern Carbon (pMC) & Stable Isotopes | |
|---|---|---|---|
| **Beta - 579376** | **LDM20-S3: 164-165**<br>Depth in core: 153-154 cm | **4680 +/- 30 BP** | IRMS δ13C: +2.7 o/oo<br>IRMS δ18O: +1.4 o/oo |
| | **(95.4%) 3283 - 2933 cal BC** | **(5232 - 4882 cal BP)** | |

Submitter Material: Shell (Marine)
Pretreatment: (shell) acid etch
Analyzed Material: Shell
Analysis Service: AMS-Standard delivery
Percent Modern Carbon: 55.84 +/- 0.21 pMC
Fraction Modern Carbon: 0.5584 +/- 0.0021
D14C: -441.56 +/- 2.09 o/oo
Δ14C: -446.33 +/- 2.09 o/oo (1950:2021)
Measured Radiocarbon Age: (without d13C correction): 4230 +/- 30 BP
Calibration: BetaCal3.21: HPD method: MARINE13
DeltaR: -100 +/- 35

Results are ISO/IEC-17025:2017 accredited. No sub-contracting or student labor was used in the analyses. All work was done at Beta in 4 in-house NEC accelerator mass spectrometers and 4 Thermo IRMSs. The "Conventional Radiocarbon Age" was calculated using the Libby half-life (5568 years), is corrected for total isotopic fraction and was used for calendar calibration where applicable. The Age is rounded to the nearest 10 years and is reported as radiocarbon years before present (BP), "present" = AD 1950. Results greater than the modern reference are reported as percent modern carbon (pMC). The modern reference standard was 95% the 14C signature of NIST SRM-4990C (oxalic acid). Quoted errors are 1 sigma counting statistics. Calculated sigmas less than 30 BP on the Conventional Radiocarbon Age are conservatively rounded up to 30. d13C values are on the material itself (not the AMS d13C). d13C and d15N values are relative to VPDB-1. References for calendar calibrations are cited at the bottom of calibration graph pages.

**Beta Analytic, Inc.**
4985 SW 74th Court
Miami, FL 33155 USA
Tel: 305-667-5167
Fax: 305-663-0964
info@betalabservices.com

ISO/IEC 17025:2017-Accredited Testing Laboratory

# REPORT OF RADIOCARBON DATING ANALYSES

Jeremy Lloyd
University of Durham

Report Date: January 06, 2021
Material Received: December 21, 2020

| Laboratory Number | Sample Code Number | Conventional Radiocarbon Age (BP) or Percent Modern Carbon (pMC) & Stable Isotopes | |
|---|---|---|---|
| **Beta - 579374** | **LDM20-S1: 166-168**<br>Depth in core: 153-155 cm | **5770 +/- 30 BP** | IRMS δ13C: +1.8 o/oo<br>IRMS δ18O: -0.9 o/oo |
| | **(95.4%) 4441 - 4242 cal BC** | **(6390 - 6191 cal BP)** | |

Submitter Material: Shell (Marine)
Pretreatment: (shell) acid etch
Analyzed Material: Shell
Analysis Service: AMS-Standard delivery
Percent Modern Carbon: 48.76 +/- 0.18 pMC
Fraction Modern Carbon: 0.4876 +/- 0.0018
D14C: -512.42 +/- 1.82 o/oo
Δ14C: -516.59 +/- 1.82 o/oo (1950:2021)
Measured Radiocarbon Age: (without d13C correction): 5340 +/- 30 BP
Calibration: BetaCal3.21: HPD method: MARINE13
DeltaR: -100 +/- 35

Results are ISO/IEC-17025:2017 accredited. No sub-contracting or student labor was used in the analyses. All work was done at Beta in 4 in-house NEC accelerator mass spectrometers and 4 Thermo IRMSs. The "Conventional Radiocarbon Age" was calculated using the Libby half-life (5568 years), is corrected for total isotopic fraction and was used for calendar calibration where applicable. The Age is rounded to the nearest 10 years and is reported as radiocarbon years before present (BP), "present" = AD 1950. Results greater than the modern reference are reported as percent modern carbon (pMC). The modern reference standard was 95% the 14C signature of NIST SRM-4990C (oxalic acid). Quoted errors are 1 sigma counting statistics. Calculated sigmas less than 30 BP on the Conventional Radiocarbon Age are conservatively rounded up to 30. d13C values are on the material itself (not the AMS d13C). d13C and d15N values are relative to VPDB-1. References for calendar calibrations are cited at the bottom of calibration graph pages.

**Beta Analytic, Inc.**
4985 SW 74th Court
Miami, FL 33155 USA
Tel: 305-667-5167
Fax: 305-663-0964
info@betalabservices.com

ISO/IEC 17025:2017-Accredited Testing Laboratory

# REPORT OF RADIOCARBON DATING ANALYSES

Jeremy Lloyd
University of Durham

Report Date: January 06, 2021
Material Received: December 21, 2020

| Laboratory Number | Sample Code Number | Conventional Radiocarbon Age (BP) or Percent Modern Carbon (pMC) & Stable Isotopes | |
|---|---|---|---|
| **Beta - 579375** | **LDM20-S2: 167-168**<br>Depth in core: 154-155 cm | **5690 +/- 30 BP** | IRMS δ13C: +1.9 o/oo<br>IRMS δ18O: -0.1 o/oo |
| | **(95.4%) 4357 - 4144 cal BC** | **(6306 - 6093 cal BP)** | |

Submitter Material: Shell (Marine)
Pretreatment: (shell) acid etch
Analyzed Material: Shell
Analysis Service: AMS-Standard delivery
Percent Modern Carbon: 49.25 +/- 0.18 pMC
Fraction Modern Carbon: 0.4925 +/- 0.0018
D14C: -507.54 +/- 1.84 o/oo
Δ14C: -511.75 +/- 1.84 o/oo (1950:2021)
Measured Radiocarbon Age: (without d13C correction): 5250 +/- 30 BP
Calibration: BetaCal3.21: HPD method: MARINE13
DeltaR: -100 +/- 35

Results are ISO/IEC-17025:2017 accredited. No sub-contracting or student labor was used in the analyses. All work was done at Beta in 4 in-house NEC accelerator mass spectrometers and 4 Thermo IRMSs. The "Conventional Radiocarbon Age" was calculated using the Libby half-life (5568 years), is corrected for total isotopic fraction and was used for calendar calibration where applicable. The Age is rounded to the nearest 10 years and is reported as radiocarbon years before present (BP), "present" = AD 1950. Results greater than the modern reference are reported as percent modern carbon (pMC). The modern reference standard was 95% the 14C signature of NIST SRM-4990C (oxalic acid). Quoted errors are 1 sigma counting statistics. Calculated sigmas less than 30 BP on the Conventional Radiocarbon Age are conservatively rounded up to 30. d13C values are on the material itself (not the AMS d13C). d13C and d15N values are relative to VPDB-1. References for calendar calibrations are cited at the bottom of calibration graph pages.